Exploring the Stochastic Performance of Metallic Microstructures With Multi-Scale Models

Arulmurugan Senthilnathan

Dissertation submitted to the Faculty of the
Virginia Polytechnic Institute and State University
in partial fulfillment of the requirements for the degree of

Doctor of Philosophy
in
Mechanical Engineering

Pinar Acar, Chair
Bart Raeymaekers
Mehdi Ahmadian
Rakesh K Kapania

April 18, 2023
Blacksburg, Virginia

Keywords: Multi-Scale modeling, Microstructure Characterization and Reconstruction, Moment Invariants, Crystal Plasticity, Uncertainty Quantification, Phase Transition, Ising Model

Exploring the Stochastic Performance of Metallic Microstructures With Multi-Scale Models

Arulmurugan Senthilnathan

(ABSTRACT)

Titanium-7%wt-Aluminum (Ti-7Al) has been of interest to the aerospace industry owing to its good structural and thermal properties. However, extensive research is still needed to study the structural behavior and determine the material properties of Ti-7Al. The homogenized macro-scale material properties are directly related to the crystallographic structure at the micro-scale. Furthermore, microstructural uncertainties arising from experiments and computational methods propagate on the material properties used for designing aircraft components. Therefore, multi-scale modeling is employed to characterize the microstructural features of Ti-7Al and computationally predict the macro-scale material properties such as Young's modulus and yield strength using machine learning techniques. Investigation of microstructural features across large domains through experiments requires rigorous and tedious sample preparation procedures that often lead to material waste. Therefore, computational microstructure reconstruction methods that predict the large-scale evolution of microstructural topology given the small-scale experimental information are developed to minimize experimental cost and time. However, it is important to verify the synthetic microstructures with respect to the experimental data by characterizing microstructural features such as grain size and grain shape. While the relationship between homogenized material properties and grain sizes of microstructures is well-studied through the Hall-Petch effect, the influences of grain shapes, especially in complex additively manufactured microstructure topologies, are yet to be explored. **Therefore, this work addresses the gap**

in the mathematical quantification of microstructural topology by developing measures for the computational characterization of microstructures. Moreover, the synthesized microstructures are modeled through crystal plasticity simulations to determine the material properties. However, such crystal plasticity simulations require significant computing times. In addition, the inherent uncertainty of experimental data is propagated on the material properties through the synthetic microstructure representations. Therefore, the aforementioned problems are addressed in this work by explicitly quantifying the microstructural topology and predicting the material properties and their variations through the development of surrogate models. Next, this work extends the proposed multi-scale models of microstructure-property relationships to magnetic materials to investigate the ferromagnetic-paramagnetic phase transition. Here, the same Ising model-based multi-scale approach used for microstructure reconstruction is implemented for investigating the ferromagnetic-paramagnetic phase transition of magnetic materials. The previous research on the magnetic phase transition problem neglects the effects of the long-range interactions between magnetic spins and external magnetic fields. Therefore, **this study aims to build a multi-scale modeling environment that can quantify the large-scale interactions between magnetic spins and external fields.**

Exploring the Stochastic Performance of Metallic Microstructures With Multi-Scale Models

Arulmurugan Senthilnathan

(GENERAL AUDIENCE ABSTRACT)

Titanium-Aluminum (Ti-Al) alloys are lightweight and temperature-resistant materials with a wide range of applications in aerospace systems. However, there is still a lack of thorough understanding of the microstructural behavior and mechanical performance of Titanium-7wt%-Aluminum (Ti-7Al), a candidate material for jet engine components. This work investigates the multi-scale mechanical behavior of Ti-7Al by computationally characterizing the micro-scale material features, such as crystallographic texture and grain topology. The small-scale experimental data of Ti-7Al is used to predict the large-scale spatial evolution of the microstructures, while the texture and grain topology is modeled using shape moment invariants. Moreover, the effects of the uncertainties, which may arise from measurement errors and algorithmic randomness, on the microstructural features are quantified through statistical parameters developed based on the shape moment invariants. A data-driven surrogate model is built to predict the homogenized mechanical properties and the associated uncertainty as a function of the microstructural texture and topology. Furthermore, the presented multi-scale modeling technique is applied to explore the ferromagnetic-paramagnetic phase transition of magnetic materials, which causes permanent failure of magneto-mechanical components used in aerospace systems. Accordingly, a computational solution is developed based on an Ising model that considers the long-range spin interactions in the presence of external magnetic fields.

Dedication

To my family

Acknowledgments

First, I would like to thank my advisor Professor Pinar Acar for giving me this wonderful opportunity. Without her constant encouragement and guidance, this would not have been possible. Especially during the pandemic, when the whole world became uncertain, she made sure I am doing okay and gave me continuous motivation to do my research. She also supported working from home to keep continuing my research work. She introduced and motivated me to participate in multiple conferences and guided me in preparing for technical presentations and scientific writing. Throughout this journey, Professor Pinar Acar is kind, humble, supportive, and always welcomed new ideas. Her review of my work has improved my skills to conduct research and write scientific papers in a scholarly manner. Working in the ASTRO lab under the guidance of an inspiring professional certainly encouraged me to pursue my dreams of working in the academic field. I am forever grateful to Professor Acar for this incredible opportunity and all the insightful learnings throughout this journey.

It is an absolute privilege for me to have Professor Bart Raeymaekers, Professor Mehdi Ahmadian and Professor Rakesh Kapania on my dissertation committee. I am extremely grateful for the continuing support, guidance and scholarly advice of the committee members on my dissertation work. I would like to express my utmost gratitude for their insightful advice and encouragement on my research work and career. I am very grateful to have had the opportunity to meet Professor Reza Mirzaeifar. His guidance and support in my research are invaluable. My sincere appreciation and thanks to Professor Veera Sundararaghavan, Dr. Mohammadreza Yaghoobi and Iman Javaheri, University of Michigan, Ann Arbor and Professor Marc DeGraef, Carnegie Mellon University for their insightful comments, discussions and suggestions that helped my research. I would like to thank my lab mates Mahmudul

Hasan, Sheng Liu, Rick Catania, Ender Eger, Hengduo Zhao, Matthew Long and Mohamed Elleithy for their incisive discussions and comments.

There are no words to express the love and unyielding support of my mother, father, grandfather and all other family members. Their continuous moral motivation and cheering surely have fortified my will to work hard and deliver my best every day. I am very fortunate to have such amazing and optimistic friends who were always there for me and got my back. Especially, I am grateful to my college friends who always encouraged me to focus on my work and career. I also would like to thank my flatmate Abhishek Pandala for being kind and understanding throughout all these years. I would like to express my gratitude towards Professor Katerina Aifantis, Professor Curtis Taylor and Professor Bhavani Sankar, University of Florida for their encouragement and support to pursue my dreams.

I sincerely appreciate and thank the Air Force Office of Scientific Research (FA9550-21-1-0120 - UNDOPhase: UNcertainty-DOminated Phase Transitions in Magnetic Materials, AFOSR YIP Grant, Materials with Extreme Properties Program) and National Science Foundation (NSF CMMI # 2053840 - Collaborative Research: AI-Driven Multi-Scale Design of Materials under Processing Constraints) for their financial support. Furthermore, I also would like to thank Professor John Allison, Professor Veera Sundararaghavan and Iman Javaheri, University of Michigan, Ann Arbor for kindly providing me with the experimental data.

I thank God almighty for everything.

Contents

List of Figures

List of Tables

List of Abbreviations

$\bar{\lambda_s}$	Set of average Principle eigenvalue moment of synthesized images
$\bar{x}, \bar{y}$	Coordinates of centroid of an image
β	Critical exponent
η_{ij}	Normalized central moment
γ	Order parameter
λ	Principle eigenvalue moment
λ_e	Principle eigenvalue moment of an experimental image
λ_s	Principle eigenvalue moment of a synthesized image
μ_{ij}	Central moment
ω	Gaussian weightage parameter
$\phi_1, ..., \phi_7$	Hu moments
ρ_a	Ratio of area of the enclosed circle to the convex hull
ρ_p	Ratio of perimeter of the enclosed circle to the convex hull
σ	Spin parameter
Σ_{xx}, Σ_{yy}	Variance
Σ_{xy}	Covariance

ζ	Mean distance between all synthesized samples and the experimental image
$d_{\bar{\lambda}}$	Average distance parameter
d_{cr}	Distance between centroids
F	Free energy
f	Free energy per number of site
H	Hamiltonian energy
h	External magnetic field parameter
k_B	Boltzmann constant
m	Magnetization parameter
m_{ij}	Raw moment
R	Radius of the circle
T	Temperature
T_c	Critical temperature
λ_1	Largest eigenvalue
λ_2	Smallest eigenvalue
i,j	Order of the moment
N	Dimensions of the model
x,y	Coordinates

Chapter 1

INTRODUCTION

Materials for aerospace applications must meet numerous selection criteria regarding mechanical and chemical properties [1] to ensure safety and deliver better performance [2]. Different parts of an aircraft have individual requirements significant to their function. For example, aircraft frames require a good strength-to-weight ratio, high fatigue life cycle, damage tolerance, reliability, high corrosive resistance, etc. Additionally, the engine components necessitate materials to exhibit the ability to endure high temperatures [1]. By consistently meeting the requirements, aircraft models have evolved throughout the years [1]. Design conditions for aerospace materials induce research in the field of material science for a better understanding of the structural and material behavior of existing commercial materials and to develop new alloys that would perform better. One such class of materials that satisfies the design requirements for particular aircraft components is the Titanium-Aluminum (Ti-Al) alloys. Owing to their lightweight, and resistance to heat and corrosion, titanium alloys have been employed in different parts of aircraft including the turbine fan blades, fuselage, low-pressure compressor blade, etc [3, 4]. The possible application of titanium and its alloys in the aerospace industry has been well studied in the past [4, 5, 6, 7, 8, 9, 10, 11, 12].

The amalgamation of titanium and aluminum has proven to be increasing the ductility of the material and simultaneously reducing its weight [13]. The most commercially used titanium alloy is Ti-6Al-4V [10]. Segregation of aluminum into titanium yields a lightweight material. However, when the aluminum content is increased above 7%, a decrease in the ductility of

the material is observed [13, 14] due to the formation of Ti_3Al (α_2 phase) that embrittles the material. Nevertheless, the ductility until 7% is reported to be satisfactory [13]. Additionally, the intermetallic Titanium-Aluminides have also been found to be sustaining better at higher temperatures [15, 16] and significantly lighter than the nickel and iron-based alloys [15]. Therefore, Ti-7Al is of huge interest to the aerospace industry owing to its lightweight and high thermal properties [16, 17]. Especially, Ti-7Al is considered for use in turbine blades [18]. Having a better understanding of the microstructural behavior of Ti-7Al helps in designing the material better suited for the performance of aircraft components at the macro-scale.

The Ti-7Al alloy has a Hexagonal Close-Packed (HCP) crystal structure. It has three basal $< a >$, three prismatic $< a >$, six pyramidal $< a >$, twelve pyramidal $< c+a >$ slips and six tensile twin systems. However, the crystal plasticity parameters of Ti-7Al are not universally agreed [19]. Moreover, Young's modulus values of Ti-7Al are also known to be varying due to experimental measurement uncertainties [20]. Therefore, multiple different approaches have been employed in the past to study the material behavior of Ti-7Al and determine its elastic and plastic properties [14, 21, 22]. However, experimental methodologies performed to study the microstructural behavior of Ti-7Al and determine its homogenized material properties are costly and computationally expensive.

The conventional manufacturing methodologies often lead to huge wastage in raw materials and are limited when producing parts and components with complex geometries [23]. Therefore, additive manufacturing techniques such as Selective Laser Melting (SLM) have been of keen interest to the aerospace industry [12, 24, 25]. Additive manufacturing surpasses the disadvantages of traditional subtractive technologies by ensuring the machinability of complex shapes with optimized topology [23]. However, metal additive manufacturing still remains a costly method. Therefore, owing to the high cost of materials used in the aerospace industry, the manufacturing capabilities are considered under design to reduce production

costs and time. Moreover, the crystallographic nature of polycrystalline materials such as Ti-7Al is a direct result of the manufacturing process. The microstructural topology of a material heavily influences the macro-scale homogenized material properties that are considered in the design. Hence, it is crucial to investigate what set of manufacturing parameters can yield a microstructure with desired homogenized material properties. Additionally, the experimental measurements often lead to uncertainty in the microstructural topology which then propagates on the computed material properties [20]. Therefore, uncertainty is heeded as an important factor in designing aircraft components [26]. Moreover, algorithmic uncertainties can also propagate on the material properties computed through simulations modeled with synthetic microstructures [27, 28]. Therefore, in order to improve the component performance at the macro-scale and achieve economic feasibility during manufacturing, the characteristic features of the polycrystalline material should be studied at the micro-scale through physics-based and data-driven multi-scale models while considering the effects of uncertainty.

Multi-scale modeling is a cross-disciplinary approach that employs information from one length scale to understand the behavior of a system at another, thereby linking the gap between different length scales (Figure 1.1). By reducing experimental iterations, multi-scale modeling lowers the cost and time required for materials design. Additionally, multi-scale modeling provides room for innovation in design that would improve product performance and quality. Over the years, the applications of multi-scale modeling have been explored in fields such as Astronomy [29], Biology [30], Physics [31], Chemistry [32], and many more. In the field of materials science, the application of multi-scale modeling has produced a better understanding of structure-property relations [33, 34]. Multi-scale modeling benefits in solving the macro-scale problems at the component level by understanding the characteristic features of material topology at the micro-scale. For instance, metallic parts and components

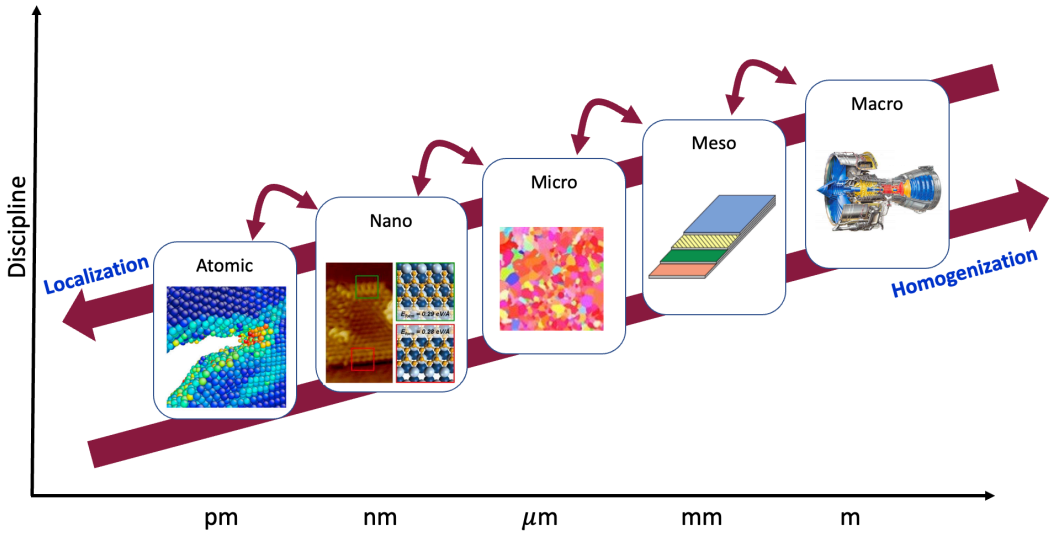

Figure 1.1: Multi-scale modeling as a cross-disciplinary approach to study material behavior [36, 37, 38, 39, 40]. This dissertation work develops numerical methods to study the multi-scale mechanical and magnetic behavior of Ti-Al alloys and ferromagnetic materials widely used in aerospace systems.

that frequently experience fatigue loading perform worse and eventually lead to failure. The failure of materials can be attributed directly to their microstructural characteristic features. This is because the homogenized (volume-averaged) properties and performance of materials are determined by the underlying microstructural features (i.e., texture, grain topology). In fact, the grain size and shape of a polycrystalline microstructure significantly impact the homogenized material response [35].

A classic example is the failure of ductile materials due to the nucleation and coalescence of voids at the micro level upon external loading [41]. Even in the absence of external loads, the presence of several kinds of crystallographic defects can influence the homogenized material properties. Inversely, one can design the material to have desired properties by optimizing the topology of microstructures. The recrystallization process can eliminate any defects in the material which improves the ductility of the material. Thus, by controlling the micro-scale

phenomenon, macro-scale qualities of materials can be designed. The macro-micro relations of grain size and homogenized material properties are well-studied through the Hall-Petch effect [35]. However, the influences of grain shapes, especially in complex microstructures, are yet to be explored.

1.1 Motivation

This work focuses on developing multi-scale models for understanding two different research problems. The first involves Microstructure Characterization and Reconstruction (MCR) techniques. In order to save the cost and time required for experiments, computational methods are developed to reconstruct synthetic microstructures in large domains. The microstructural features are visualized with instruments such as an optical microscope, Scanning Electron Microscope (SEM), Transmission Electron Microscope (TEM), and Atomic Force Microscopy (AFM) [42, 43]. For metallic microstructures, Electron Backscatter Diffraction (EBSD) [44, 45, 46, 47, 48] and X-ray diffraction [49, 50, 51] are predominantly used to determine the grain orientation information. Moreover, many other procedures are introduced to detect the grain mapping [52, 53, 54].

However, micro-scale experiments using expensive instruments often require rigorous time-consuming sample preparation procedures that often lead to material waste. To minimize the cost and time requirements of these large-scale experiments, computational microstructure reconstruction methods are applied to predict the microstructural evolution in large domains given the small-scale experimental information [55]. Next, these synthesized microstructures are used to determine the material properties through computational simulations. However, carrying out a combination of tasks involving microstructure reconstruction and crystal plasticity simulations is expensive. Additionally, the inherent uncertainty of experimental

images propagated on the material properties via reconstructed samples requires a ubiquitous methodology to quantify the microstructure topology. Therefore, this work concentrates on addressing the aforementioned problems and contributes toward advancing the state-of-the-art techniques for microstructure reconstruction by explicitly quantifying the grain shapes of the synthetic microstructures and developing surrogate models to predict material properties as a function of microstructure texture and topology [56, 57, 58, 59, 60]. This work focuses on Ti-7Al, a candidate for applications in the aerospace industry owing to its lightweight and better strength at higher temperatures [16]. The EBSD samples of Ti-7Al used in this work indicate a close-to-randomly oriented microstructural texture with slight variability in the textures of different samples. The presented scheme will be applicable to study microstructures having any type of grain structure and here it will be tested for the forged and additively manufactured samples of the same material, which is the Ti–7Al alloy.

On the other hand, the second research problem involves investigating the instability of the ferromagnetic-paramagnetic phase transition in metals. Ferromagnetic materials naturally exist in magnetic domains where all of the spins in each domain are aligned in the same direction. These materials exhibit permanent magnetic properties upon applying an external magnetic field. Ferromagnetic materials are used in various electromagnetic and Giant-Magneto Resistance (GMR) devices in aircraft due to their strong magnetic properties [61]. More importantly, the powdered ferrites are used in fighter aircraft [62] as a Radar Absorbing Material (RAM) that converts the incoming radar waves into heat and thereby performs as a stealth aircraft. Only a few materials including iron, cobalt, nickel and some rare earth materials exhibit this ferromagnetic property.

However, the extreme environment contributes to affecting the performance of magnetic materials that are used in critical components. When the temperature exceeds a point known as the Curie temperature, ferromagnetic materials lose their magnetic strength and

transition into a weak magnetic phase known as paramagnetic material. However, in reality, the phase transition is rather a zone than a single point due to measurement uncertainties. Conventionally, a lattice-based model is used to study the magnetic phase transition [63, 64] under the effects of neighbor spins [65, 66, 67, 68] and external magnetic field [69, 70, 71, 72, 73]. Nevertheless, the computational time restricts obtaining the exact solution for the magnetic phase transition problem under the effects of long-range neighbors. Therefore, by using numerous approximation theories [67], historically the magnetic phase transition problem is solved either for short-range neighbors either with [68, 69, 70, 71, 72, 73] or without an external magnetic field [65, 66, 74]. Although some notable works have attempted to include long-range interactions [75, 76], this work develops a numerical approach using optimization techniques including the presence of an external magnetic field. Furthermore, the magnetic phase transition problem is also solved for the 3D model but without the effects of the external magnetic field [67]. Therefore, this work builds the theory for solving a 2D magnetic phase transition problem using an optimization approach that is to be extended to study the 3D polycrystalline materials while accounting for the crystallographic effects in the future.

1.2 Contributions

The contributions of this study to the state-of-the-art multi-scale modeling of materials are listed next:

1. **Quantitatively characterizing the microstructure topology**

    - This work develops a two-stage methodology that statistically validates the reconstructed microstructure images with respect to available small-scale experimental

data. The validation is achieved by quantifying the 2D and 3D grain shapes of polycrystalline microstructures using the concept of moment invariants. The Principle Eigenvalue Moments (PEM) are introduced as new shape descriptors for representing the microstructure topology. The developed methodologies aid the computational tools used to investigate the material behavior and properties of alloys like Ti-7Al, which are of great interest to the aerospace industry. Moreover, the developed methodologies are also designed to be ubiquitous in characterizing any kind of microstructure including composites, ceramics, etc.

2. **Quantifying the uncertainty of the microstructure topology**

   - This work proposes PEM based on Hu moments [77] as a numerical descriptor to quantify the uncertainty of microstructural features and homogenized properties arising from the experimental data and computational reconstruction of the synthetic microstructures. These parameters are utilized to capture the expected values of the microstructural features in addition to the deviations arising from the uncertainties. These statistical parameters can also be used to understand and analyze the quality of the microstructure reconstruction when employing different MRF parameters, including the window size and image resolution.

3. **Investigating the effects of topology and its uncertainty on material properties**

   - A surrogate model based on Gaussian Process Regression (GPR) (Figure 1.2) is developed to predict the material properties and the associated uncertainty as a function of PEM that quantifies the microstructure texture and topology. The surrogate model is also used to compute the variations of the mechanical properties as a result of the microstructure uncertainty. Therefore, moments invariant

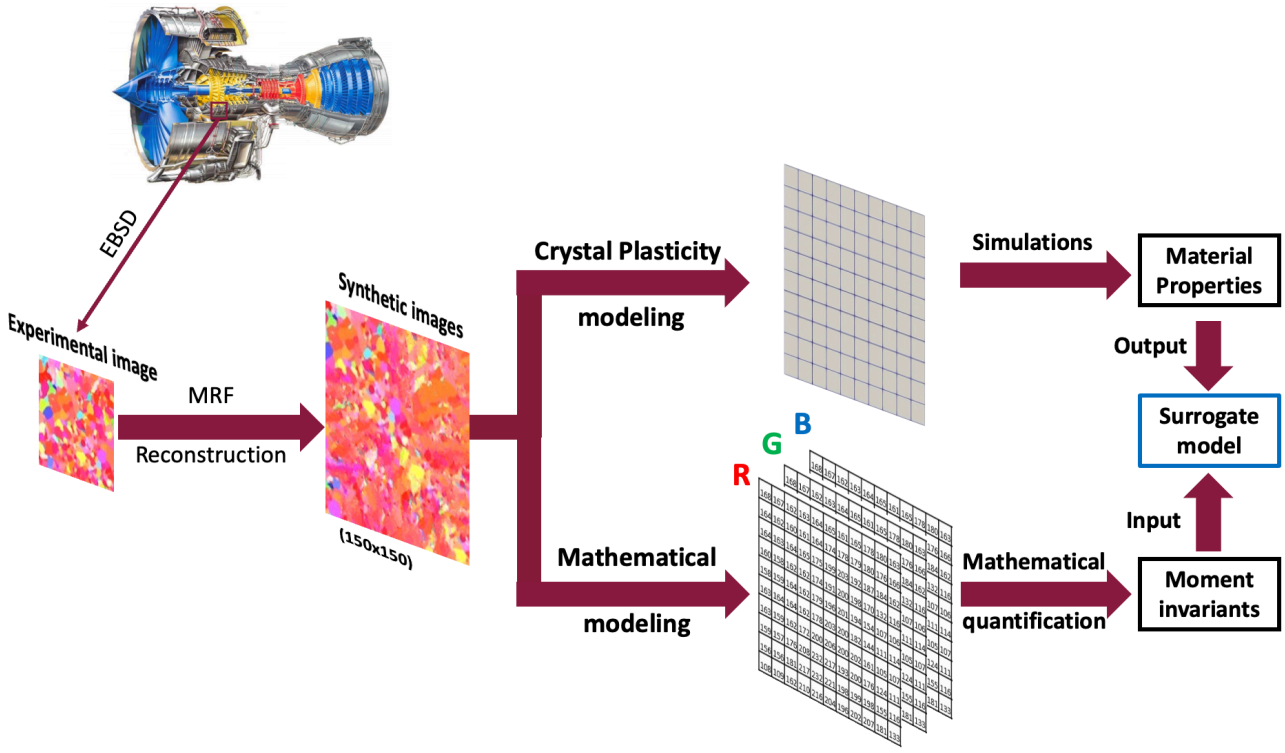

Figure 1.2: Outline of a surrogate model developed for predicting mechanical properties as a function of moment invariants representing microstructural features

to Rotation, Scale and Translation (RST) are proposed as a new descriptor for representing microstructural topology. Using RST invariants to represent microstructural topology brings significant data reduction when compared to direct image-based training performed using computationally expensive deep learning techniques.

Chapter 2

MICROSTRUCTURE RECONSTRUCTION AND CHARACTERIZATION

The topology of metallic microstructures is conventionally identified through EBSD [44, 45, 46, 47, 49, 78] that scans small sample surfaces in an SEM device. EBSD imaging provides a dataset containing information about the crystallographic characteristics of the material. One such important microstructural feature is the grain orientation displayed through the Inverse Pole Figure (IPF) [79]. The IPF mapping identifies the crystallographic orientation information of the microstructure through the Red-Green-Blue (RGB) coloring system. Thus, EBSD serves as a powerful tool in extracting vital information about material characterization. However, it requires rigorous and tedious sample preparation techniques. Furthermore, operating powerful devices, such as electron microscopes, comes at the expense of requiring vigorously trained human work and utilizing the device multiple times. On the other hand, computational material science offers efficient solutions for expensive experimental techniques. One such example would be the microstructure reconstruction techniques [80, 83, 84, 85, 86, 87, 88, 89, 90, 81, 82] developed to predict microstructural evolution in large domains using the small-scale information characterizing the microstructural features.

In the past, the area of Microstructure Characterization and Reconstruction (MCR) has

been widely investigated [55]. MCR is based on the notion that if a parameter describing the characteristic features of a microstructure contains enough information about the microstructural topology, it can be utilized to create a statistically equivalent microstructure. The rapidly evolving field of MCR has begun with some pioneer works developing statistical parameters that are set to capture the information about the microstructural images explicitly. Examples include two-point correlations either with simulated annealing [80, 83, 84, 91, 92, 93] or the phase recovery algorithm [94, 95], and the Voronoi tessellation [86, 96]. This is followed by the utilization of the geometry-based shape descriptors such as the ellipsoid [84, 85]. Some other notable techniques include image in-painting [97] and the experimental reconstruction through milling [98, 99].

A more advanced characterization technique involves the implementation of a pattern recognition algorithm through the Support Vector Machine (SVM) [87], deep learning [88], and supervised machine learning [88, 89, 90, 81, 82] techniques. The complex and implicit nature of Machine Learning (ML) based methodologies make the reconstruction of color (RGB) microstructure images difficult. On the other hand, the image-based reconstruction techniques are found to perform better than the above-mentioned methods by eliminating the need of characterizing the topology without compromising the physical meaning of the microstructural features [28]. It does so by using a neighboring analysis (NA) where a window size parameter is defined. One such example would include the Markov Random Field (MRF) method [28, 100, 101, 102, 103]. Furthermore, some ML-based techniques such as transfer learning [81], supervised learning [89], and Convolutional Neural Network (CNN) [82] have also been used for MCR with a non-parametric approach. However, deep learning techniques always require a large amount of data samples for training neural networks. Therefore, the probabilistic graphical model that requires relatively minimum experimental data is chosen in this study to reconstruct the microstructures of 2D EBSD images using the MRF method.

The organization of Chapter 2 is as follows: Section 2.1 discusses the development of the Ising model. Section 2.2 introduces the reconstruction of microstructure images using MRF. Section 2.3 presents the microstructural characterization techniques for verification of the reconstructed microstructures.

2.1 Ising model

The Ising model was initially developed by Ernest Ising for understanding the magnetic phase transition [63]. The Ising model corresponds to a lattice-based structure (Figure 2.1 (a)). The lattice points are a set of periodically located points at regular intervals. The bond connecting the lattice points is called an edge and it encloses the model with boundaries. Thus, the lattice arrangement of the model can be thought as of a periodic arrangement of the lattice square connecting four lattice points forming the unit cell in 2D. For 3D, the unit cell would be the lattice cube connecting 6 points. The Ising model can be constructed for any model size of N^d with dimensions, d, of 1, 2, and 3. Another important concept of the Ising model is the nearest neighbors which are defined for a lattice point (i) as the immediate neighboring lattice points (j) located in all available directions. For the cases of $d = 1$, 2, and 3, the numbers of nearest neighbours are $j = 2$, 4, and 6, respectively. The nearest neighbors are also known as the first-order neighbors. The second-order neighbors constitute the next level of close neighbors.

The edges enclosing the first and second nearest neighbors form a square window of size 1 (pixel^2). An example window with a size of 1 is illustrated in Figure 2.1 (b). For the k^{th} nearest neighbor, the window size ranges from $k = 1$ to $k = N - 1$. However, for the lattice points on the boundary, the neighborhood window is not square. Rather, the shape of the window is bent according to the number of available lattice points. The same applies to

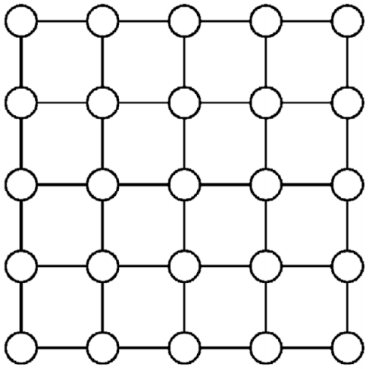

(a) Simple Ising model

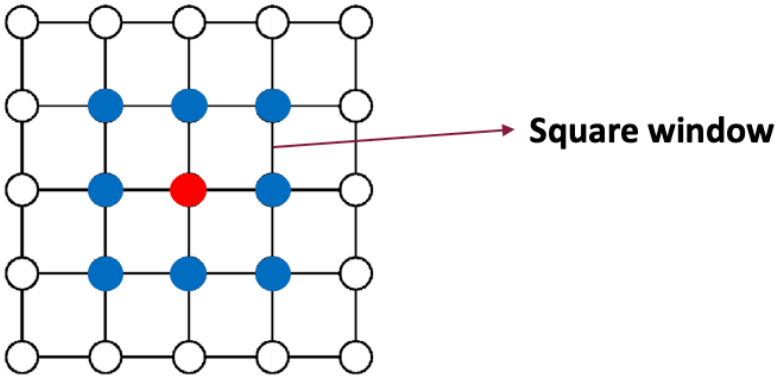

(b) Simple Ising model with Square window

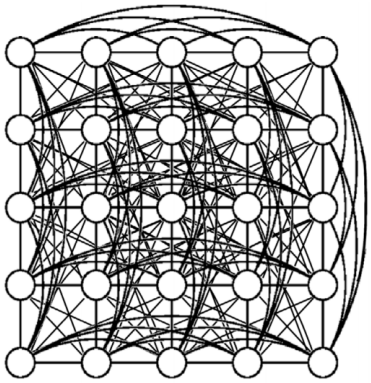

(c) Higher order Ising model

Figure 2.1: MRF as an undirected graphical model. The circles show the pixels of an image. The bonds are used to connect the neighbors: (a) Ising model with the nearest neighbor interactions. (b) A square window on a simple Ising model with a pixel of interest located at the center (Red) connected to all neighbors (blue) within the window. (c) A higher-order Ising model. The microstructure reconstruction performed in this work is based on the MRF method, which is a higher-order Ising model [56].

the bonding connecting the lattice points on the boundary. While the interior lattice points are covered by all j neighbor points, the boundary lattice points get cut due to the shape of the model. However, Ising models are applied often for larger systems and so only a small fraction of the total number of lattice points occupies the lattice sites of the boundary. Hence, the assumption of adjustable window size for the lattice nodes located at the edges and corners is acceptable.

An image of $N \times N$ dimensions is mathematically a matrix of $N \times N$ with each element of the matrix containing the pixel intensity value of that particular pixel. While a binary and a grayscale image have a single channel representing a single matrix, a color image has three (RGB) channels. The pixel intensity of a grayscale or an RGB image is defined with values ranging from 0 to 255 for each channel while the binary image has only two choices: either 0 or 1. A simple model is illustrated in Figure 2.1 (a). Furthermore, for modeling microstructures, a higher-order Ising model where all the nodes are connected to one another, as illustrated in Figure 2.1 (c), is assumed to include the long-range interactions.

In order to reconstruct the synthetic microstructure images, the higher-order system is further developed as a probabilistic graph model by applying conditional dependence according to Markov's rule [28]. When the lattice points and the edges can be thought as of random variables (RVs) and correlation functions, respectively, the Ising model can be used to model the microstructural images. Because, in an image, the pixels are correlated with one another [56].

2.2 Microstructure reconstruction by Markov Random Fields

Graphical model (GM) is a class of machine learning used to study domain problems with a graphical approach. Since GM can help incorporate the uncertainty, it is a suitable candidate for modeling microstructure images for reconstruction with a non-deterministic approach. GM is a general framework that has a declarative representation of a model describing the construction of a system. The model contains the knowledge of system function in detailed semantics and algorithms are developed for reasoning the most probable outcome based on the developed graphical model [104].

There are two types of probabilistic graphical models namely the Directed Graphical Model (DGM) and the Undirected Graphical Model (UGM). The difference between the two is the assignment of a direction to the edges connecting two random variables. The directed model such as a Bayesian network relies on the history of the present state. However, the absence of a direction paves the way for defining a neighborhood window in the undirected models. Therefore, the UGM solely depends on its current state. Conventionally, UGM is also known as Markov networks based on which the Markov Random Field (MRF) algorithm is developed.

There are multiple reasons to prefer MRF for microstructure reconstruction. First, MRF has an edge over the other types of reconstruction techniques since the random nature of its algorithm enables the reconstruction of multiple samples from a relatively small amount of experimental data. Also, MRF samples are a useful source to analyze the propagation of epistemic and aleatoric uncertainty. Furthermore, MRF requires relatively very small experimental data to synthesize the microstructures. Hence, MRF is adopted in this work to generate synthetic microstructures [56, 57, 58, 59, 60]. The MRF reconstruction has been

applied in the past for both spatial and temporal reconstruction [28] in large domains using small-scale experimental data. This work focuses on using the algorithm implemented in [28] for the spatial reconstruction of Ti-7Al microstructure images. The methodology of the MRF algorithm follows the previous work by [28, 103]. The structure of the algorithm is explained by [28] and is described here in brevity.

To apply the MRF algorithm, the microstructure image is mathematically constructed using an Ising model [63]. Therefore, the image is designed as an $N \times N$ lattice with values X_{i} containing any one of G color levels in the range *0, 1, ..., $G - 1$* assigned to each particle i of the lattice. In an Ising model for microstructural images, each particle representing the pixels conditionally depends on its neighbors [56]. In other words, the edge connecting two particles of the lattice is absent if they both are conditionally independent. Conventionally, each particle of an Ising model is connected to its neighbors as illustrated in Figure 2.1 (a). However, for modeling microstructures, a higher order Ising model is used by linking all the lattice points as illustrated in Figure 2.1 (c) [56]. This structure defines an MRF where the joint probability density of all particles is defined by the local Markovian property which indicates that the probability of a value (X) is conditionally independent of all other values that are placed outside of its neighbors. The graphical network is designed in a way to have conditional dependence on its neighbors exhibiting a joint probability distribution globally. An important feature of the MRF algorithm is the Window Size (WS). It is defined as the size of a square neighborhood window around a pixel of interest located at the center and bonding it to every other pixel within the window (Figure 2.1 (b)). The window size is a crucial adjustable parameter during MRF reconstruction. While smaller window sizes can cause more uncertainty to propagate on the synthetic model, choosing larger window sizes is computationally expensive. Hence, determining an optimum window size is essential to reconstruct synthetic microstructures.

The algorithm initiates its first step by randomly selecting a $W \times W$ (pixel^2) seed window (where $W << N$) from the experimental image and transfers it to the center of the synthetic image. Since the location of the seed window is selected at random, one can create multiple synthetic images from the same experimental image. The resemblance between the experimental and synthetic window results from solving a minimum distance problem as described in [28]. In order to find the value of the unfilled pixel, the algorithm performs an exhaustive search. During the search, the algorithm looks for a neighborhood window in the input microstructure image that matches well with the neighborhood window of the synthetic model. The matching between both windows is measured through a distance parameter [28]. Among all the neighborhood windows in the input image that satisfy the threshold condition [28], one of them is randomly chosen and the center pixel of the chosen window is taken to be the pixel intensity of the unfilled pixel. Next, the algorithm moves around in a clockwise direction filling each of the unfilled pixels. For the RGB image, the above-mentioned procedure is repeated for all three color channels. If none of the neighbors are filled in the synthetic model, then the threshold is raised by a small percentage. Then, the algorithm moves the window outwards from the center of the synthetic image in a clockwise direction, and it determines the pixel intensity of the next unfilled pixel. The algorithm repeats this process by incrementally moving the synthetic window clockwise until the reconstruction of the synthetic surface topography map is complete [56].

Due to a large number of variables in color images, the mathematical construction is subjected to model uncertainty as the MRF algorithm works using joint probability distributions. While the stochastic nature of the MRF algorithm is a beneficial feature, the randomness (epistemic) can still give rise to uncertainty. Furthermore, the unavailability of the correct pixel intensity information (aleatoric) in the microstructure image can also introduce uncertainty. This is because the microstructures are inherently stochastic due to the uncer-

tainties arising from the unanticipated fluctuations in stress and thermal gradients during thermo-mechanical processing (processing-induced or aleatoric uncertainty). More about the source of uncertainty is described in detail in Chapter 4. Therefore, a single experimental microstructure sample is not representative of all features of the entire specimen and there are several possible outcomes for synthetic images. The goal of MRF is to achieve a "statistically-equivalent" microstructure, rather than the exact same microstructure. However, during reconstruction, incorrect pixel intensity values might propagate on the synthetic samples due to uncertainty. Even a slight change in one of the color channels may alter the color of the reconstructed pixel and affect the subsequent process. Therefore, it is important to use a quantifiable parameter that not only captures the resemblance of two images as a whole but also accounts for the uncertainty of the algorithm by explicitly comparing the original and synthesized images. The present work uses Hu moments [77] to investigate this important challenge. The application of moment invariants, which are derived from Hu moments, to compare and verify the original and synthesized microstructures are explained in the next section.

2.3 Computational Characterization of Microstructures

The MRF algorithm generates statistically equivalent microstructures. Hence, it is crucial to validate the synthetic microstructures reconstructed from experimental data. The key to validating the reconstructed microstructures lies in characterizing microstructural features. One such important feature is the grain shape which also relates to the texture of the microstructure. The characterization and quantification of grain shapes of polycrystalline microstructures are significant to verify the reconstructed microstructure images and understand the effects of different grain shapes on homogenized material properties. How-

ever, the broad variety and intricate nature of grain shapes including highly non-convex or concave grains [105] poses a challenge for grain shape quantification. Therefore, a universal approach is necessary to characterize and quantify grain shapes. This work focuses on developing metrics to ubiquitously describe the grain shapes of any microstructure.

Many practical methods to quantify the grain shapes are based on intuitive approaches involving experiments [106, 107]. Moreover, Fourier analysis has also been used in the past for the classification of crystal shapes [108]. Another idea was the utilization of the Minkowski functions [109], which are mostly used in the field of astronomy [110], to characterize 3D microstructures [111]. The traditional approach is to perform a visual inspection for grain mapping that does not lead to any quantitative information [89]. Another novel approach for determining the validity of 3D reconstructed grains from 2D maps is utilizing the surface projection error [112], which only includes information about the diameter and volume of the grains and therefore does not capture any detailed shape information. Other than the aforementioned techniques, the attempts to characterize microstructural features can widely be classified as statistical functions and physical descriptors. The statistical functions can further be sub-classified into point-based or line-based functions. For example, the widely-used two-point correlations [113, 114, 115] do not maintain sufficient information to analyze the statistical equivalence of microstructures and, thus, they cannot provide explicit information about the grain shape.

A similar yet more informative physical descriptor is the 2-point cluster correlation, which can be used to quantify the microstructure in 2D and 3D domains [89]. However, they do not explicitly determine the size and shape of individual grains [116]. Unlike point-based functions, line-based comparisons are also attempted [28, 55] using linear path functions that do not explicitly capture the local-level microstructure features, such as the grain shape. On the other hand, the physical descriptors can be used to check the statistical equivalency between

the features of the original and reconstructed microstructures. The geometrical shape-based descriptors are introduced for quantifying the microstructure topology [55]. However, these descriptors are not ideal for quantifying complex grain shapes, such as those resulting from additive manufacturing techniques. None of the shape descriptors and correlation functions discussed above explicitly capture the grain shapes. Therefore, they cannot be used as universal metrics to characterize different grains. A quantitative scheme that can explicitly compare grain shapes was not developed previously.

However, a notable characterization technique for shape quantification is the shape quotient [117]. The shape quotient, which is based on the isoperimetric inequality, is invariant to affine transformation [118]. However, the shape quotient is more of a compactness measure of shape with respect to a common geometry like a circle for the 2D case or an ellipsoid/sphere for the 3D case. The shape quotient can only measure the shape of the object while the moment invariant can also capture the changes in the orientations (texture) of the microstructure by considering the changes in the pixel intensity of the image samples.

The moments stand out from other shape descriptors by their quality of invariance to different shapes. In this work, the goal is to build a quantitative verification approach based on image moments that will compute both global-level (volume-averaged) and local-level (grain scale) features of the synthesized microstructures generated with the MRF for both 2D and 3D. The moment invariants are used in diverse fields, ranging from simple object shape detection to human face recognition [119, 120, 121, 122, 123, 124, 125, 126]. For instance, Žunić [127, 128, 129, 130] studied the application of the first Hu moment to measure the circularity, ellipticity, and ellipsoidness of 2D and 3D shapes. The use of moment invariants in materials science, particularly for grain shape recognition, is a relatively new research area. The application of moment invariants for measuring shapes has also been investigated to quantify grain shapes of 2D and 3D microstructures [105, 117, 131, 132, 133, 134, 135,

136]. More recently, the use of moment invariants as a grain shape descriptor was found applicable by Callahan et al. [105, 133], MacSleyne et al. [117, 134, 135], and DeGraef [136] for both 2D and 3D microstructures. MacSleyne et al. [117] discussed the applications of dimensionless moment invariants (denoted by ω_1 and ω_2) and introduced normalized moments as a shape descriptor, specifically for 3D microstructures [134, 135]. Additionally, moment invariants are derived for standard 2D and 3D geometric shapes [105, 135, 135] for classifying particle shapes [105], compare experimental and synthetic grains [134], and for the quantification and analysis of precipitate grain shapes [119, 134, 135]. However, these methods do not work well for the highly irregular grain shapes of additively manufactured materials. To address this problem, the present study aims to quantify the grain shapes of microstructures without the need of comparing them to another geometry. The shape moments are invariant with respect to Rotation, Scale, and Translation (RST), and thus become a preferable choice for quantifying grain shapes. Different measures to quantify the effects of the uncertainty affecting the 2D and 3D grain shapes of microstructures are also explored using these descriptors. The moment invariants were formulated by Hu as a special set of image moments that are invariant to RST transformations [123]. In an image, the Hu moments describe the distribution of the pixel intensities over the image while remaining invariant to shape transformation. The image moments have been applied in this work to compare experimental and synthesized 2D microstructure images at global and local levels [56]. In addition, the present work proposes to use the concept of moment invariants to study the uncertainty propagation on the grain features of 2D and 3D synthetic microstructures [57, 59].

A moment as defined in classical mechanics is a product of a physical quantity and distance between where it is applied and a reference point. The mathematical concept of a moment in image processing is the same as this physical meaning. For an image, pixel intensity is a

random variable distributed over the image discretely. Therefore, a moment of an image is a measure of an average weighting number based on each pixel's intensity. Since an image is a 2D figure, the moments derived in the following sections are for 2D spaces. The basic type of a moment is called a raw moment. It is defined as the summation of the product of each pixel's location and its corresponding pixel intensity. To determine the location of pixels, the images are graphically expressed over a Cartesian coordinate system (x, y).

$$m_{ij} = \sum_{x} \sum_{y} x^i y^i I(x, y) \tag{2.1}$$

Equation 2.1 demonstrates the definition of the raw moment, where $i, j = 0, 1, 2, ..., N$ with N representing the order of the moment. The zeroth and first-order raw moments can yield two important properties that are used to calculate more advanced moments. When $i = j = 0$, the raw moment also statistically signifies its equivalence to the expected mean which is defined for a discrete random variable as m_{00}. Hence, m_{00} can also be thought of as the expected value of the image. It can also be called the image area since m_{00} is the summation of all the pixel intensities of an image. Another property that can be derived from the first-order raw moments is called the centroid ($\bar{x}$ and $\bar{y}$). The centroid is defined as the ratio of the first-order moment (m_{10}, m_{01}) with respect to the image area. It represents the geometric center of an image.

$$\bar{x} = \frac{m_{10}}{m_{00}}, \quad \bar{y} = \frac{m_{01}}{m_{00}} \tag{2.2}$$

$\bar{x}$ and $\bar{y}$ represent the coordinates of the centroid of the image. μ_{ij} is a subset of another type of moment called the central moment. It is estimated through raw moments but each of the pixel locations is subtracted from their centroid coordinates of the image as formulated

in Equation 2.3.

$$\mu_{ij} = \sum_{x} \sum_{y} (x - \bar{x})^i (y - \bar{y})^i I(x, y) \tag{2.3}$$

The first-order central moment is always zero and the second-order central moments are statistically equivalent to the variance. An important characteristic of the central moment is that it is invariant. For instance, μ_{ij} is invariant to the translation of shapes. A scale invariant is introduced by normalizing the central moments by the image area to the power of γ. This is called as normalized central moment, (η_{ij}), given as:

$$\eta_{ij} = \frac{\mu_{ij}}{(m_{00})^\gamma} \; where \; \gamma = \frac{2 + i + j}{2} \tag{2.4}$$

The use of a central or normalized central moment, however, does not provide a complete one-to-one image comparison as they are not invariant to rotations. A quantity that is invariant to the rotation, scale, and translation of shapes is available using the set of seven moments (Equation 2.5) defined by Hu [77].

$$
\begin{aligned}
\phi_1 &= \eta_{20} + \eta_{02} \\
\phi_2 &= (\eta_{20} - \eta_{02})^2 + 4\eta_{11}^2 \\
\phi_3 &= (\eta_{30} - 3\eta_{12})^2 + (3\eta_{21} - \eta_{03})^2 \\
\phi_4 &= (\eta_{30} + \eta_{12})^2 + (\eta_{21} + \eta_{03})^2 \\
\phi_5 &= (\eta_{30} - 3\eta_{12})(\eta_{30} + \eta_{12})[(\eta_{30} + \eta_{12})^2 - 3(\eta_{21} + \eta_{03})^2] \\
&+(3\eta_{21} - \eta_{03})(\eta_{21} + \eta_{03})[3(\eta_{30} + \eta_{12})^2 - (\eta_{21} + \eta_{03})^2] \\
\phi_6 &= (\eta_{20} - \eta_{02})[(\eta_{30} + \eta_{12})^2 - (\eta_{21} + \eta_{03})^2] \\
&+4\eta_{11}[(\eta_{30} + \eta_{12})(\eta_{21} + \eta_{03})] \\
\phi_7 &= (3\eta_{21} - \eta_{03})(\eta_{30} + \eta_{12})[(\eta_{30} + \eta_{12})^2 - 3(\eta_{21} \\
&+\eta_{03})^2] - (\eta_{30} - 3\eta_{12})(\eta_{21} + \eta_{03})[3(\eta_{30} + \eta_{12})^2 - (\eta_{21} + \eta_{03})^2]
\end{aligned}
\tag{2.5}
$$

Furthermore, many different moments that provide similar invariant properties to Hu moments can be developed. For example, MacSleyne et al. [135] has developed a dimensionless moment invariant (ω) to quantify grain shapes and precipitates. In addition, the possibility of developing a graphical map based on the moment invariants is also investigated by MacSleyne et al. [135] to quantify and characterize the grain shapes. However, moment invariants have not been explored for uncertainty quantification. This work develops a formulation based on shape moment invariants to investigate the effects of uncertainty as explained in Chapter 4.

The central moments are developed in the form of multivariate distributions. Hence, the second-order central moments represent the variance (μ_{20}, μ_{02}) and covariance (μ_{11}) of an image while the third-order normalized central moment contains the skewness information of the same image. Similarly, a fourth-order moment provides information about the kurtosis of the image. The present work focuses on the utilization of the second-order Hu moments,

which are used to quantify grain shapes. Interested readers are referred to [137] for more information about the statistical meaning of the higher-order Hu moments.

By calculating all the second-order central moments, the covariance matrix can be formed as:

$$\begin{bmatrix} \Sigma_{xx} & \Sigma_{xy} \\ \Sigma_{xy} & \Sigma_{yy} \end{bmatrix} = \begin{bmatrix} \mu_{20} & \mu_{11} \\ \mu_{11} & \mu_{02} \end{bmatrix} \tag{2.6}$$

Similarly, a 2×2 covariance matrix for the normalized central moments can be defined as:

$$\begin{bmatrix} \eta_{20} & \eta_{11} \\ \eta_{11} & \eta_{02} \end{bmatrix} \tag{2.7}$$

The eigenvalues of Equation 2.7can be formulated in terms of the Hu moments, as follows:

$$\lambda_{1/2} = \frac{\phi_1 \pm \sqrt{\phi_2}}{2} \tag{2.8}$$

The eigenvalues of this matrix yield PEM denoted by λ. The present work uses the Principal Eigenvalue Moments (PEM) denoted by Equation 2.8 to develop a graphical domain and derive five parameters to quantify the uncertainty arising from the reconstruction of 2D and 3D microstructures. A similar approach was presented earlier [134, 135] with a map of ω_1 and ω_2 for comparing grain shapes. Here, ω_1 and ω_2 are the dimensionless moment invariants. The map developed from these moments can be used to characterize the grain and particle shapes. However, in this work, the focus is on quantifying the uncertainty propagated on the reconstructed microstructures with a map of PEM. Significant statistical parameters based on the PEM moments that can be used to study the uncertainty quantification of reconstruction methods have been developed in this work and described in detail in Chapter 4. Furthermore, the PEM map can be used as a universal measure for understanding the

uncertainty propagated on both 2D and 3D reconstructed microstructures.

Chapter 3

RESULTS AND MODEL VERIFICATION

The MRF algorithm, as discussed in Chapter 2, is applied to reconstruct the microstructure images of Ti-7Al samples that are forged and additively manufactured (presented in Figure 3.1 (a) and Figure 3.1 (b), respectively). The microstructure images are obtained through the EBSD technique in the SEM device [38]. The EBSD images contain information about the microstructural topology. The RGB colors in an EBSD image represent a crystallographic orientation. The MRF algorithm reconstructs the synthetic images by building statistics of the pixel intensity values of the input (EBSD) image. However, computational reconstruction aims to predict a statistically equivalent microstructure. Therefore, it is crucial to verify the reconstructed microstructures.

This chapter is structured as follows: Section 3.1 presents the results of the synthetic microstructures reconstructed with the MRF algorithm. Section 3.2 presents the computational time consumed for generating reconstructed microstructure images. Section 3.3 discusses the two-stage methodology developed to verify the 2D synthetic microstructures with respect to the experimental data and Section 3.4 discusses the procedure to verify the 3D synthetic microstructures reconstructed by the MRF algorithm.

3.1 Synthesized microstructures of MRF

The synthetic microstructures are reconstructed using the EBSD data of Ti-7Al samples fabricated with conventional forging (Figure 3.1 (a)) and additive manufacturing (Figure 3.1 (b)) [38]. The reconstruction is performed for the same size and higher resolution (1.5 times (1.5×) and 2 times (2×) larger images than the original image) using window sizes of 5, 7, and 9. In each case, a hundred images are generated to find the efficiency of the MRF algorithm and optimum window size. The results are presented in Figure 3.2 and Figure 3.3 for the same size reconstruction. The results for higher resolution cases are presented in Figures 3.4 - 3.7.

To reduce the effects of the algorithmic uncertainties, a strategy is developed for filtering the reconstructed images using the Hu moments and without biasing the MRF process. Every time an image is reconstructed by the MRF, this strategy (i) converts the reconstructed image into grayscale, (ii) calculates the Hu moments for the entire grayscale image, and (iii) saves the reconstructed image only if certain conditions based on the Hu moments are satisfied. These conditions are defined in terms of the first (ϕ_1) and second (ϕ_2) Hu moments. The ϕ_1 and ϕ_2 values of the synthesized images satisfy the following conditions: error percentages of $e_{\phi_1}<2\%$ (error in ϕ_1) and $e_{\phi_2}<10\%$ (error in ϕ_2) with respect to the Hu moments of the original image in grayscale. When the resolution is higher, it takes more time to find the images satisfying these filtering conditions. To limit the required computational time, in the forged 2× case (when the synthesized samples are 2 times larger than the original), only the first filtering condition ($\phi_1<2\%$) is used. The percentage values are chosen based on trials. For filtering, the image is converted into grayscale for improving computing times. The ϕ_1 and ϕ_2 values used for filtering are purely based on the second-order moment. The third and higher-order moments are found to be too sensitive when used as filtering criteria. Also,

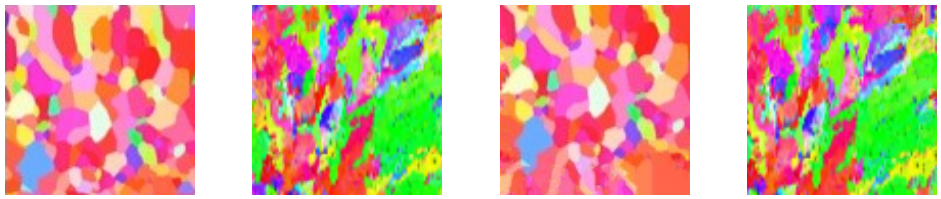

(a) (b) (c) (d)

Figure 3.1: Experimental and reconstructed images (a) Experimental forged image with a resolution of 100x100 pixels, (b) Additively manufactured image with a resolution of 93x93 pixels, (c) Reconstructed forged image of 100x100 pixels using window size (WS) of 5 with error percentages of ϕ_1=1.09%, ϕ_2=12.35%, ϕ_3=238.51%, ϕ_4=77.60%, ϕ_5=97.78%, ϕ_6=96.32%, ϕ_7=82.56%. (d) Reconstructed additively manufactured image of 93x93 pixels with WS of 5 with error percentages of ϕ_1=0.25%, ϕ_2=1.49%, ϕ_3=69.87%, ϕ_4=25.30%, ϕ_5=80.80%, ϕ_6=329.81%, ϕ_7=53.71% [56].

the order of magnitude for the higher-order moments (third and higher) is extremely low [56]. This is because when the central moments are divided by the pixel area which is of higher magnitude than the central moment, the resulting value becomes rather small. While the third and higher order moments can assure the presence of uncertainty even when the images are visually satisfying (Figure 3.1 (c), (d)), including them for filtering the synthesized samples is infeasible due to the computational time requirements.

The similarity of individual synthetic grains to the grains of the experimental image is studied better through the difference in the magnitudes of the Hu moments without the need to compare them to common geometrical shapes. A small change in the size or shape of the grain can directly be measured by the Hu moment values. Hence, in this work, the reconstructed image is compared to the original image on two levels. In the first level, global parameters are defined to describe the whole image by accounting for each and every pixel intensity in all three color channels. In the second level, a local measure is defined to compare the size and shape of each grain.

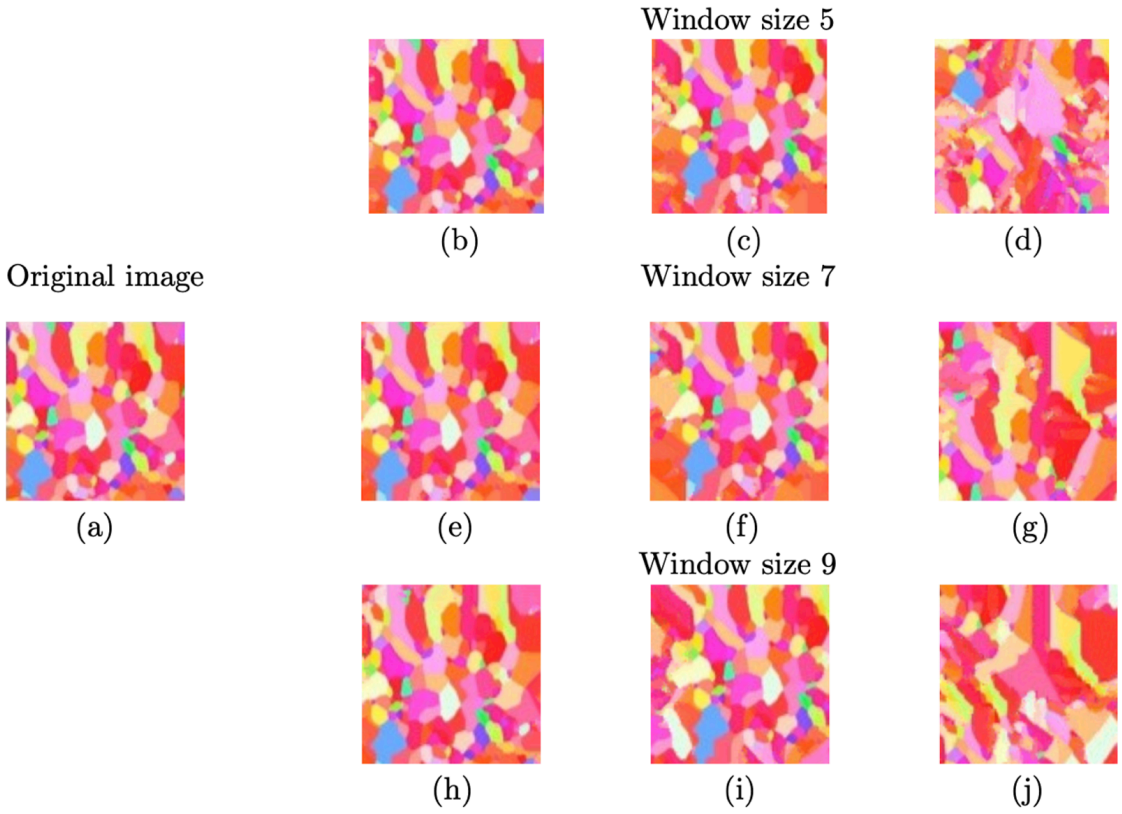

Figure 3.2: Original experimental forged image (100x100 pixels) versus the same-size reconstructed images (100x100 pixels) of Ti-7Al. (a) Original image. Reconstructed images: (b) Type 1 acceptable image of WS 5, (c) Type 2 acceptable image of WS 5, (d) Eliminated image of WS 5, (e) Type 1 acceptable image of WS 7, (f) Type 2 acceptable image of WS 7, (g) Eliminated image of WS 7, (h) Type 1 acceptable image of WS 9, (i) Type 2 acceptable image of WS 9, and (j) Eliminated image of WS 9 [56].

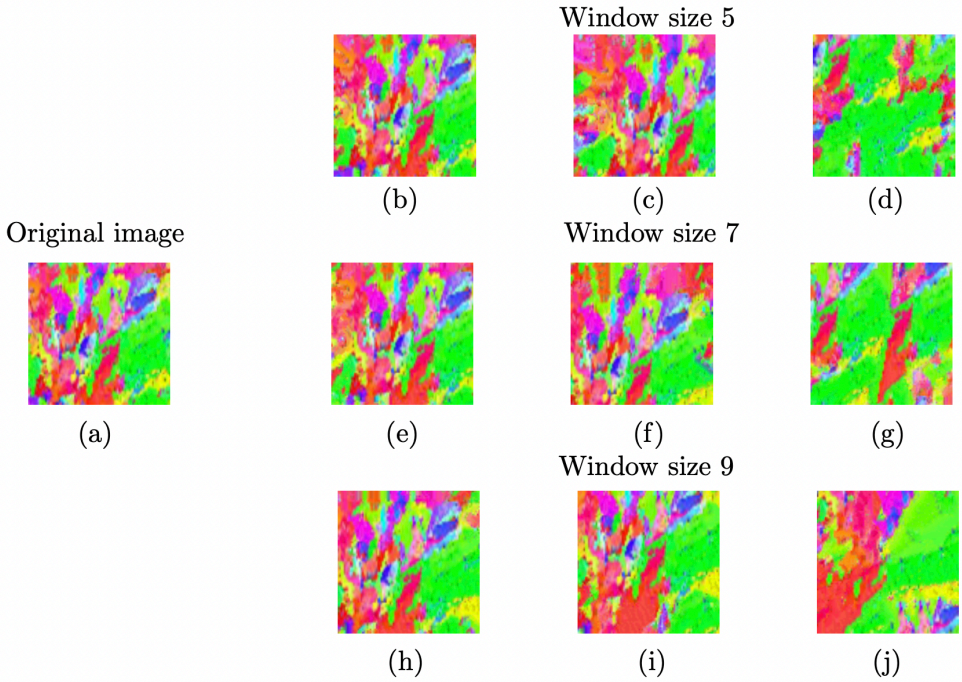

Figure 3.3: Original additively manufactured experimental image (93x93 pixels) versus the same-size reconstructed images (93x93 pixels) of Ti-7Al. (a) Original image. Reconstructed images: (b) Type 1 acceptable image of WS 5, (c) Type 2 acceptable image of WS 5, (d) Eliminated image of WS 5, (e) Type 1 acceptable image of WS 7, (f) Type 2 acceptable image of WS 7, (g) Eliminated image of WS 7, (h) Type 1 acceptable image of WS 9, (i) Type 2 acceptable image of WS 9, and (j) Eliminated image of WS 9 [56].

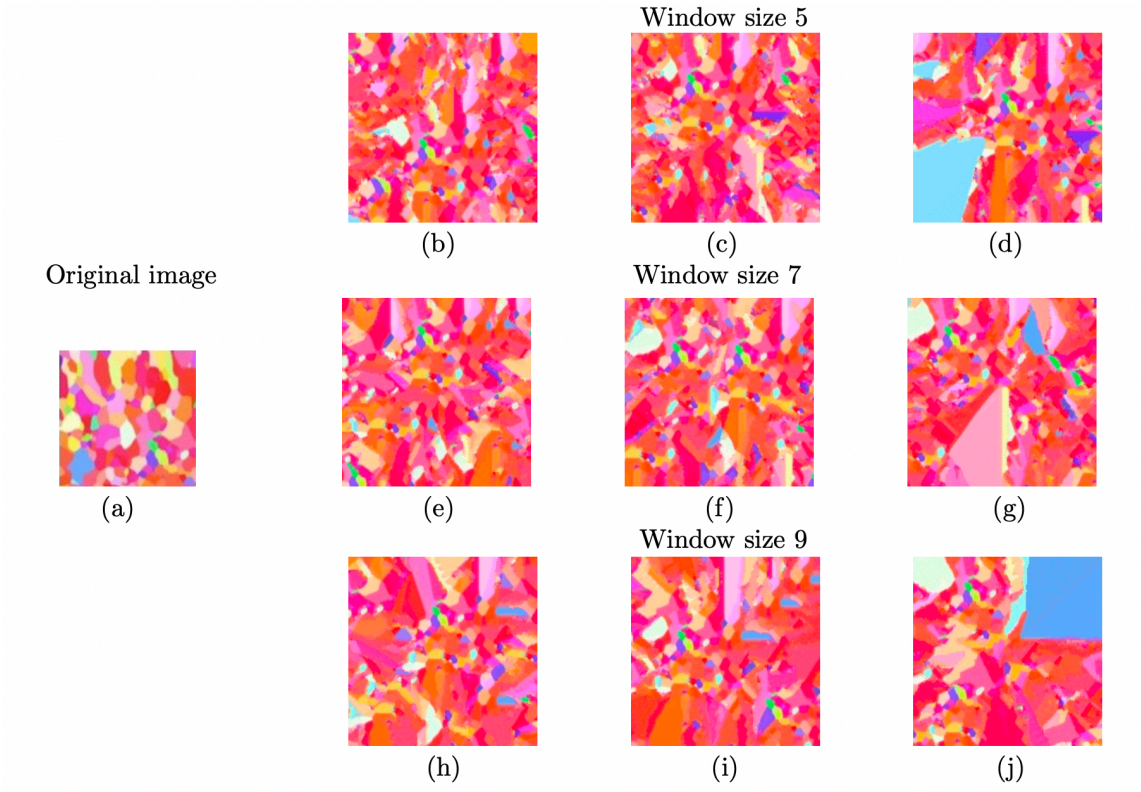

Figure 3.4: Original experimental forged image (100x100 pixels) versus 1.5x reconstructed images (150x150 pixels) of Ti-7Al. (a) Original image. Reconstructed images: (b) Type 1 acceptable image of WS 5, (c) Type 2 acceptable image of WS 5, (d) Eliminated image of WS 5, (e) Type 1 acceptable image of WS 7, (f) Type 2 acceptable image of WS 7, (g) Eliminated image of WS 7, (h) Type 1 acceptable image of WS 9, (i) Type 2 acceptable image of WS 9, and (j) Eliminated image of WS 9 [56].

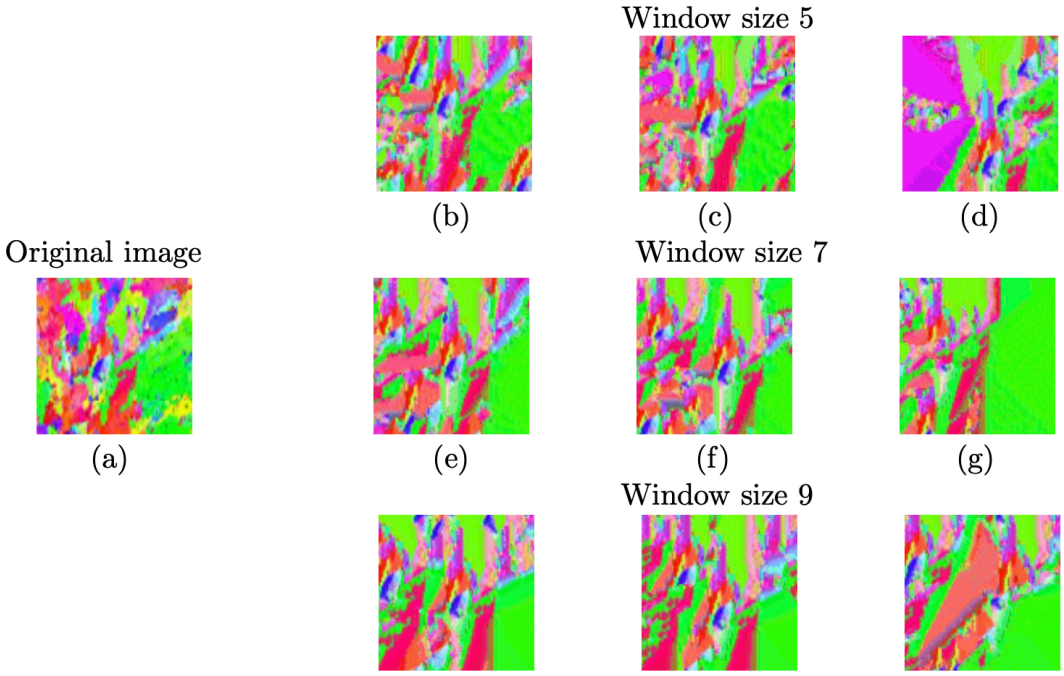

Figure 3.5: Original additively manufactured experimental image (93x93 pixels) versus 1.5x reconstructed images (69x69) of Ti-7Al. (a) Original image from which a 46x46 image is cut from the center for reconstruction. Reconstructed images: (b) Type 1 acceptable image of WS 5, (c) Type 2 acceptable image of WS 5, (d) Eliminated image of WS 5, (e) Type 1 acceptable image of WS 7, (f) Type 2 acceptable image of WS 7, (g) Eliminated image of WS 7, (h) Type 1 acceptable image of WS 9, (i) Type 2 acceptable image of WS 9, and (j) Eliminated image of WS 9 [56].

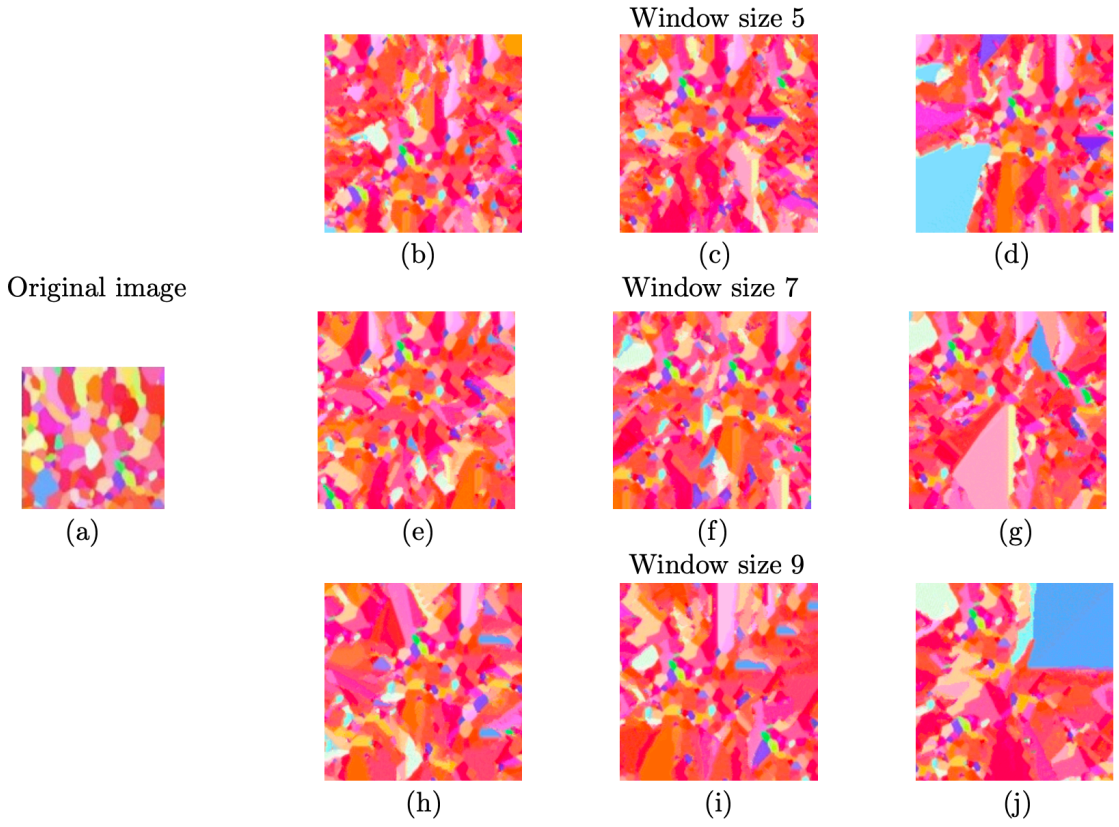

Figure 3.6: Original experimental forged image (100x100 pixels) versus 2x reconstructed images (178x178) of Ti-7Al (a) Original image from which a 78x78 image is cut. Reconstructed images: (b) Type 1 acceptable image of WS 5, (c) Type 2 acceptable image of WS 5, (d) Eliminated image of WS 5, (e) Type 1 acceptable image of WS 7, (f) Type 2 acceptable image of WS 7, (g) Eliminated image of WS 7, (h) Type 1 acceptable image of WS 9, (i) Type 2 acceptable image of WS 9, and (j) Eliminated image of WS 9 [56].

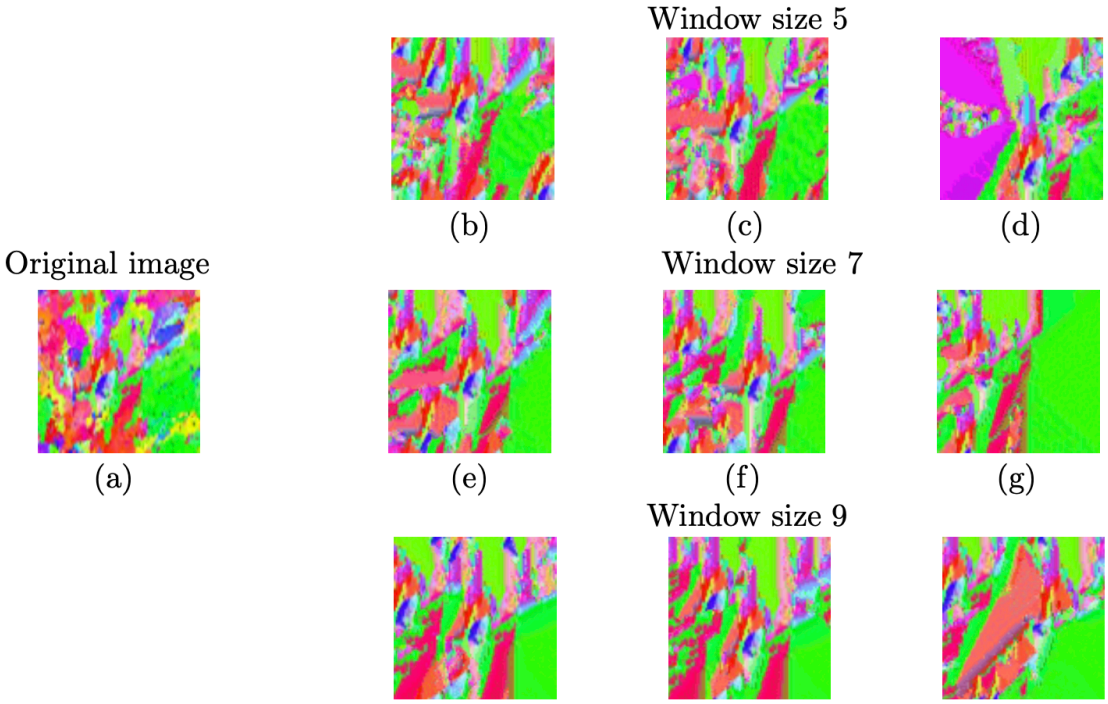

Figure 3.7: Original additively manufactured experimental image (92x92 pixels) from which a small image of size 46x46 is cut from the center for reconstruction versus 2x reconstructed images (92x92) of Ti-7Al (a) Original image. Reconstructed images: (b) Type 1 acceptable image of WS 5, (c) Type 2 acceptable image of WS 5, (d) Eliminated image of WS 5, (e) Type 1 acceptable image of WS 7, (f) Type 2 acceptable image of WS 7, (g) Eliminated image of WS 7, (h) Type 1 acceptable image of WS 9, (i) Type 2 acceptable image of WS 9, and (j) Eliminated image of WS 9 [56].

3.2 Computational time

The computational time of the reconstruction is formulated in Table 3.1. The spread of the color range reveals that the additively manufactured sample requires less time to be reconstructed than the forged sample in some of the higher-resolution cases. Table 3.1 shows the required computational times for each window size, which is normalized by the time required for the window size 5. As it can be seen from Table 3.1, the average computational time ratio increases with increasing window size in each resolution case. Hence, window size 9 has the highest computational time. The computational time depends on the image size of the reconstructed sample. For an image of 100 × 100 resolution, it would take approximately 45 s in a moderate computational platform (such as a desktop computer) for the same size reconstruction while the higher resolutions (1.5× and 2×) would respectively take 2 and 3 times more without any constraints. Additionally, any constraints on reconstruction as presented in this work would require slightly more computational time. (See Table 3.1.)

Table 3.1: Computational time [56]

Resolution	Window size	Total time ratio	
		Conventional forged	Additively manufactured
Same size	WS5	1	1
	WS7	2.34	2.77
	WS9	3.07	4.27
1.5x	WS5	1	1
	WS7	1.45	1.24
	WS9	1.56	1.61
2x	WS5	1	1
	WS7	1.49	1.89
	WS9	3.94	3.66

3.3 Verification methodology for 2D reconstructed images

For reconstruction algorithms such as MRF that require only one input image to generate multiple samples, a methodology needs to be implemented to verify the synthetic data. It is crucial to statistically validate the synthesized images with respect to the experimental image. To achieve a high-fidelity and statistically similar representation of the original experimental image, the synthesized samples are assessed according to their global and local level features. At the global level, the whole microstructure images are compared to each other. At the local level, individual grains are compared through their shapes and sizes. Moment invariants are applied for both global and local level comparisons. First, at the global level, the difference in the largest eigenvalues of the second-order normalized covariance matrix (Equation 2.7) is used to identify the reconstructed images which resemble the original the most. Furthermore, a distance parameter (described in Section 3.3.1) measuring the distance between the centroid of two images is also included at the global level. At the local level, the grains of the EBSD images are separated. Each grain is quantified through the first Hu moment and the grain sizes are measured through an equivalent radius parameter.

3.3.1 Global level

The global level involves comparing the topology of the reconstructed microstructure with the experimental image. Therefore, at the global level, the whole microstructure images of the experimental and reconstructed samples are compared. In an image, the pixel intensity ranging from $0-255$ for all the three color (RGB) channels is spread in both x and y directions as a discrete function. Determining the variance of pixel intensities can give the data spread

in one direction (horizontal spread Σ_{xx} or vertical spread Σ_{yy}). Here, the data changes in a 2D space. Therefore, the covariance (Σ_{xy}) is also needed to represent the data spread in the image. The second-order central moment represents the variance and covariance values of the image. The covariance here defines how pixel intensity is varying in both x and y directions. The percentage difference (δ_{λ_1}) between the largest PEM (λ_1) quantifying the experimental ($\lambda_{1,E}$) and synthesized images ($\lambda_{1,S}$) is used at the global level to verify the reconstructed samples along with a distance parameter defined in the following equation.

$$d_{cr} = \sqrt{(\bar{y_S} - \bar{y_E})^2 + (\bar{x_S} - \bar{x_E})^2} \tag{3.1}$$

where S and E represent the synthetic and experimental data, respectively, and d_{cr} shows the Euclidean distance between the centroid points of the experimental ($\bar{x_E}$ & $\bar{y_E}$) and synthetic ($\bar{x_S}$ & $\bar{y_S}$) images. Therefore, d_{cr} is defined as a measure of similarity between the distributions of pixel intensity values. If the MRF takes the seed image from the center region, then the reconstructed image would resemble the original more, assuming that the level of the algorithmic uncertainty would be smaller. However, if the seed image is selected from the corner of the original image, then the reconstruction begins around the corner and the resulting synthesized image can look slightly different than the original. Therefore, d_{cr} can represent how far the seed image is taken from the center. Unlike the PEM, d_{cr} is not a geometric measure as it depends on the distribution of the pixel intensity. At the global level, the d_{cr} parameter assists the PEM in filtering the acceptable images from a pool of synthesized samples. The selected cut-off value for the error percentage (δ_{λ_1}) and d_{cr} varies for different images. The cut-off value for δ_{λ_1} is set to 3% for the forged sample, and 10% for the additively manufactured samples. The cut-off value for d_{cr} is set to be 1 for both cases. All the cut-off values are chosen based on trial and error. The synthesized images that satisfy the cut-off values are defined as acceptable samples. However, it is important to

note here that the cut-off values are also affected by the filtering conditions described earlier in Section 3.1. Therefore, the cut-off values are subjected to change for different types of microstructural images.

The acceptable images at the global level are further categorized into two types. Type-1 reconstructed samples are the images that satisfy both the global filtering conditions (For example, $\delta_{\lambda_1} < 3\%$ & $d_{cr} < 1$ for the conventionally forged case). Type-2 reconstructed samples are the images that only satisfy the eigenvalue global filtering condition (For example, $\delta_{\lambda_1} < 3\%$ for the conventionally forged case). For some microstructure images, as the color density of the microstructure image increases, the uncertainty propagating on the grain shapes of reconstructed images increases as well. This needs the inclusion of more than one constraint to filter out noisy images. Examples of Type-1 acceptable images of the same size reconstruction are presented in Figure 3.2 (b), (e), and (h) for the conventionally forged and Figure 3.3 (b), (e), and (h) for the additively manufactured samples. Similarly, for the higher resolution cases (1.5× and 2×), the Type-1 acceptable images are presented in Figure 3.4 - 3.7 (b), (e), and (h). The Type-1 acceptable images are the closest to the original in terms of the defined global level measures. Hence, these images have the least average Hu moment error represented by the blue curves in Figures 3.8 - 3.10 for each window size.

Type-2 is defined as the acceptable images satisfying the filtering conditions only for δ_{λ_1}. Therefore, d_{cr} is greater than 1 for the Type-2 acceptable images. Hence, they are not as close to the original as the Type-1 but still statistically similar to the experimental image with low levels of uncertainty. The difference between Type-1 and Type-2 can be because the seed image can be selected from a corner region of the experimental image. To demonstrate the dissimilarity between the Type-1 and Type-2 images, all the reconstructed images are quantified by Hu moments and compared to the original image. The difference in the two types of acceptable images can be observed in the graphical plots of Figure 3.8 (same size)

and Figure 3.9 - Figure 3.10 (higher resolution) where the average Hu moment errors of the Type-2 acceptable images are above the curves of the Type-1 acceptable images. Examples of Type-2 acceptable images are presented in Figure 3.2 and Figure 3.3 (c), (f), and (i). Thus, together with the δ_{λ_1} and d_{cr}, the global parameters help with identifying the acceptable images from the whole pool of reconstructed samples.

Because of the uncertainty of the experimental images and the algorithmic randomness, the MRF can also produce images with high uncertainty, as presented in Figure 3.2 - 3.7 (d), (g), and (j) for the same size and higher resolution reconstruction. However, they are eliminated in this work using global measures. From the graphs of Figures 3.8 - 3.10, it can be observed that the red curves, which represent the eliminated reconstructed images, have high uncertainty reflected in the error percentages of the Hu moments. The blue and black curves again prove that Type-1 has the least error percentage for the Hu moments with respect to the original image, thereby validating the categorization method based on the eigenvalues and distance parameters at the global level. The curves in Figures 3.8 - 3.10 also prove that as the order of moment increases, its sensitivity to the change in the pixel intensity also increases. Thus, the error percentages of the third-order moments (ϕ_3 and ϕ_4) in the eliminated samples are much higher.

Table 3.2 shows the percentage of acceptable images among the 100 reconstructed images for each case. Even though a particular window size may produce more acceptable images in each category, there are repetitions of the reconstructed images, especially in higher window sizes of the forged (window size 9) and additively manufactured (window size 7, window size 9) samples. This means more possible solutions can be obtained with the MRF algorithm if the image has a diverse color range, as observed in the forged alloy. Additionally, all three window sizes seem to have the ability to produce good results (for example, Type-1 results in Figures 3.8 - 3.10). Therefore, more parameters are required to decide the optimum window

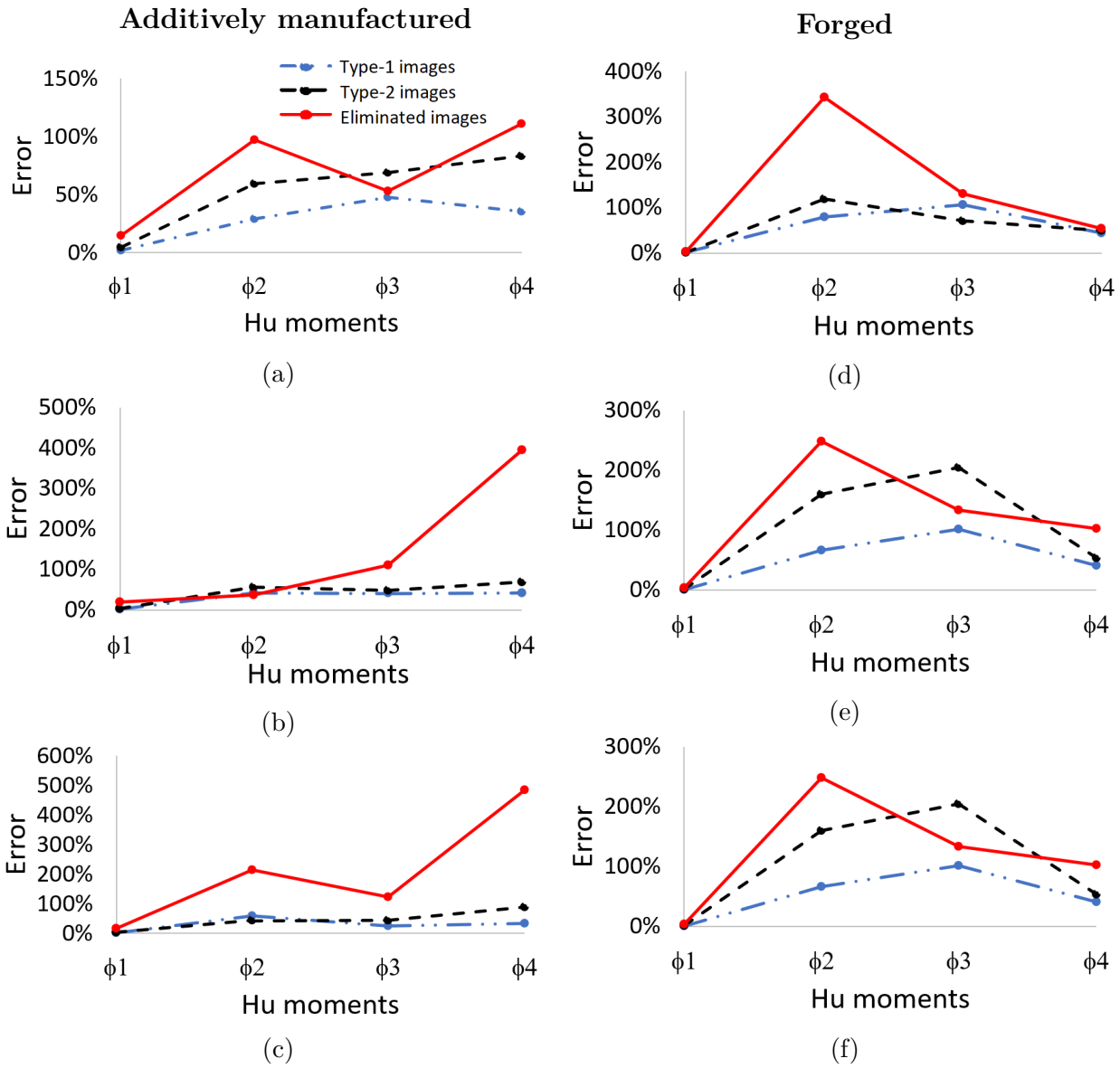

Figure 3.8: Average error percentage plots of the same size synthesized images for the additively manufactured microstructure with (a) WS 5, (b) WS 7 and (c) WS 9 and for the forged microstructure with (d) WS 5, (e) WS 7, and (f) WS 9 [56].

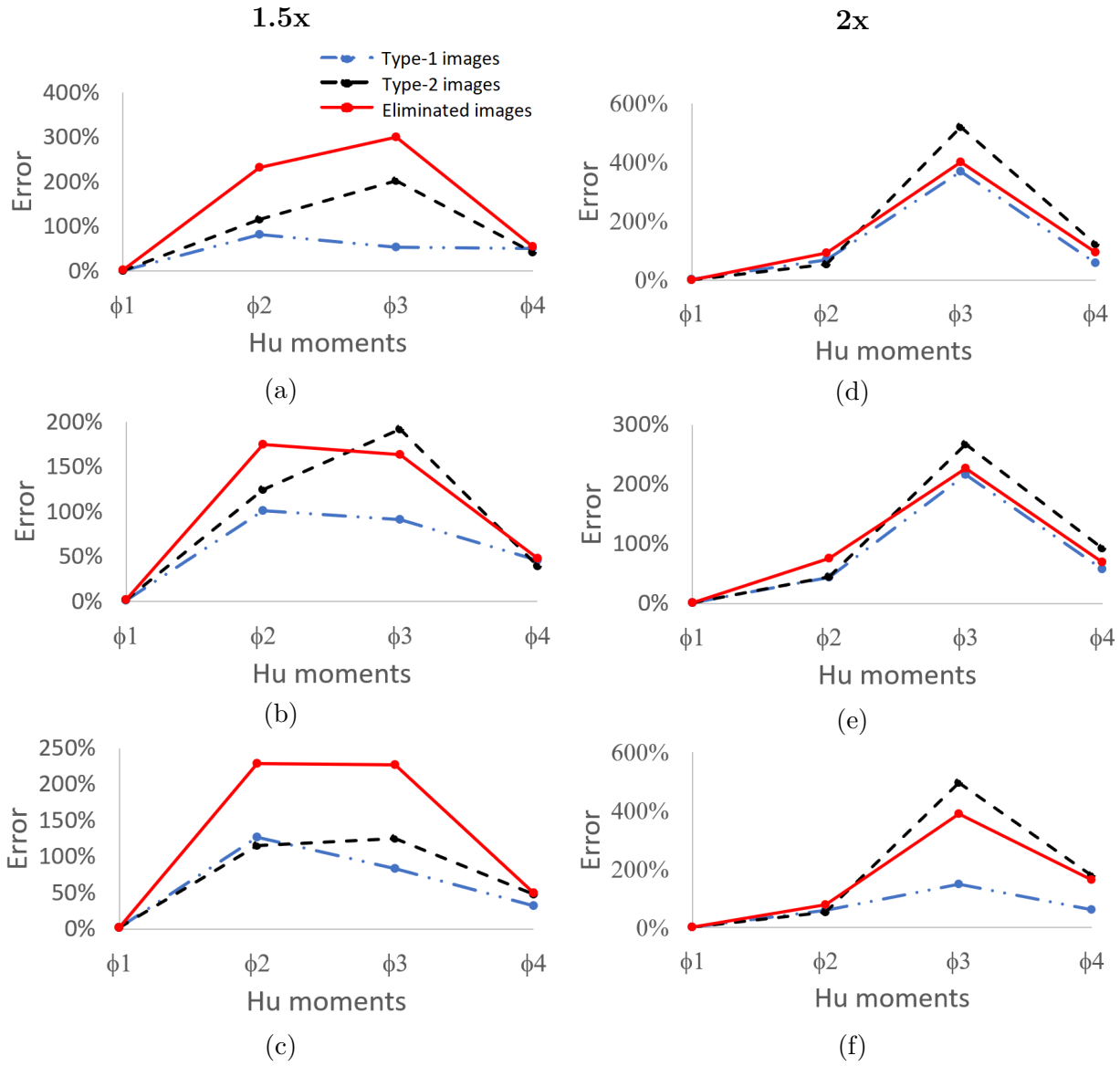

Figure 3.9: Average error percentage plots of the forged synthesized images reconstructed at a scale of 1.5× with (a) WS 5, (b) WS 7 and (c) WS 9 at a scale of 2× with (d) WS 5, (e) WS 7, and (f) WS 9 with various window sizes [56].

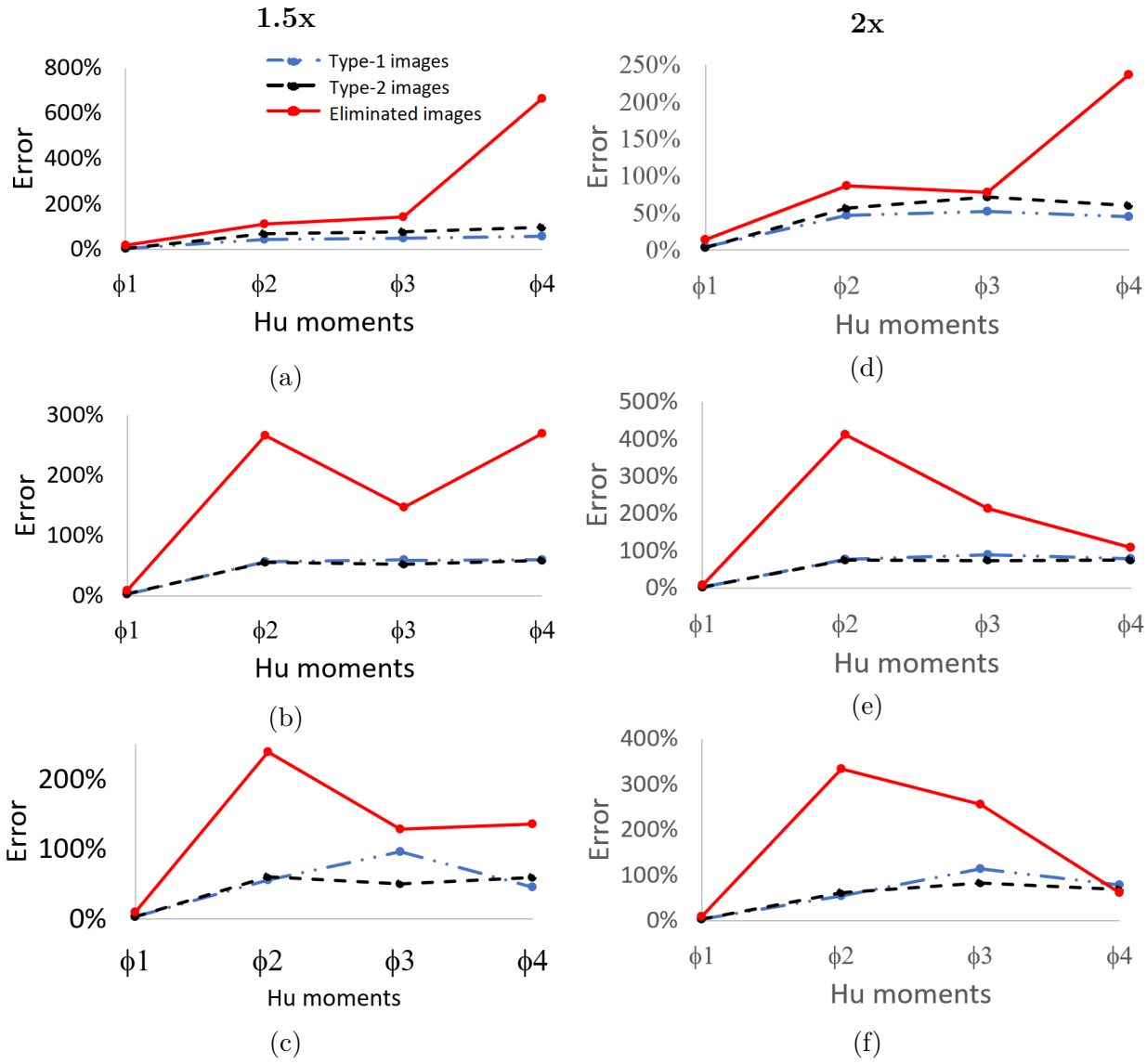

Figure 3.10: Average error percentage plots of the additively manufactured synthesized images reconstructed at a scale of 1.5× with (a) WS 5, (b) WS 7 and (c) WS 9 at a scale of 2× with (d) WS 5, (e) WS 7, and (f) WS 9 with various window sizes [56].

Table 3.2: Percentage acceptable images of hundred reconstructed samples for forged and additively manufactured microstructures after global level analysis [56]

Resolution	Window size	% acceptable (forged)	% acceptable (Add. Manuf.)
Same size	WS5	72%	83%
	WS7	63%	88.68%
	WS9	64.86%	85.42%
1.5x	WS5	63%	67%
	WS7	76%	59%
	WS9	64%	59%
2x	WS5	47%	75%
	WS7	57%	39%
	WS9	55%	44%

size for the given image.

The chosen acceptable images at the global level are again compared at the local level where each grain in the reconstructed image is separated as a single image and compared to the grains in the experimental image.

3.3.2 Local level

The grain size and shape are two important geometric parameters that form the layout of the microstructure. Hence, it is crucial to measure and compare these parameters in reconstructed images with the original. Since the global measures do not capture these, it is necessary to introduce a local-level analysis of the grains. The images filtered at the global level will be used at the local level for the grain-by-grain comparison. Every grain in each filtered synthetic image at the global level is separated into a single image of the same resolution.

The size and shape of the synthetic grains are to be compared with that of the grains present in the original image. The grain size is estimated by different methods for the forged and additively manufactured samples due to the difference in grain structures. For the forged

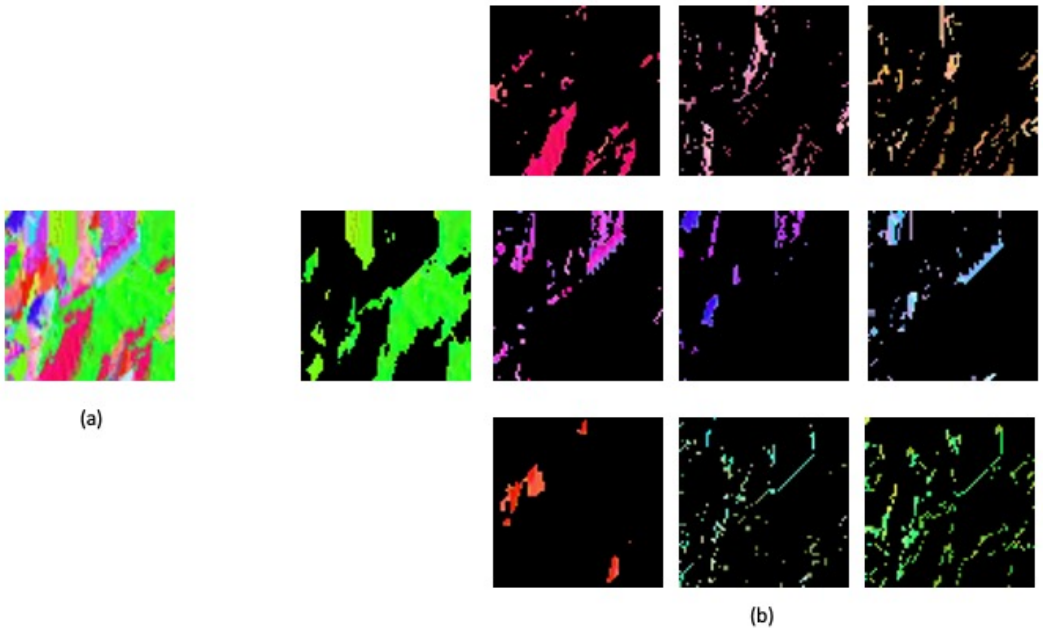

Figure 3.11: (a) A synthetic image reconstructed from Figure 3.1 (b) at a scale of 1.5 ×. (b) Clusters separated from the (a).

sample, the maximum distance between two pixels on the boundary of the grain is estimated to be the grain size. However, for the additively manufactured sample, the grain shapes are complex. Ten major colors in the image are identified first and then using the k-means clustering algorithm, the microstructure image is separated into ten images, where each of them contains a cluster of grains with one single color. An example of clusters is presented in Figure 3.11 for a synthetic image reconstructed at a scale of 1.5×. Here, each color represents the orientation of the grain. This approach can also be viewed as separating the grains from each other based on their orientations. The number of pixels in each of the ten images is calculated and an equivalent circle, which contains the same number of pixels, is generated. The radius of that circle is used as a parameter for studying the size of the grains in additively manufactured images.

The first Hu moment, ϕ_1, is decided to be the measure for the grain-by-grain shape compari-

son since it is the dominant moment among all seven Hu moments (Equation 2.5) magnitude-wise. ϕ_1 can capture both the shape and orientation of a grain. Unlike previous works [135], which were focused on comparing the invariant numbers to a particular shape, ϕ_1 can be treated as a single invariant number directly related to a specific grain. Among a set of grains, ϕ_1 can be used to represent the grains of the same shape or a range of ϕ_1 values can be defined to represent the grains of very similar shapes (grain family). This is possible with only ϕ_1 because it does not have a covariance term or any other higher-order complex moment. ϕ_1 is also the sum of the diagonal of the second-order normalized covariance matrix.

In other words, the summation of the normalized variance of the horizontal and vertical axes captures the shape of the grain. On the other hand, ϕ_1 cannot be used as a single local measure because it does contain information about the dimensions of the grains. Hence, grain size is also included at the local level comparison. Other Hu moments do not capture the grain shape as effectively as ϕ_1 since they have decreasing order of importance magnitude-wise. Mathematically, any type of moment without a covariance term can capture the grain shape. As the Hu moment is invariant to RST transformations, ϕ_1 would be the same number for the same grain shape irrespective of its location, rotation, or scale size.

The pixel intensities in the microstructure maps directly correspond to the orientation of the grain. When it comes to a small image with only one grain, ϕ_1 not only captures the shape but also the change in pixel intensity. Moreover, moment invariants capture the grain shapes explicitly and eliminate the need for defining a common geometry for studying the grain properties in a microstructure map.

Table 3.3 and Table 3.4 summarize the local-level grain-by-grain comparison of the same-size resolution cases. The average number of grains in all reconstructed cases is not the same as the original image. This shows that local-level analysis is also necessary. Additionally, the MRF reconstruction provides higher quality synthesized samples in general for the forged

microstructure, compared to the additively manufactured microstructure. This is because of the complex grain features of the additively manufactured material, which are still well characterized by the MRF and image moments; however, the forged samples are easier to quantify owing to their grain structure.

It was found at both local and global levels (Table 3.3 and Table 3.4) that the uncertainty is amplified more as the spatial resolution increases. At the global level, the Type-1 acceptable images of higher resolution cases are not as close to the original as the Type-1 of the same size resolution. Additionally, it is observed from Table 3.2 that the percentage of acceptable images decreases as the resolution increases. At the local level, the percentage change in the grain shape increases from the same size to the 2× in both forged and additively manufactured samples, as can be seen in Table 3.3 and Table 3.4. However, it is the opposite for the case of the forged sample at 2× resolution because of different filtering conditions. At the global level, the Type-1 acceptable images have the lowest average error in both 1.5× and 2×, as shown in Figures 3.8 - 3.10. The grains are repeated several times in higher resolution reconstruction due to uncertainty. Such repetitions are identified and their sizes and shapes are averaged at the local-level analysis. In the forged sample, the number of orientations in high-resolution samples is found to be different than the number of orientations in the same resolution. The best-performing window size is found to be changing with respect to each global and local level parameter. Therefore, the window size that performs the best for most global and local parameters is selected as the optimum window size.

3.3.3 Determination of optimum window size for reconstruction

The performance of reconstruction is significantly affected by the user-defined window size parameter. The optimum window sizes change for each type of microstructure image. There-

Table 3.3: Local level analysis of forged and additively manufactured samples of same size resolution [56]

Category	Window size	Average grain size	Average change in grain shape
Forged (Same size)	Original	12.55	-
	WS5	12	9.25%
	WS7	12.5	5.72%
	WS9	12.7	6.46%
Add. Manuf (Same size)	Original	16.06	-
	WS5	16.04	3.54%
	WS7	16.1	4.83%
	WS9	16.03	2.86%

fore, for the aforementioned 2D to 2D MRF reconstruction for the conventionally forged and additively manufactured microstructures, the optimum window size is determined based on multiple factors. The selection of the optimum window size is detailed in Table 3.5. From Table 3.5, it is clear that for the additively manufactured sample, the window size of 5 is optimum. Even though in the same size reconstruction, the window size of 7 produces more acceptable images, and the window size of 5 produces higher quality images at the local level. For the forged sample, both window size 5 and window size 7 can be selected as the optimum.

3.4 Verification methodology for 3D reconstructed microstructures

Based on the concept of moment invariants, a methodology is established for comparing the 2D experimental microstructures and 3D synthetic microstructures. For demonstration, the 3D microstructures reconstructed by Javaheri et al. [100, 101] are used. The computational reconstruction of two anisotropic microstructures manufactured by two different techniques is considered. The first one is the additively manufactured 316L stainless steel and the other

Table 3.4: Local level analysis of forged and additively manufactured sample under higher resolution reconstructions [56]

Forged Sample

Category	Window size	Average grain size	Average change in grain shape
1.5x	Original	15.7	-
	WS5	11.9	4.73%
	WS7	26	7.29%
	WS9	21	6.07%
2x	Original	16.23	-
	WS5	16.48	5.15%
	WS7	17.04	6.88%
	WS9	17.18	8.80%

Additively Manufactured Sample

Category	Window size	Average grain size	Average change in grain shape
1.5x	(original)	12.03	-
	WS5	11.89	7.44%
	WS7	11.9	8.74%
	WS9	11.8	11.95%
2x	(original)	15.91	-
	WS5	15.84	10.89%
	WS7	15.77	5.81%
	WS9	15.67	8.37%

Table 3.5: Best performing window size at each parameter [56]

Category	Resolution	Average ϕ_1 error	% Acceptable	Average grain size	Grain shape	Optimum WS
Forged	Same size	WS7	WS5	WS7	WS7	WS7
	1.5x	WS5	WS7	WS5	WS9	WS5
	2x	WS7	WS7	WS5	WS5	WS5&7
Add Manuf	Same size	WS5	WS7	WS5	WS9	WS5
	1.5x	WS7	WS5	WS5	WS5	WS5
	2x	WS5	WS5	WS5	WS9	WS5

one is a rolled aluminum-lithium (Al-Li) alloy sample. Experimental 2D anisotropic images of both samples are spatially reconstructed in 3D using the MRF algorithm by Javaheri et al [100, 101]. For more details about the reconstruction procedure, readers can refer to [100, 101]. The present work proposes to use normalized central moments (η) as formulated in Equation 2.4, as a universal measure to quantify grain shapes in different dimensions. Using the same metric (η), the distributions of the 2D and 3D grains are compared first. Then, a demonstration of the box whisker plot is used to compare the shapes and orientations of the 2D and 3D grains in detail.

First, each of the 2D and 3D grains separated from the microstructure is quantified by η in all three directions. The parameter η is suitable for quantifying grains because it is invariant to both shape and orientation. Additionally, η can serve as a universal parameter to measure the grain shapes of different dimensions. Since MRF is developed using a Gaussian-distributed weight parameter [28], the synthetic microstructure is also expected to produce a texture with a similar distribution. Evidently, the grains of both materials quantified using the lognormal transformation of η exhibit a normal distribution as presented in Figures 3.12 and 3.13. Hence, lognormal distributions of the grains are compared in Figure 3.12 and Figure 3.13 for rolled and additively manufactured samples, respectively. The logarithmic value of η is negative because the η values are less than 1 due to a large image area. The distribution curves in Figures 3.12 and 3.13 for both 2D and 3D grains demonstrates the normal distribution. For both samples (rolled and additively manufactured), as presented

in Figures 3.12 and 3.13, the distribution of synthetic 3D grains are matching with its corresponding counterpart directions in the 2D images. Each of the three distribution curves of the 3D microstructure (Figure 3.12 (b) and Figure 3.13 (b)) is compared to its counterpart in 2D distributions. The distribution curves are color-coded to compare the directions. The distribution lines of 2D orthogonal images have different shades to denote the three planes. For example, η_x of the 3D microstructure representing the normalized variations of all the 3D grains in the x direction is compared to the η_x of 2D grains obtained for the xy and xz planes i.e, the planes normal to the direction of xy plane (Long direction (L)) and xz plane (Long Transverse direction (LT)). The distributions of 2D η_x for both xz and xy planes and the distribution of 3D η_x are found to be comparable (Figures 3.12 and 3.13). A similar comparison can be made for the η_y and η_z distributions (Figures 3.12 and 3.13). Therefore, all the grains in the 2D and 3D microstructures are varying proportionally in the three directions.

Next, the shape and orientation of 2D and 3D grains are compared using the same metric (η_x, η_y, and η_z). A box whisker plot using the $|\ln \eta|$ values is presented in Figure 3.14 and Figure 3.15 for the rolled and additively manufactured microstructure samples, respectively. The normalized variances of both 2D and 3D grains quantified by the invariant η are compared in all three directions. For 2D grains, the normalized variance in a direction is spread out in two planes. That is, the net η_x value of 2D grain is resolved into the planes normal to LT (xz-plane) and L (xy-plane) directions. Therefore, three box whisker plots are created for each sample to individually compare the data. For example, as illustrated in Figure 3.14 and Figure 3.15, the planes normal to the ST (Short Transverse) direction (yz-plane) contain the information about the spread and skewness of all the 2D and 3D grains in both y and z directions. The η is the same measure quantifying both shape and orientation (represented by pixel intensities) of 2D and 3D grains making it advantageous over other

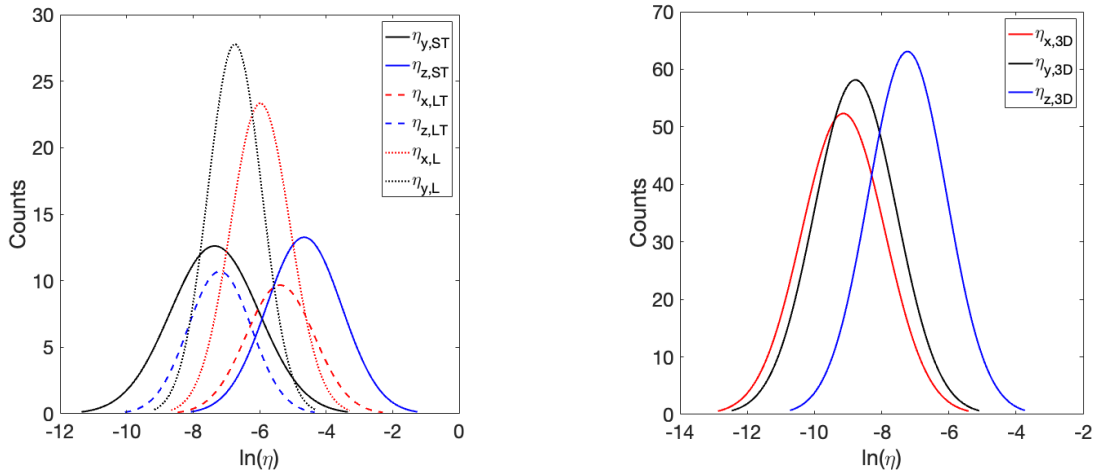

(a) 2D orthogonal images (b) 3D microstructure

Figure 3.12: Distributions of 2D and 3D microstructures of rolled Al-Li sample [60].

moments. The box whisker plot provides an analysis of the grain shape comparison for each plane individually, which makes it preferable for the case of anisotropic microstructures.

First, for the rolled sample, the spread of normalized variance in the z direction of 2D grains in the LT plane (z_{LT}) is found to be completely within the range of the normalized variance of 3D grains in the z direction (z_{3D}). Both $\eta_{z_{LT}}$ and $\eta_{z,3D}$ have no skewness, thus agreeing with a normal distribution. The long transverse direction (y) also has the 2D and 3D grains varying commensurate to each other. This can be found in the plots of $\eta_{y,ST}$ vs $\eta_{y,3D}$ in the ST plane (Figure 3.14) and $\eta_{y,L}$ vs $\eta_{y,3D}$ in the L plane (Figure 3.15). The slight mismatch between the η_y values of 2D and 3D grains in both the ST and L planes for the aforementioned comparison can be attributed to the large volume of the 3D grains. However, when it comes to the normalized variance of 2D and 3D grains in the x direction, the spread of 3D grains is translated slightly away from the range of 2D grains both in the LT and L planes. The 2D grains varying in the x direction of the LT and L planes and the z direction of the ST plane are found to be slightly skewed to the left. Their counterpart directions in the 3D microstructure (η_z and η_x), although not visible in Figure 3.14, do produce a slightly

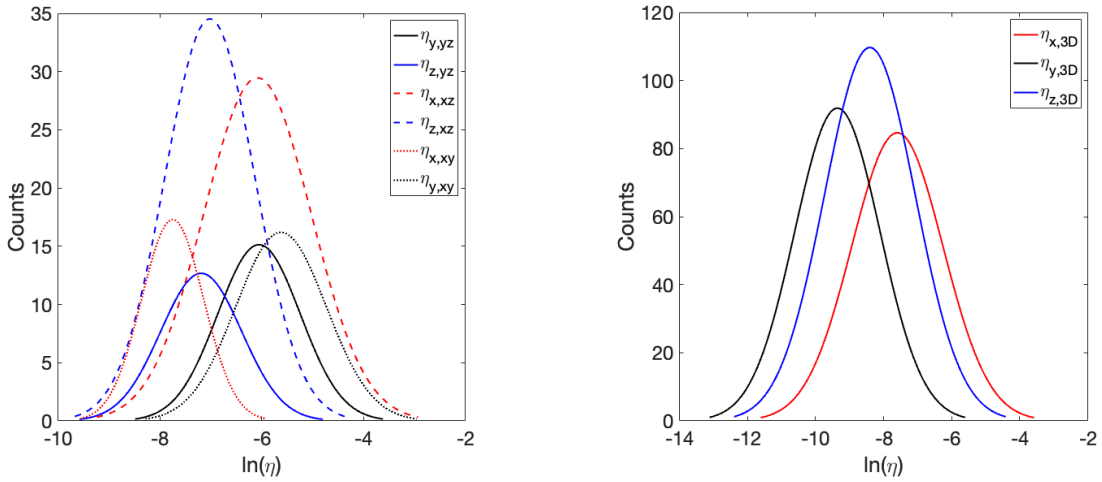

(a) 2D orthogonal images (b) 3D microstructure

Figure 3.13: Distributions of 2D and 3D microstructures of additively manufactured 316L stainless steel sample [60].

left-skewed distribution.

Next, for the additively-manufactured sample, the small boxes for 2D cases in box whisker plots of Figure 3.15 imply that the shapes of 2D grains are similar to each other. When compared to 3D, the 2D grains are varying proportionately to the 3D grains in both x and z directions. The spread and skewness of η_x in xz and xy planes and η_z in yz and xz planes for both 2D and 3D grains are found to be analogous. On the other hand, the y direction has a slight anomaly indicating that the reconstruction has provided more similar microstructural features to the experimental data in x and z directions. The outliers in Figure 3.14 and Figure 3.15 simply represent the corner grains and grains with unusual shapes compared to the other 2D and 3D grains. An example of an outlier grain is presented in Figure 3.16.

The synthetic microstructures generated by the MRF algorithm demonstrate features that are statistically equivalent to the input (experimental) microstructure. Therefore, it becomes crucial to analyze how much the shape and orientation of synthetic 3D grains are varying with respect to the 2D grains. The statistical parameters from the distribution data (Figure

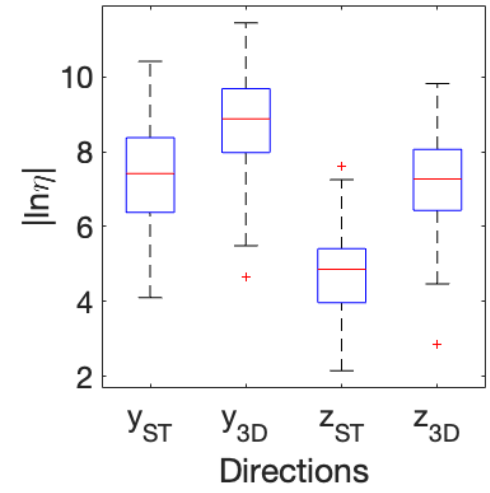

(a) ST plane

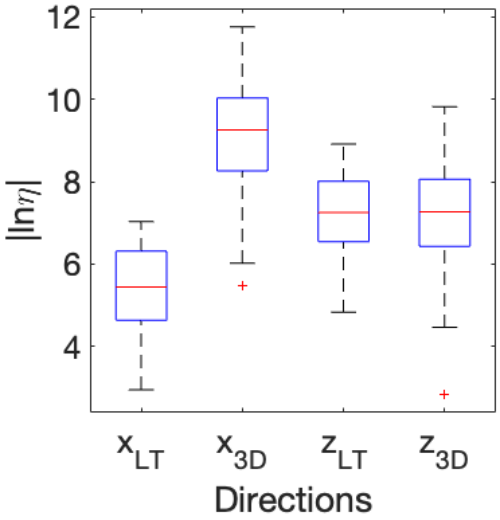

(b) LT plane

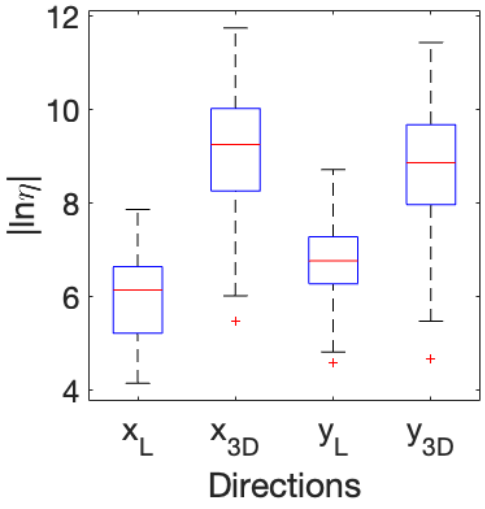

(c) ST plane

Figure 3.14: Box whisker plot of 2D and 3D microstructures of rolled samples [60].

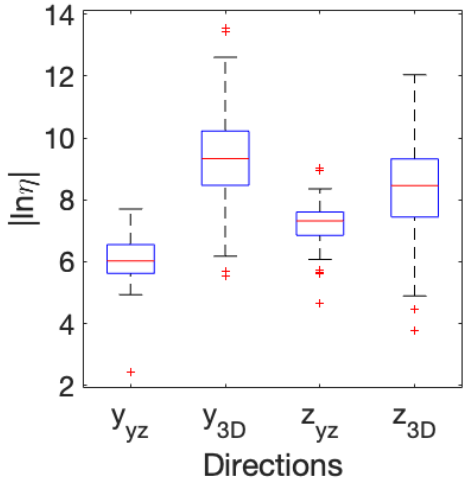

(a) X plane

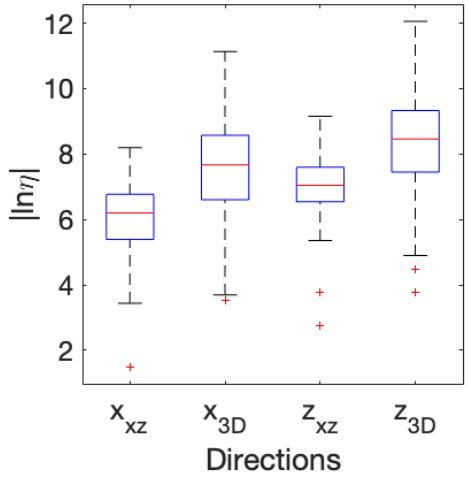

(b) Y plane

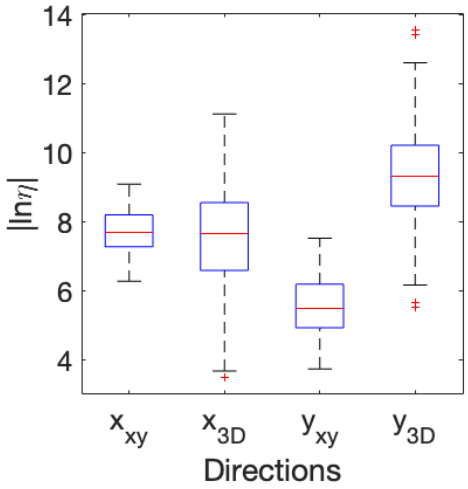

(c) Z plane

Figure 3.15: Box whisker plot of 2D and 3D microstructures of additively manufactured sample [60].

Figure 3.16: An outlier grain from the experimental z_{xz} data of Figure 3.15. Here, the orientations of all pixels are very similar. As a result, the clustering algorithm considered them to be the same grain. [60]

3.12 and Figure 3.13) of both materials are determined and listed in Table 3.6 to understand the anisotropic nature of the reconstructed microstructure. The parameters describing 3D grains are compared to 2D grains for each direction. The notation for the 2D grain directions in Table 3.6 is as follows: $\text{direction}_{\text{plane}}$. The mean value can be used to find how much the 3D grains are offset from the 2D grains. The standard deviation and variance measure how much the 3D grains are varying from the distributions of the 2D grains in a particular direction. For example, it is worth noting that for the rolled sample, the mean of 3D grains offsets more from the mean of 2D grains in the x direction compared to the other two. For the additively manufactured sample, the mean of 3D grains offsets more in the y direction than the other two, which is analogous to the observation made from the box whisker plot of the additively manufactured sample. Furthermore, in the case of the rolled sample, it is observed that the variance of 3D grains in the z direction (L) is close to the variance of the 2D grains in the z direction of the yz plane (ST) than the z direction of the xz plane (LT). From this observation, it can be concluded that the reconstruction works better on the yz plane rather than the xz plane for the rolled sample. The mean and variance values demonstrate that the algorithm produces 3D features that are statistically more similar to the experimental orthogonal images in some directions than others. These statistics can

be better characterized with larger databases of reconstructed samples in the future. The generation of statistical data can also enable to study the propagation of the algorithmic uncertainty of the MRF method on synthetic anisotropic microstructures.

Table 3.6: Statistical parameters of 2D and 3D grains quantified by η in all the three directions [60].

Method	Parameter	X			Y			Z		
		3D	X_{xz}	X_{xy}	3D	Y_{yz}	Y_{xy}	3D	Z_{yz}	Z_{xz}
Rolled	Mean	9.13848	5.380784	5.976988	8.779185	7.350776	6.743291	7.231071	4.660436	7.197765
	Standard deviation	1.242754	1.028651	0.89541	1.228236	1.334567	0.808697	1.164793	1.13509	0.951241
	Variance	1.544438	1.058122	0.80176	1.508564	1.78107	0.65399	1.356743	1.288429	0.90486
Additively manufactured	Mean	7.595243	6.080227	7.747056	9.357121	6.049683	5.61661	8.402375	7.185405	7.015467
	Standard deviation	1.339053	1.051975	0.608671	1.251892	0.811646	0.888308	1.330783	0.795874	0.884797
	Variance	1.793062	1.106652	0.370481	1.567235	0.658770	0.789092	1.770984	0.633415	0.782866

Chapter 4

UNCERTAINTY QUANTIFICATION FOR MICROSTRUCTURE TOPOLOGY

An outcome of a deterministic model design may not be reliable without considering the uncertainties. Therefore, to achieve robust results, design under uncertainty has been heeded as an important research topic in the field of material science and the aerospace industry. [26, 138]. Experiments and simulations often cause measurement and modeling/parametric uncertainties, respectively. Because of these uncertainties, a notable deviation in the performance of aircraft components is observed [139]. Therefore, uncertainty is taken into consideration during the material design for aircraft turbine components [140, 141]. Aircraft materials are required to satisfy multiple selection criteria involving mechanical and chemical properties [1]. Hence, designing materials for aircraft components requires performing rigorous testing to determine the homogenized material properties. The macro-scale properties of materials such as Young's modulus or the yield strength are directly affected by the crystallographic nature of the material at the micro-level. Therefore, the microstructure topology of the material is studied through EBSD experimental techniques. This work aims to quantify the effects of the uncertainty of microstructure topology and its propagation on homogenized material properties. While there are previous studies in the literature that

modeled the effects of uncertainty of the microstructural texture on the homogenized properties [142, 143, 144], the effects of the uncertainty on microstructure topology (i.e., the grain shapes) have not been considered before in the literature, to the best of the author's knowledge.

Many state-of-the-art models have been developed in the past for Uncertainty Quantification (UQ) based on numerical and analytical techniques [42, 115, 142, 145, 146, 147, 148] while the numerical UQ algorithms pose some challenges. For instance, the Monte Carlo Simulation (MCS) is a computationally expensive method that can be numerically intractable for quantifying the uncertainty of large 3D microstructure samples [147]. On the other hand, a Bayesian approach-based UQ model [142] requires a good knowledge in the selection of a prior distribution and thus is not suitable for representing the randomness arising from microstructure reconstruction [147]. Models based on advanced techniques such as Deep Neural Networks have also been developed [149] for UQ while their large data requirements pose challenges. As an alternative strategy, surrogate models have been developed using probabilistic and non-probabilistic theories [146]. However, the present study explores the effects of uncertainty on grain shapes and resulting homogenized properties of microstructures by introducing new moment invariant-based statistical measures.

In this work, the uncertainties arising from the EBSD experimental technique and the reconstruction algorithm are studied and quantified through the concept of moment invariants as explained in Section 2.3 [57, 58, 59]. First, the source of the uncertainties is identified. EBSD technique has a long sample preparation process such as mechanical polishing, which can introduce uncertainty on the RGB pixel intensity values representing the microstructural orientation information. Mechanical polishing is a method used to create a smooth sample surface for the EBSD device to map the crystallographic orientation topology with Orientation Image Mapping (OIM) [47]. Although polishing is not performed for this work, a brief

explanation of the procedure is provided for understanding the causes of experimental uncertainty. The mechanical polishing procedure starts with coarse grinding the sample surface to fine grinding on different standardized abrasive papers. Then, the scratchings on the sample surface that has resulted due to grinding is removed by using slurry solutions. The final result will be a mirror-like flat surface. Thus, the sample surface has to undergo a series of long and tedious procedures because the phosphorous screen in the EBSD device requires a flat and clean polished surface to obtain the crystallographic orientation. However, often the scratching and deposits of slurry solutions are left over on the sample surface which affects the information obtained by the EBSD device. This experimental error is reflected on the microstructure image as incorrect pixel intensity values while scanning the sample surface with OIM and thus resulting in aleatoric uncertainty. Therefore, during reconstruction, the erroneous pixel intensity values obtained experimentally are propagated on the synthesized images.

Another source of uncertainty is the stochastic nature of the MRF algorithm. The presence of randomness in the reconstruction algorithm introduces uncertainties to the microstructural features that lead to variations in homogenized properties. The use of probabilities leads to randomness in the reconstructed microstructural features. In other words, each synthetic microstructure would look slightly different than one another if the MRF algorithm is run multiple times using the same input data. This randomness in the microstructural features as a result of the model uncertainty would lead to variations in the material properties. This type of uncertainty is called epistemic uncertainty.

Proof of both kinds of uncertainty can be observed in the following demonstration. The experimental image of Ti-7Al presented in Figure 3.1 (a) is used to reconstruct three synthetic microstructures spatially at a scale of 1.5× and 2× with window sizes ranging from 5 to 9. Examples of some of the synthesized microstructures are presented in Figure 4.1. Each of the

synthesized images is modeled using PRISMS-Plasticity [150, 151] (details explained in Appendix A) and uniaxial tension simulations are performed on the modeled microstructures to determine the material properties. The resulting stress-strain curves are presented in Figure 4.2. Using the k-means clustering algorithm, each microstructure image is separated into 15 clusters as presented in Figure 4.3. Each cluster has a collection of grains that has the same orientation. Then, every single grain from all the clusters is further isolated and quantified by ω_1 and ω_2 which are introduced by [135]. ω is a dimensionless moment invariant to different shape transformations [135]. Since this demonstration has been completed prior to the aforementioned microstructure characterization and verification procedures, PEM is not used for grain shape quantification. More details are available in [152]. It can be observed in Table 4.1 and Table 4.2 that when compared to the average ω values of the grains in the experimental image (7.2277, 98.7023), the synthesized images generated grains that demonstrate ω values ranging as: $\omega_1 = [6.5291, 7.6292]$ and $\omega_2 = [91.1067, 101.3621]$. These ranges lead to the variations of **-9.67% to +5.56% for** ω_1 **and -7.7% to +2.7% for** ω_2 compared to the experimental data. The uncertainty observed in the microstructure also propagates on the material properties. Compared to the experimental image that demonstrates Young's modulus (E) of 133.7456 GPa and yield strength (σ_y) of 726.2467 MPa according to the crystal plasticity simulations, a range of material properties is determined for the synthesized images with different window sizes. The variations in the properties of the synthesized samples are determined to **range from -0.48% to +3.59% for** E **and from -4.21% to +2.5% for** σ_y compared to the values obtained with the crystal plasticity simulation of the experimental microstructure. Evidently, the material properties calculated through Crystal plasticity (CP) simulations are affected by the changes in the grain topology. Therefore, it is crucial to develop statistical parameters that would quantify the uncertainty propagating on the synthesized microstructures.

Table 4.1: ODF and shape moment invariant values for 1.5x reconstructed images [57]

	Window size 5		Window size 7		Window size 9	
	ω_1	ω_2	ω_1	ω_2	ω_1	ω_2
Image 1	7.6292	101.3621	7.2539	97.3060	7.1019	94.7028
Image 2	7.0504	94.6042	6.5010	97.8937	7.1474	94.3335
Image 3	7.2160	94.9669	7.1773	93.3669	7.0567	97.0908

Table 4.2: ODF and shape moment invariant values for 2x reconstructed images [57]

	Window size 5		Window size 7		Window size 9	
	ω_1	ω_2	ω_1	ω_2	ω_1	ω_2
Image 1	6.6630	91.5392	6.8309	90.6279	6.5291	91.1067
Image 2	6.6869	90.7083	6.7574	92.0010	6.8494	93.3216
Image 3	6.7238	90.5626	6.7342	92.3165	6.8224	93.8803

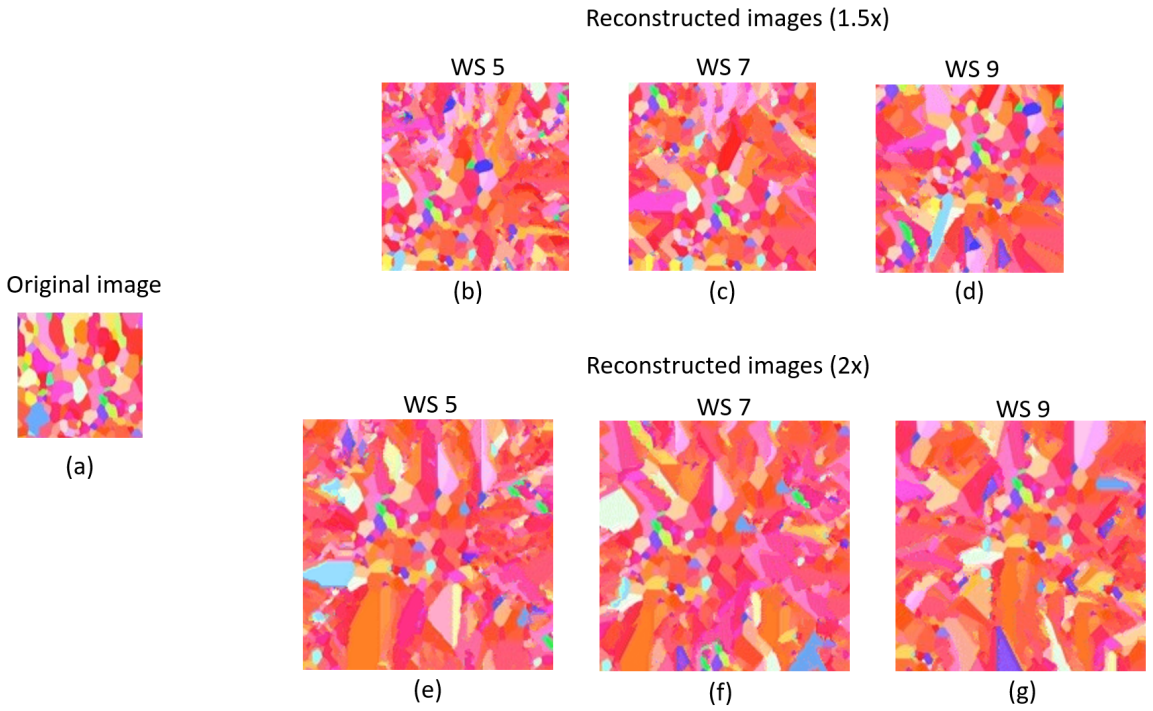

Figure 4.1: (a) Experimental image of Ti-7Al with resolution 100×100, (b) $1.5\times$ reconstructed image (150×150) with WS5, (c) $1.5\times$ reconstructed image (150×150) with WS7, (d) $1.5\times$ reconstructed image (150×150) with WS9, (e) $2\times$ reconstructed image (200×200) with WS5, (f) $2\times$ reconstructed image (200×200) with WS7; and (g) $2\times$ reconstructed image (200×200) with WS9 [57].

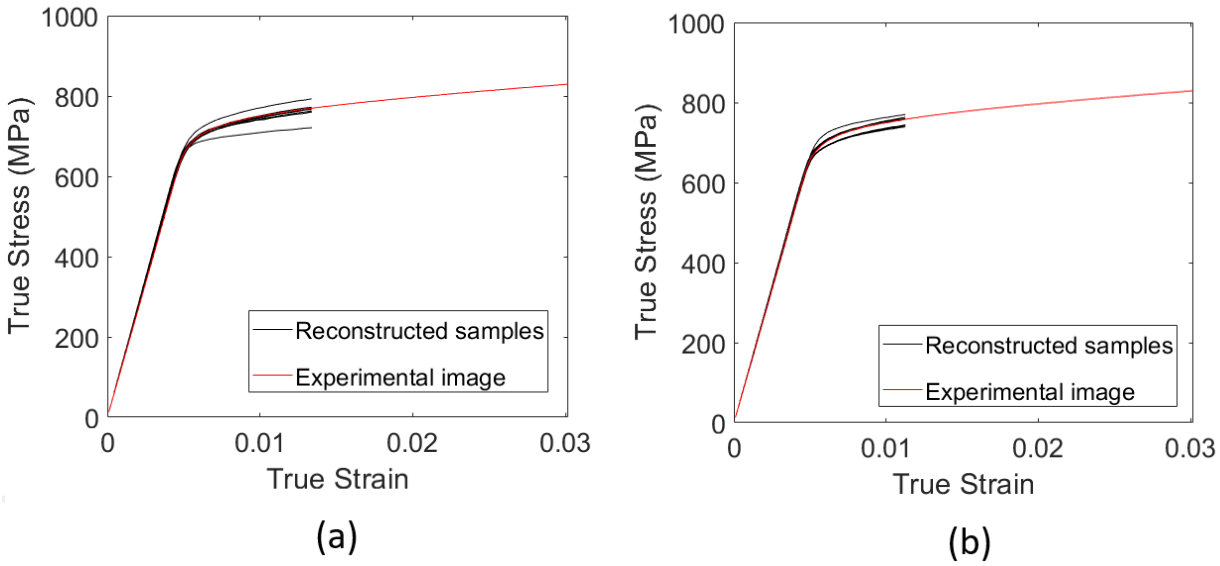

(a) 1.5× reconstructed images

(b) 2× reconstructed images

Figure 4.2: Stress-strain curves of reconstructed images compared to the experimental curve up to 3% strain [57].

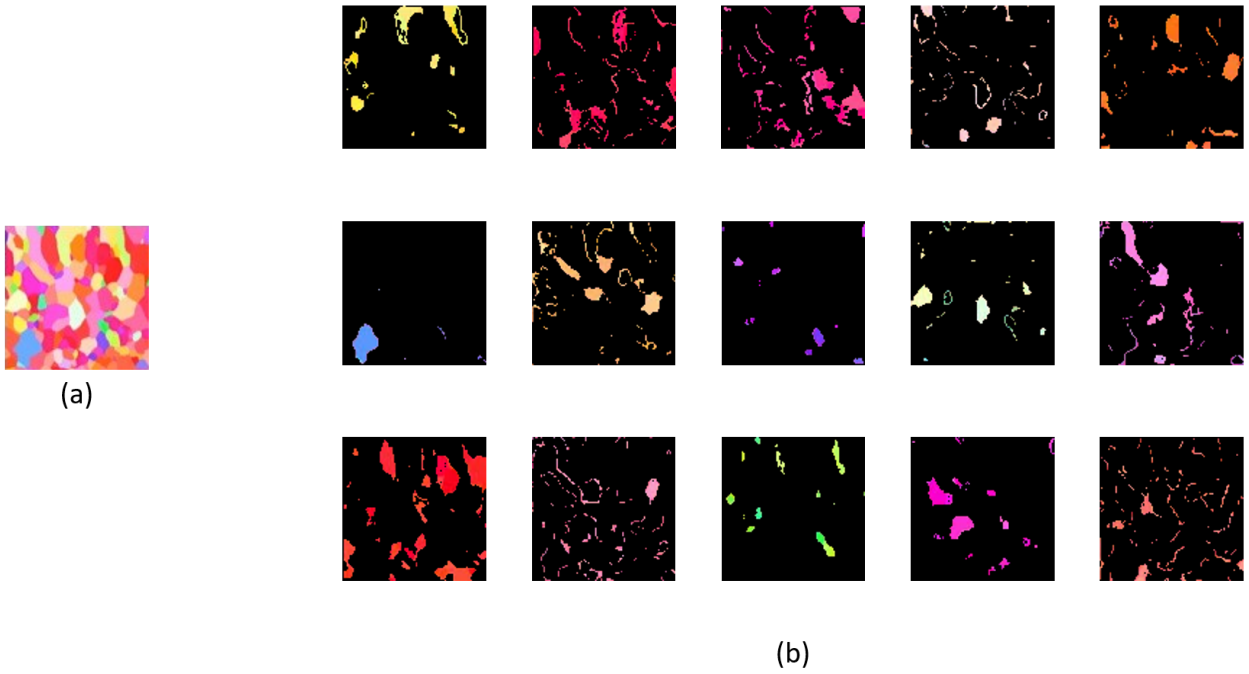

Figure 4.3: (a) Original experimental image, (b) Separation of 15 clusters with each cluster indicating a unique microstructural orientation [57].

This chapter is organized as follows: Section 4.1 presents the new statistical parameters developed based on the moment invariants to quantify the epistemic and aleatoric uncertainties in the microstructural topology. Section 4.2 demonstrates the ability of shape moment invariants as a microstructure descriptor when predicting the material properties as a function of microstructural topology.

4.1 Moment invariant based statistical parameters for UQ

To study the uncertainty propagation on the synthesized material and resultant the material properties, microstructure images were reconstructed without any aforementioned filters discussed in Section 3.1. Two different Ti-7Al microstructure images (Figure 4.4 (a) and Figure 4.4 (b)) are used to predict the larger scale evolution of microstructures. Using the MRF method, a total of 1000 images are reconstructed for each image at a scale of 1.5×. Figure 4.4 (c-d) shows one example selected among 1000 synthesized images. The probability of finding the optimum pixel intensity value for the synthetic structure is achieved through the Gaussian distributed weight parameter of the MRF algorithm [28].

The synthesized microstructure texture quantified by the PEM has also yielded a probability distribution similar to the Gaussian distribution (Figure 4.5). The advantage of MRF's resemblance to the Gaussian distribution feature is taken into account for modeling the uncertainty of material properties. The absolute PEMs are calculated for the whole image and their values are plotted (Figure 4.6) in a natural logarithmic scale. Figure 4.6 shows the $\ln|\lambda|$ values of both experimental and synthetic microstructures. Here, the synthetic data (represented with λ_s) forms a cluster around the experimental eigenvalue (λ_e). The

Table 4.3: Parameters to statistically validate 2D images [58]

	R	d_λ	ζ	ρ_a	ρ_p
Forged	0.1187	0.0159	0.0336	2.3579	1.3828
Additively manufactured	0.4348	0.0981	0.1186	5.8036	2.1048

eigenvalues are calculated using Equation 2.8 for any particular image. While λ_e is constant for a single experimental image, λ_s varies within λ_{s1}, λ_{s2},...,λ_{sN} for the synthetic images ranging from 1 to N, where N represents the total number of reconstructed samples. The mean of the eigenvalues for all the synthesized images is also plotted ($\bar{\lambda_s}$) in Figure 4.6 and it is found to be in close proximity to the experimental data points λ_e for both cases. However, Figure 4.6 is the graphical representation to validate the reconstruction. To study the UQ problem for the reconstructed microstructures, five different parameters are derived from the PEM map (Figure 4.6).

Hence, in the present work, the statistical parameters for UQ are defined using the concept of moment invariants to develop an explicit and computationally efficient model. The developed statistical parameters can also be applied to the UQ of any reconstruction technique making this a universal approach. However, a special focus is given to the MRF algorithm. This is because the MRF method generates multiple unique microstructures using the same experimental image. Next, uncertainty propagated on the reconstructed microstructures and material properties are determined using crystal plasticity simulations.

The following five parameters are derived from the PEM-based map illustrated in Figure 4.6 to quantify epistemic and aleatoric uncertainty.

The first parameter is the *radius* (R) of the enclosed circle that completely covers the cluster of all synthesized eigenvalue points where the center of the circle is defined as the eigenvalue of the experimental image (λ_e). The radius parameter measures the maximum possible extent of the data spread in the PEM-based map with respect to the experimental value.

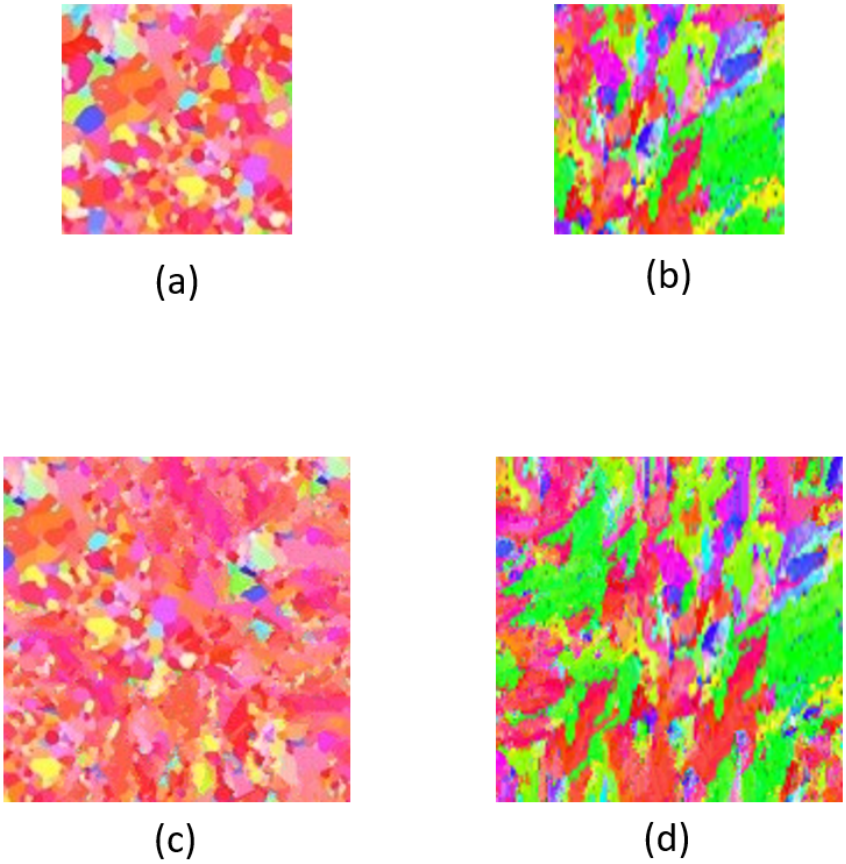

Figure 4.4: Original experimental images of (a) Forged Ti-7Al of size 100x100, (b) Additively manufactured material of size 93x93, (c) Reconstructed example of the forged Ti-7Al with size of 150x150, and (d) Reconstructed example of the additively manufactured material with size of 140x140 [58].

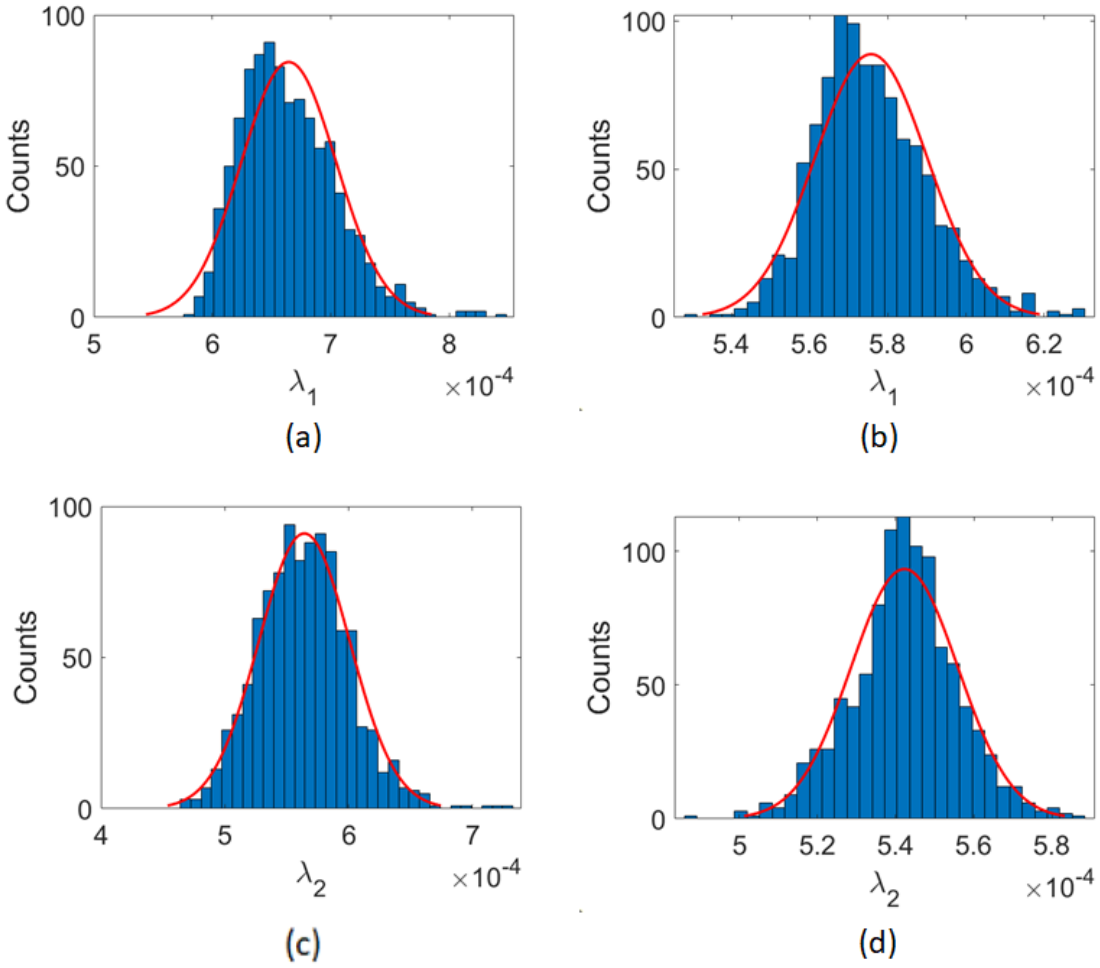

Figure 4.5: (a)-(b) Standard normal distributions of λ_1 for additively manufactured Ti-7Al microstructure and forged Ti-7Al microstructure (c)-(d) Standard normal distributions of λ_2 for additively manufactured Ti-7Al microstructure and forged Ti-7Al microstructure [58].

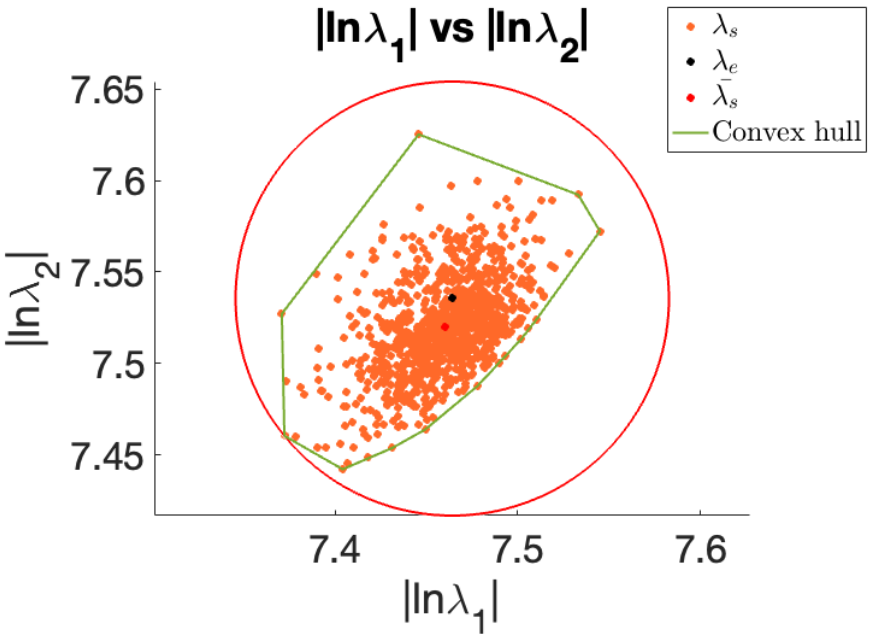

(a) Conventionally forged

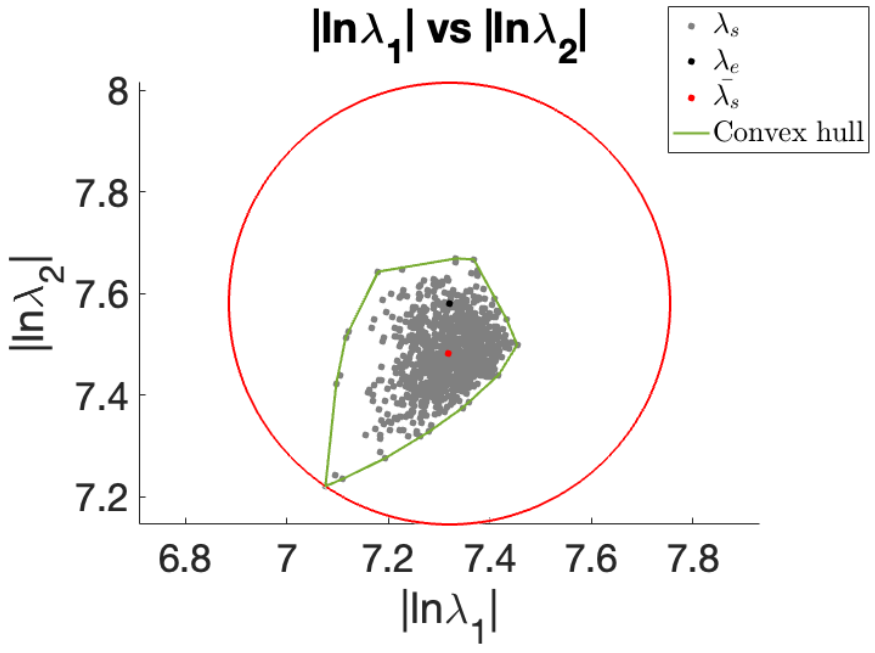

(b) Additively manufactured

Figure 4.6: PEM-based map for Ti-7Al microstructure [58]

The second parameter is the *average distance* ($d_{\bar{\lambda}}$), which measures the distance between the average eigenvalue of all synthesized images ($\bar{\lambda_s}$) and the eigenvalue of the experimental image (λ_e). $d_{\bar{\lambda}}$ helps with evaluating the average of the data spread for a given reconstruction procedure. This is because the PEM of an image as a whole predominantly depends on the image size and the pixel area, which is the sum of all pixel intensities of all three color channels (RGB). However, the ratio of the radius over this average distance can distinguish different images vividly.

$$d_{\bar{\lambda}} = ||\bar{\lambda_s} - \lambda_e|| \tag{4.1}$$

The next parameter, ζ, is the mean of the distances between all the synthesized points with respect to the experimental eigenvalue. ζ is defined to demonstrate the statistical similarity of 2D and 3D reconstructed microstructures to the experimental data (where N stands for the total number of synthesized samples).

$$\zeta = \frac{\sum(||\lambda_s - \lambda_e||)}{N} \tag{4.2}$$

The last two parameters, ρ_a and ρ_p, are the ratios of the area and perimeter of the enclosed circle to that of a convex hull. The circle covers the maximum area enclosed by the spread of all λ_s points. On the other hand, the convex hull is the closure of the smallest area covered by the spread of all λ_s points.

$$\rho_a = \frac{\text{Area of the enclosed circle}}{\text{Area of the convex hull}} \tag{4.3}$$

$$\rho_p = \frac{\text{Perimeter of the enclosed circle}}{\text{Perimeter of the convex hull}} \tag{4.4}$$

One can use these five parameters to investigate the uncertainty of the reconstructed microstructures. In this study, the additively manufactured microstructure images are expected to demonstrate higher variations in microstructural features due to their complex grain shapes [153]. This hypothesis is also verified using the radius parameter defined above. However, the high ρ_a value computed for the additively manufactured microstructures reveals that the level of uncertainty associated with each reconstruction is different (Table 4.3). The illustrated values in Table 4.3 calculations show that the synthesized image may differ significantly from the experimental image due to epistemic and aleatoric uncertainty.

Furthermore, the same set of five statistical parameters for quantifying the uncertainty of 2D grain topology is extended to the 3D microstructures reconstructed with the MRF algorithm developed by Javaheri et al [100]. Their MRF technique applies a voxel-by-voxel filling approach based on matching the neighbor window of a voxel with the 2D image locally in addition to using a global optimization approach [100]. Therefore, it is important to include each pixel and voxel value while comparing the 2D and 3D microstructures to understand if the reconstructed data is statistically equivalent to the input 2D data. The 2D experimental EBSD image of Ti-7Al manufactured by conventional forging (Figure 3.1 (a)) is used for 3D reconstruction. More details on the reconstructed 3D synthetic microstructure are available in [58]. While comparing 2D and 3D samples is more challenging, it is still possible by using PEM. The eigenvalues for all the plane sections normal to X, Y, and Z directions are calculated and plotted in the PEM map (Figure 4.7 (a-c)) [58]. The data points of the 3D reconstructed microstructure are found to be located within a range around the original eigenvalues of the input 2D image in Figure 4.7. This proves that the reconstructed sample is statistically similar to the input data which can also be observed in Table 4.4.

The histogram of PEM for 1000 synthesized microstructures demonstrates a normal distribution (Figure 4.5) as MRF uses a Gaussian distributed weight parameter to determine the

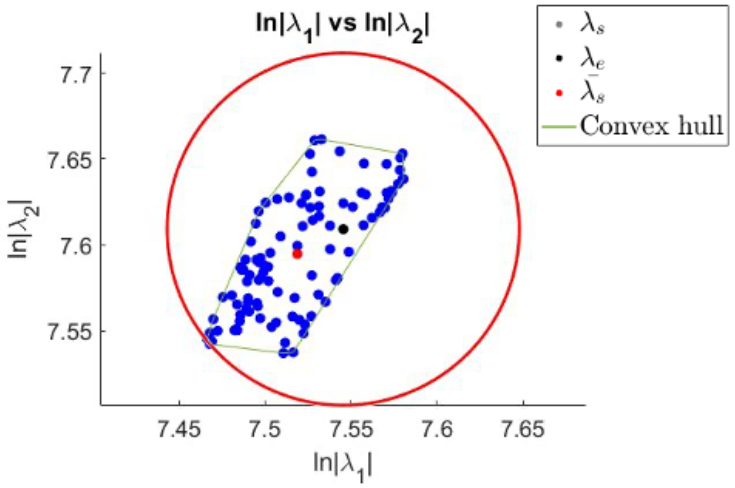

(a) X Section

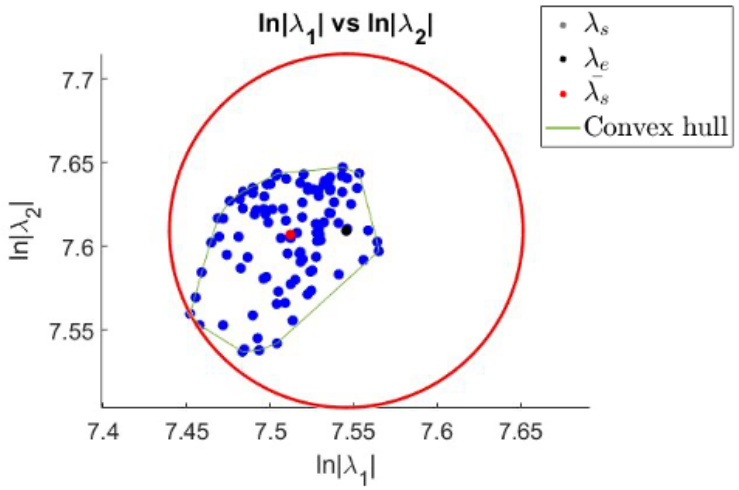

(b) Y Section

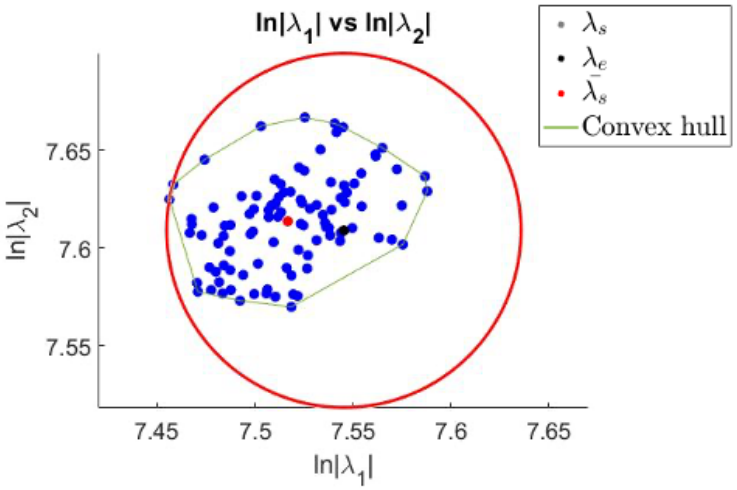

(c) Z Section

Figure 4.7: PEM-based map for X, Y, and Z sections of 3D forged Ti-7Al microstructure [58]

Table 4.4: Developed Metrics for Statistical Quantification of 3D Microstructure Samples [58]

Forged Sample	X	Y	Z
R	0.1024	0.1057	0.0905
d_λ	0.0303	0.0335	0.0291
ζ	0.0509	0.0453	0.0428
ρ_a	4.3381	4.2662	2.8814
ρ_p	1.7343	1.9250	1.6044

probability information. This result is significant since the Gaussian-distributed features can be used to model uncertainty propagation (on material properties) using Gaussian Process Regression (GPR).

4.2 Surrogate model of homogenized material properties

A Gaussian Process is a collection of random variables that agree with a joint Gaussian probability function [154]. It involves a Bayesian approach where the probability distribution prediction is updated at each iteration until it is converged and assigned as the final posterior distribution. Gaussian Process Regression (GPR) is a stochastic process that has applications in optimization [155], supervised machine learning [156], UQ [157], and multi-fidelity modeling [19]. In the present work, GPR is used to investigate the effects of microstructural uncertainties by developing a surrogate model representation with the Kriging method. A brief overview of this work is presented in Figure 4.8. The training data is obtained by the CP simulations that are performed for the synthetic microstructures with PRISMS-Plasticity [150, 151]. For CP simulations, the microstructure images are modeled as a single layer made of N^2 voxels, where N represents the image dimensions. A 10×10 mesh strategy is used on the model to save computational time. The number of voxels is

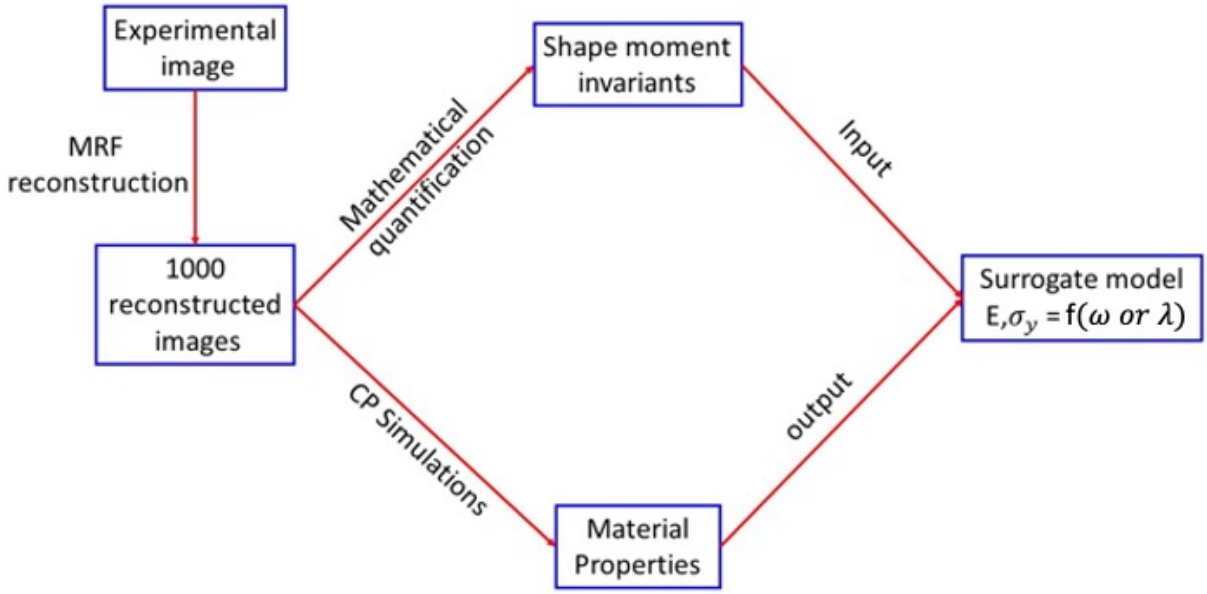

Figure 4.8: Flowchart explaining the process implemented for developing the surrogate model [59]

equal to the number of pixels in the image. This CP model is used to generate training data of microstructural features quantified by shape moment invariants and corresponding homogenized properties in a uniaxial tensile test.

The kriging model is widely used in the field of Geology [158]. It consists of a regression of sample data points followed by a prediction of future outcomes through a correlation function and has been explored in the past for modeling microstructures [30, 159, 160]. The possibility of using different combinations of regression models along with the correlation function makes the kriging method preferable for achieving the objective of predicting material properties as a function of microstructural topology. With the use of the GPR method, the variance of the outcomes is automatically predicted in addition to the mean value estimations. Therefore, it leads to an efficient approach to studying the uncertainty propagation on outputs. In particular, the kriging method is utilized using the DACE toolbox [161] to build the surrogate

model of the complex and non-explicit relationship between the shape moment invariants and material properties (Young's modulus and yield strength). The hyper-parameters of the kriging method are found by solving an optimization problem that aims to minimize the mean squared error computed for all test points by following the approach presented by Sacks et. al [162]. Here, a polynomial regression of zeroth order is implemented followed by an exponential correlation function, as defined next.

$$corr(X_i, X_j) = \prod e^{-\theta_{jk}|X_{ik}, X_{jk}|} \tag{4.5}$$

where θ is the hyper-parameter of the correlation function obtained with a minimum error strategy between test points (X_{ik}) and predictions (X_{jk}) (Equation 4.5).

To train the surrogate model, the results from Section 4.1 are used. To predict the material properties two types of surrogate models are developed. One is for conventionally forged microstructures (Model-1) and the other is for additively manufactured microstructures (Model-2). Both models use different kinds of shape moment invariants to understand their ability to predict the homogenized material properties. Model-1 uses ω introduced by [135] to quantify the microstructural topology and Model-2 uses λ (PEM) developed in this work. Out of the 1000 reconstructed images of the Ti-7Al microstructures, both models use 70% of the data samples for training and 30% of the data samples for testing. The material parameters such as Young's modulus and yield strength values computed by the CP simulations (Appendix A) are used as output, while information on the synthesized microstructure images (Figure 4.4) collected by the shape moment invariants (ω & λ) are used as input. Using this collection of data, the surrogate model is trained to predict the material properties of Ti-7Al microstructures, such as Young's modulus and yield strength values.

In Figure 4.9 (a)-(b), the GPR predictions of Model-1 for Young's modulus and yield strength

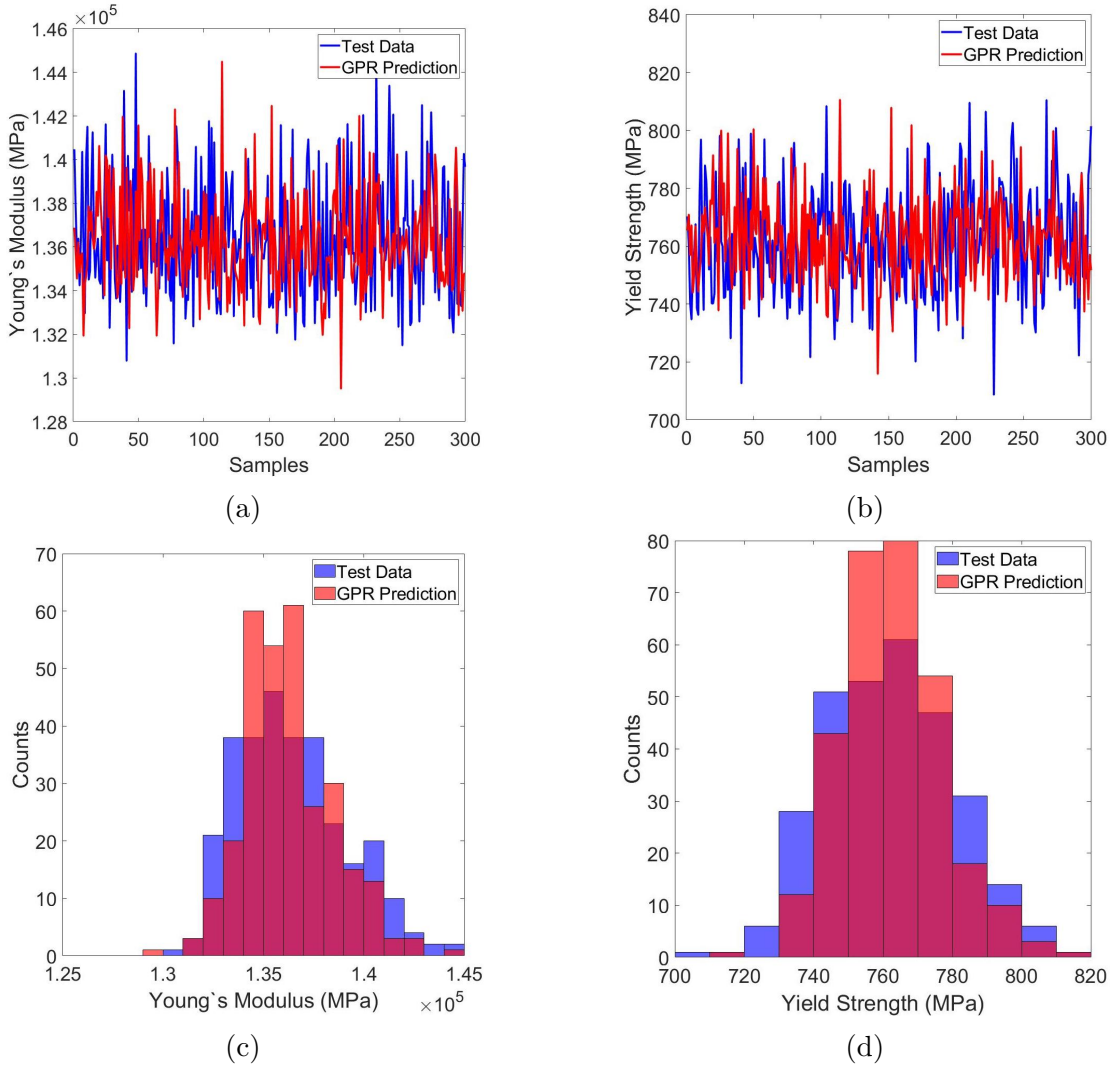

Figure 4.9: Results for surrogate model-1: (a)-(b) Test Data vs. GPR Prediction for the expected values of Young's modulus and yield strength, respectively; (c)-(d) Histograms of Test Data vs. GPR Predictions for Young's modulus and yield strength, respectively [59].

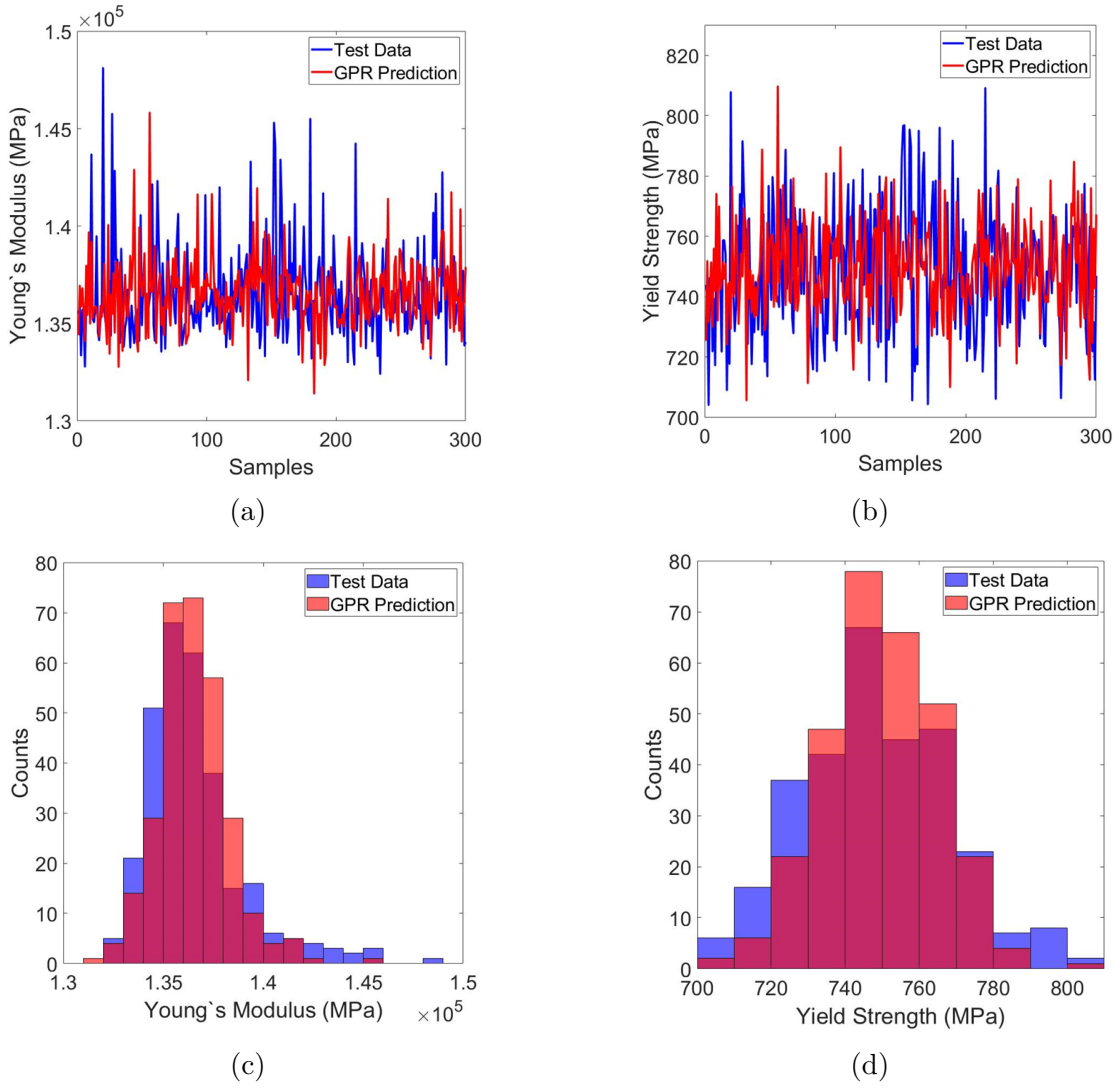

Figure 4.10: Results for surrogate model-2:(a)-(b) GPR predictions and test data for Young's modulus and yield strength respectively, (c)-(d) Probability distributions of 2D additively manufactured microstructures for Young's modulus and yield strength respectively [58].

are shown. The predictions appear to be matching the test data with a combined average error difference of 2.8471 GPa for Young's modulus (E) and for 18.35 MPa for yield strength σ_Y. This error accounts for the uncertainty propagated on the homogenized material properties due to the stochasticity of the microstructure. Also, the CP model prediction for the experimental microstructure (Figure 4.4 (a)) is found to be 133.7456 GPa for Young's modulus and 726.2467 MPa for yield strength. Both values lie within the CP model predictions for the reconstructed microstructures. Furthermore, the GPR predictions capture the distribution of the actual material properties used as the test points, as can be seen in the histograms in Figure 4.9 (c-d).

On the other hand, another surrogate model based on GPR is developed for predicting the material properties of reconstructed samples of additively manufactured microstructures (Figure 4.4 (d)). Here, the mechanical properties, such as Young's modulus and yield strength, are defined as a function of the microstructures represented by the PEM (λ_1 and λ_2). The kriging model uses a polynomial regression along with the exponential correlation function (Equation 4.5) to predict the mechanical properties. The predictions of the surrogate model are illustrated in Figure 4.10. The predictions indicate an average error of 2.1719 GPa and 20.0685 MPa for Young's modulus and yield strength, respectively. The similarity between the GPR-predicted outcomes and test data (Figure 4.10 (a) and (b)) implies that the link between the material properties and PEM may agree with an exponential relationship. The probability distributions of the test data and kriging predictions given in Figure 4.10 (c)-(d) demonstrate a good match. Predictions of both models indicate that the shape moment invariants that contain the invariant property like the Hu moments (RST invariants) can represent the microstructure topology when predicting the material properties. However, compared to other shape moment invariants, PEM has an additional advantage as it can quantify uncertainties. Therefore, PEM is preferable for UQ in addition

to representing the microstructural topology.

Chapter 5

MAGNETIC PHASE TRANSITION

This chapter investigates the ferromagnetic-paramagnetic phase transition problem of magnetic materials using a numerical formulation derived from the Ising model. The permanent magnetic property of ferromagnetic material is deemed to be a desired quality in many aircraft applications. However, the exposure of aircraft components employing ferromagnetic materials to extreme environments affects the magnetic strength of the material. Therefore, it is crucial to study the magnetic phase transition phenomenon to achieve a robust design of aircraft components. In this study, the Ising model-based methodology previously used for microstructure reconstruction with MRF is extended to model the spin-spin interactions of magnetic materials.

In a ferromagnetic material, the crystallographic arrangements of the unparalleled electrons in a uniform direction lead to the formation of small regions called magnetic domains (Figure 5.1 (a)). When an external magnetic field (h) is applied, the ferromagnetic material becomes a permanent magnet as the magnetic domains get aligned in the directions of the applied field. Therefore, ferromagnetic materials have a broad array of applications in a variety of magneto-mechano-electric devices [61]. One of the important applications of ferromagnetic materials is in aircraft engines as electrical generators due to their strong permanent magnetic property. However, when ferromagnetic materials are subjected to higher temperatures, they transform to a different phase where the magnetic spins are randomly aligned leading to a disorderly state called the paramagnetic phase (Figure 5.1 (b)). The temperature at which

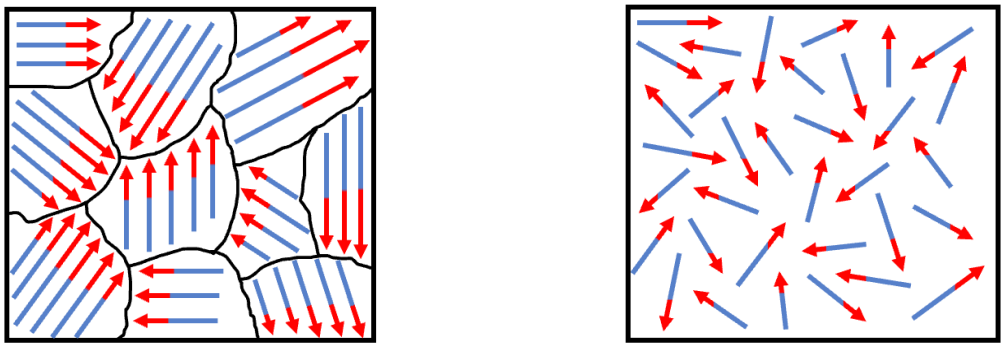

(a) (b)

Figure 5.1: Alignment of magnetic spins in (a) Ferromagnetic and (b) Paramagnetic materials

this transition occurs is called a Curie temperature. Additionally, the interaction between the external magnetic field and the magnetic spins is also known to influence the phase transition. However, the experimental measurement uncertainties in the external magnetic field and temperature (T) propagating on the magnetization and free energy induce a variation in the magnetic phase transition. As a result, a range of critical external magnetic fields and temperatures yields a magnetic phase transition zone. A lack of concrete understanding of the uncertainty-induced magnetic phase transition zone increases the risk of losing the permanent magnetic property of ferromagnetic materials. Hence, it is crucial to study the ferromagnetic-paramagnetic phase transition in order to increase the reliability and design the magneto-mechano-electrical devices used in the aircraft to perform better.

The modeling of ferromagnetic-paramagnetic phase transition is studied through a lattice structure developed by Ising [63] in 1924. However, other models have also been developed in the past for understanding the magnetic phase transition. Notable works include Heisenberg [163], Potts [164], and Baxter-Wu [165] models. The Heisenberg model differs from the Ising in its symmetric property. For example, for a particular spin combination, while the Heisenberg model exhibits global spin rotational symmetry [166], the Ising model has global spin sign flip symmetry [167]. The Potts model has been extensively studied for phase

transition and other research problems [164]. Furthermore, the Baxter-Wu model develops the Ising problem with three spins for a triangle lattice [165]. However, all the aforementioned models are modified forms of the Ising model. Furthermore, experimental validation exists for the Ising model prediction of magnetic phase transition for rare earth materials [168, 169, 170]. Therefore, this work uses the Ising model to represent the physical mechanism of the ferromagnetic-paramagnetic phase transition.

Multiple attempts have been made in the past to address the phase transition problem in magnetic materials using the Ising model [65, 66, 67, 68, 69, 70, 71, 72, 73]. However, they usually account only for the nearest neighbor interactions either in the presence [68, 69, 70, 71, 72, 73] or in the absence of an external magnetic field [74, 65, 66]. Furthermore, the long-range interactions in the Ising model have also been studied but without the external magnetic field [75, 76]. For instance, Hiley et al. [75] derived some general properties of the Ising model with long-range interactions for the disordered state with a zero field. Moreover, Siegert et al. [76] obtained the free energy per spin of the Ising model including long-range interactions but in the absence of the external magnetic field. To address the challenges in the literature, this work presents a novel numerical approach using optimization techniques to study the magnetic phase transition by including the effects of the external magnetic field and long-range interactions between magnetic spins [171]. This objective is accomplished by developing a 2D Ising model that accommodates the long-range interactions among magnetic spins and the external magnetic field.

This chapter is outlined as follows: Section 5.1 describes the developed 2D Ising model accounting for the long-range interactions of magnetic spins and the external magnetic field. Section 5.2 presents the solution obtained for magnetic phase transition using mean-field theory.

5.1 2D Ising model for phase transition

The structure of the 2D Ising model developed for magnetic phase transition follows the same procedure as described in Section 2.1. Accordingly, the lattice points of the Ising model are modeled to represent the magnetic spins of the material. The Hamiltonian energy for any given Ising model considering the effects of the external magnetic field is defined as [172]:

$$H = -\omega_j \Sigma_{<i,j>} \sigma_i \sigma_j - h \Sigma_i \sigma_i \tag{5.1}$$

where h is the external field parameter and σ is the spin parameter. The spin values of a particular node (i) and its corresponding neighbors ($j = 1, 2, ..., N$ where N is the total number of neighbors) are denoted by σ_i and σ_j, respectively. The magnetic spin has only two possible states namely the up spin ($\sigma_i = +1$) and the down spin ($\sigma_i = -1$). The product of σ_i and σ_j represents the interactions between the spins including the long-range spins. The ω_j parameter in Equation 5.1 is defined as a weight parameter for the corresponding level of neighboring information to be used in the Hamiltonian energy expression. The state of any spin is driven by both nearest-neighbor and long-range order interactions. However, the nearest-neighbor spins are more decisive than the far-away spins. Therefore, the weight parameter, ω_j, will be defined for each spin to ensure that nearby neighbors would be more influential than the long-range neighbors to determine the magnetic state of that spin. The following constraint (Equation 5.2) will be defined to acknowledge that the effects of neighboring spins will descend as the order of correlation increases:

$$\omega_n < \omega_{n-1} < \omega_{n-2} < .... < \omega_3 < \omega_2 < \omega_1 \tag{5.2}$$

where n is the maximum order of interactions considered in the Ising model. For example,

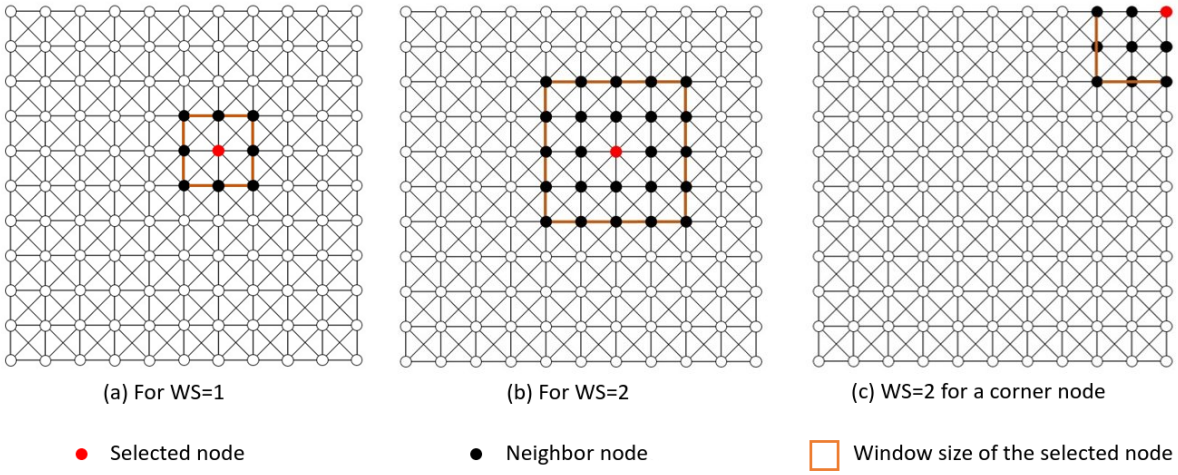

Figure 5.2: 2D Ising model with high-order interactions for (a) WS 1, (b) WS 2 for the center node, and c) WS 2 for a corner node [171].

ω_1 and ω_2 will be used for the nearest-neighbor and the second nearest-neighbor interactions, respectively. The interactions between the magnetic spins are quantified through the weightage parameter (ω) assigned in a square window. For example, the ω value remains constant for all spins along the perimeter of the window but it changes in an arithmetic sequence as the window size increases. In Figure 5.2, an example of how this window size parameter changes for the spins at the center and corner can be seen. In addition, as described in Equation 5.3, ω values are Gaussian distributed and normalized with respect to the total sum. In this study, the determination of spin states will be accomplished using this methodology.

$$\omega = \frac{\omega_1}{\sum_{i=1}^{n} \omega_i}, \frac{\omega_2}{\sum_{i=1}^{n} \omega_i}, ..., \frac{\omega_n}{\sum_{i=1}^{n} \omega_i} \tag{5.3}$$

In the next section, the developed Ising model accounting for the long-range interactions is used to determine if they are equipped to represent the magnetic phase transition by finding the minimum free energy using mean-field theory.

5.2 Mean field theory

Finding an exact solution to the Ising problem is computationally expensive. Because for any given model of size N, the number of spin combinations is 2^N. However, with Mean Field Theory (MFT), it is possible to derive an approximate solution by finding the minimum free energy. MFT is a well-known approach in physics that provides a good approximation to the exact solutions if the number of dimensions is adequately large. It is the most widely used estimation technique for simulating interacting systems [172]. However, the mean-field solutions are still built upon some assumptions regarding the correlations between the interacting spins. In the past, while determining the system's free energy, either the covariance relation between the spins in the long-range [172, 173, 174] or the external magnetic field [75, 76] is neglected due to the computational complexities and costs. Therefore, the mean-field solution will be extended in this study by eliminating the fundamental assumptions made on magnetic spin interactions. With the mean-field approach, the free energy of system F is expressed in terms of the Hamiltonian of the 2D lattice, as given in Equation 5.4:

$$exp(-\beta F) = \Sigma_\sigma exp(-\beta H), \text{where, } \beta = \frac{1}{k_B T} \tag{5.4}$$

where β is the critical exponent defined in terms of the temperature (T) and Boltzmann constant (k_B). According to Equation 5.4, the free energy will increase with the increase in the number of sites N. Hence, to avoid the effects of the finite volume size, the free energy density per site (f) is defined as the free energy divided by the number of sites. The magnetization (m) of the system is related to the first derivative of the free energy density with respect to the external magnetic field, such that $m = -\partial f / \partial h$.

The instability in the magnetic phase transition under the combined effects of the external magnetic field and the temperature is mathematically identified by considering the following

cases:

1) When $T < T_c$, the material is ferromagnetic. Upon applying the external magnetic field, all spins tend to align in the direction of the applied field. However, the state of spins (up or down) can be mathematically determined by analyzing the first-order derivative of the free energy with respect to the external magnetic field ($\frac{\partial f(h,T)}{\partial h}$). When the direction of the applied field is changed, there is a sudden jump in the magnetization of the system as h passes through zero. Due to the sudden jump in the system's magnetization value between $M < 0$ and $M > 0$, a discontinuity occurs at $h = 0$. Therefore, the first-order derivative of the free energy with respect to the external magnetic field diverges indicating that transition as a function of the external magnetic field is a first-order transition problem. Evidently, the first-order transition is observed to occur for a range of temperature values less than T_c [173]. Therefore, when the external magnetic field reaches critical values (h_c), a discontinuity occurring at a single critical location leads to the first-order transition of the magnetic spin state. The first-order derivative is defined as:

$$\frac{\partial f(h,T)}{\partial h} = \lim_{h \to h_c} \frac{f(h_c,T) - f(h,T)}{h_c - h} \to \infty \tag{5.5}$$

2) At $T = T_c$, the thermal energy from the heat source is more than the interaction energy between the magnetic spins of the system leading to the phase transition from the ferromagnetic state to the paramagnetic state. In this case, the first-order derivatives remain continuous. However, a discontinuity occurs in the second-order derivatives of the free energy with respect to the external magnetic field and the temperature. Therefore, the following assumption is made. The second-order derivatives of free energy with respect to the external magnetic field and temperature diverge (approach infinity). Consequently, the magnetic phase transition is theoretically identified by solving the following optimization

problem:

$$min \;\; f(h,T)$$

$$\text{subject to: } \frac{\partial^2 f(h,T)}{\partial h^2}|_{T=T_c} \rightarrow \infty \text{ and } \frac{\partial^2 f(h,T)}{\partial T^2}|_{T=T_c} \rightarrow \infty \tag{5.6}$$

The spin state is identified based on the free energy of the system, which is a function of the external magnetic field and temperature. When an external magnetic field is applied, the system tends to be in the minimum free energy state. Therefore, the Ising model developed to represent magnetic phase transition accounting for long-range interactions is tested by solving the aforementioned optimization problem in Equation 5.6 to find the minimum free energy. However, the constraints are removed for simplification purposes. For a constant $h = 0.01$ and $k_B T = 0.5$, the minimum free energy (Equation 5.4) per number of sites without any constraints is obtained using a genetic algorithm. To verify the optimum solution, an exhaustive search is performed by computing the free energy of all possible combinations for models with dimensions of 2×2, 3×3, and 4×4, as presented in Figure 5.3. Details about the exhaustive solutions for 3×3 and 4×4 domains are displayed in Figure 5.4. The optimized solutions precisely match the exhaustive solutions. Therefore, it can be concluded that the newly introduced ω parameter successfully captures the long-range interactions of magnetic spins during the phase transition. Since the total number of possible combinations for the 4×4 model is 2^{16}, determining the exhaustive solutions for domains larger than 4×4 is computationally impractical. When a positive external magnetic field is introduced, the optimization problem finds a solution in which a model with all positive spins produces the minimum free energy per number of sites. Similarly, when a negative field is applied, the model with all negative spins produces the minimum free energy. This is because the

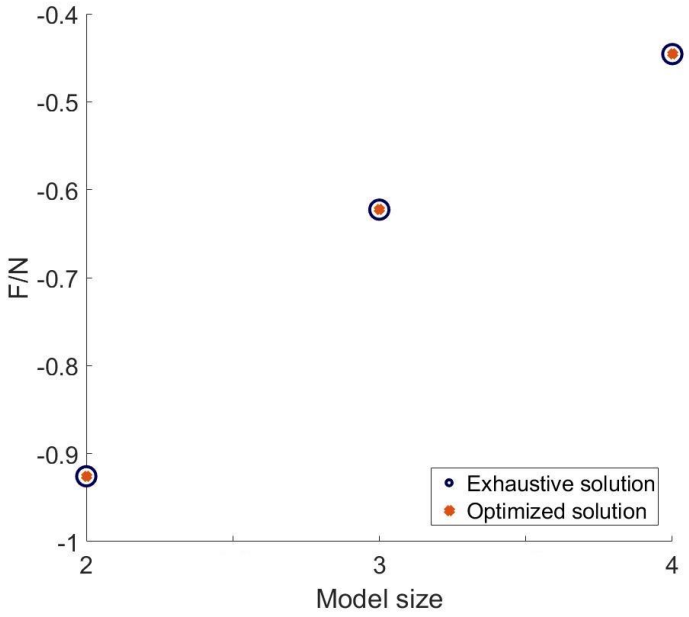

Figure 5.3: Free energy solutions obtained by both exhaustive search and optimization for a 2D Ising model with dimensions 2×2, 3×3, and 4×4 when $h = 0.01$ and $k_B T = 0.5$ [171].

application of an external magnetic field causes a change in the magnetization of each grain of a polycrystalline microstructure and the spins tend to align in the direction of the external magnetic field.

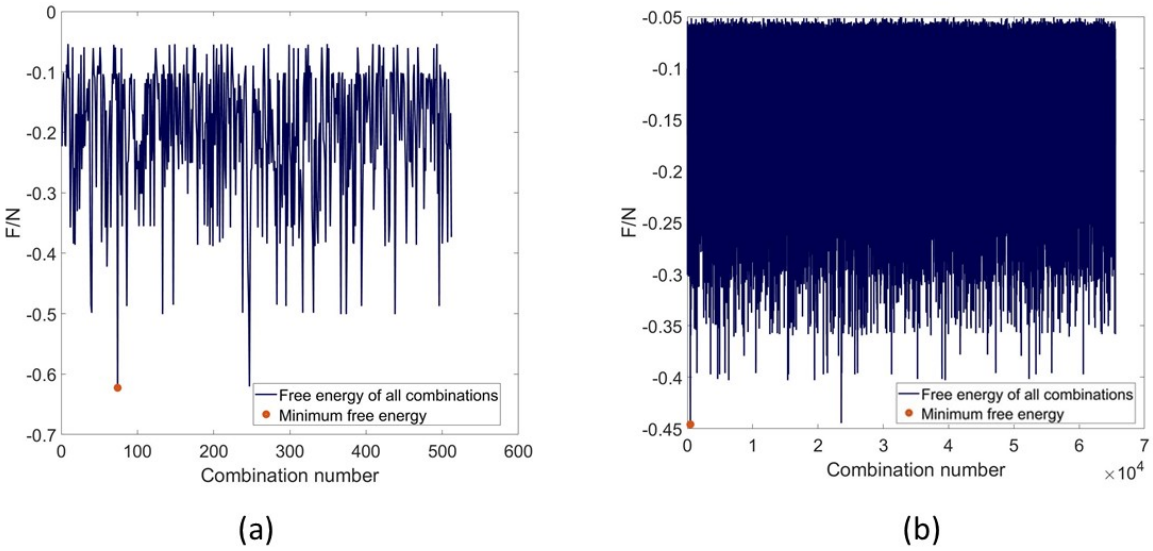

Figure 5.4: Minimum free energy obtained by optimization along with the free energy solutions obtained by exhaustive search for all possible combinations of a 2D Ising model with dimensions 3×3 and 4×4 when $h = 0.01$ and $k_B T = 0.5$ [171].

Chapter 6

CONCLUSIONS AND FUTURE WORK

6.1 Conclusions

This work investigates the multi-scale modeling of Ti-7Al by computationally quantifying and characterizing its microstructural features through the concept of moment invariants. Thus, the presented formulation determines the homogenized material properties as a function of grain topology. A significant data reduction is achieved by quantitatively characterizing the grain topology of Ti-7Al microstructures using PEM. Moreover, the experimental and algorithmic uncertainties propagating on the synthetic microstructures and material properties are quantified through statistical parameters developed based on PEM. Altogether, the findings of the presented research work contribute to the state-of-the-art computational techniques that are used to study the material behavior of Ti-7Al for potential use in many aerospace components. Furthermore, the presented techniques are also designed to be universally applicable to any kind of microstructural topology (e.g., composites, ceramics, etc).

Computational reconstruction of microstructure images alleviates the burden of laborious and tedious experimental methodologies. Therefore, the forged and additively manufactured Ti-7Al alloy experimental images [38] are spatially reconstructed into large domains with the MRF algorithm at different resolutions using different window sizes (Section 3.1). After

reconstruction, the 2D synthesized samples are compared with the experimental data at two levels (Section 3.3). At the global level, the whole microstructure images are quantified and compared through PEM and d_{cr} (Section 3.3.1). At the local level, the grain shapes and sizes of synthetic and experimental images are compared through Hu moments and an equivalent radius parameter (Section 3.3.2).

The 3D synthesized microstructures of Al-Li and 316L stainless steel alloys generated with the MRF algorithm by Refs. [100, 101] are verified by statistically comparing them to the experimental 2D orthogonal images (Section 3.4). To compare the 2D and 3D grains, the normalized central moments (η) that are invariant to shape transformations are proposed as a universal metric. The 3D synthetic microstructures are compared to the experimental images in three planes normal to the X, Y, and Z directions (Figure 3.12 and Figure 3.13). The distributions of 2D and 3D grain shapes quantified by η are found to be similar. The grain topologies are compared in each direction through a box whisker plot (Figure 3.14 and Figure 3.15). Statistical measures derived from the distributions of grain shapes quantified by η (Table 3.6) are used to understand the anisotropic features of the reconstructed microstructures. By developing measures for the computational characterization of microstructures, this work addresses the gap in the mathematical quantification of microstructural topology. The ubiquitous two-step verification methodology for synthetic microstructures and the newly introduced PEM aid the computational techniques in the MCR research field to analyze any type of microstructures. As a result, the developed methods can be applied to complex microstructures such as the ones originating from additively manufactured materials.

Furthermore, this work also addresses the quantification of epistemic and aleatoric uncertainty of microstructural topology and their propagation on the homogenized material properties. To quantify the uncertainty of microstructural features and homogenized prop-

erties arising from the computational reconstruction of the synthetic samples, a graphical map and five novel statistical parameters have been developed based on the PEM (Figure 4.6). Surrogate models are developed for predicting the homogenized material properties of polycrystalline microstructures as a function of crystallographic texture and grain topology using GPR. In order to generate sufficient statistical data, synthetic microstructures are reconstructed from the experimental images of Ti-7Al alloy using the MRF approach. The input microstructure data is characterized with shape moment invariants by quantifying the reconstructed samples of the microstructure. Next, the homogenized material properties such as Young's modulus and yield strength values of the reconstructed microstructures are determined with crystal plasticity simulations (Appendix A) and utilized for training and test data. The performance of the surrogate model in predicting the homogenized material properties is analyzed using ω (Figure 4.9) and λ (Figure 4.10). The developed methodologies for validation, uncertainty quantification, and material property prediction are eligible to be universally applied to any kind of material or reconstruction methodology.

Additionally, this work addresses the ferromagnetic-paramagnetic phase transition by developing a 2D Ising model that considers the long-range spin interactions in the presence of external magnetic fields (Section 5.1). An optimization solution is obtained to identify the spin combinations and critical external magnetic field that cause phase transition to occur (Section 5.2). Furthermore, the optimization solution is verified with exhaustive solutions for small domain sizes (Figure 5.3).

6.2 Future work

1) In Tribology: The present work on microstructure characterization and reconstruction (MCR) has already been extended to a tribology problem where surface maps of Inconel 718

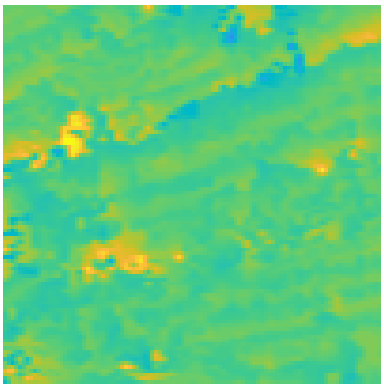

(a) Experimental image (100×100)

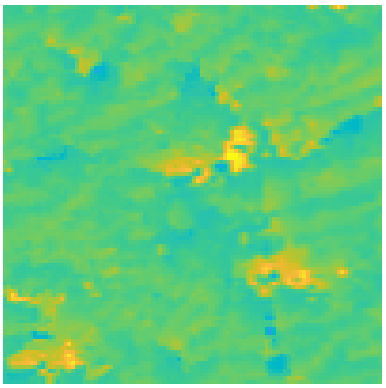

(b) Reconstructed image (100×100).

Figure 6.1: Reconstruction of Inconel-718 surface topology using MRF. Experimental image: Courtesy of Prof. Bart Raeymaekers

have been reconstructed using MRF and synthetic images are verified by the PEM [175] to reduce the experimental cost and time. An example of the preliminary work is presented in Figure 6.1. Additionally, the PEM is also being used in ongoing work to classify the different surface maps. Furthermore, the PEM has a potential application as a shape descriptor for wear particles [176].

2) In Fracture Mechanics: The extension of the presented research on MCR has potential applications in the field of fracture mechanics, which has advanced in recent years through the use of machine learning techniques [177]. However, the advancements still lack thorough validation procedures to verify the synthetic structures. Therefore, by applying the shape quantification techniques (Section 3.4) that have been developed in the presented work, it is possible to validate and improve the quality of the 3D reconstruction of crack propagation. The uncertainty associated with the reconstruction methods used for the crack prediction models is not well-researched [177]. Therefore, the statistical parameters developed in the present work for quantifying the uncertainty of the microstructural topology [58] can be extended to the 3D crack propagation problems.

3) In Additive Manufacturing: The complexity of the microstructure and the manufacturing cost are some of the obstructions in producing additively manufactured materials. However, by computationally reconstructing the additively manufactured microstructure images, it is possible to reduce the experimental cost and time. With the latest developments in the 3D reconstruction of additively manufactured materials [101], it is possible to train a neural network-based surrogate model to extensively study the shapes of 3D grains and quantify them with PEM. With the improved knowledge of various complex grain topologies of additively manufactured microstructures, it is plausible to solve the inverse problem of determining the manufacturing parameters that would need to be set for producing a sample with desired material properties. Solving the inverse problem will help with automating and speeding up the production process.

Bibliography

[1] R. R. Boyer et al. "Materials considerations for aerospace applications". In: *MRS Bulletin* 40.12 (Nov. 2015), pp. 1055–1065. ISSN: 08837694. DOI: 10.1557/MRS.2015.278/FIGURES/5. URL: https://link.springer.com/article/10.1557/mrs.2015.278.

[2] Michael Mohaghegh. "Evolution of Structures Design Philosophy and Criteria". In: *https://doi.org/10.2514/1.11717* 42.4 (May 2012), pp. 814–831. ISSN: 15333868. DOI: 10.2514/1.11717. URL: https://arc.aiaa.org/doi/10.2514/1.11717.

[3] I. Inagaki, Tsutomu Takechi, and Yoshihisa Shirai Nozomu Ariyasu. "Application and Features of Titanium for the Aerospace Industry". In: (2014).

[4] Manfred Peters et al. "Titanium Alloys for Aerospace Applications". In: *Advanced Engineering Materials* 5.6 (June 2003), pp. 419–427. ISSN: 1527-2648. DOI: 10.1002/ADEM.200310095. URL: https://onlinelibrary.wiley.com/doi/10.1002/adem.200310095.

[5] Rodney R. Boyer. "Aerospace applications of beta titanium alloys". In: *JOM* 46.7 (July 1994), pp. 20–23. ISSN: 10474838. DOI: 10.1007/BF03220743/METRICS. URL: https://link.springer.com/article/10.1007/BF03220743.

[6] R. R. Boyer. "An overview on the use of titanium in the aerospace industry". In: *Materials Science and Engineering: A* 213.1-2 (Aug. 1996), pp. 103–114. ISSN: 0921-5093. DOI: 10.1016/0921-5093(96)10233-1.

[7] R. R. Boyer and R. D. Briggs. "The use of β titanium alloys in the aerospace industry". In: *Journal of Materials Engineering and Performance* 14.6 (Dec. 2005), pp. 681–685.

ISSN: 10599495. DOI: 10.1361/105994905X75448/METRICS. URL: https://link.springer.com/article/10.1361/105994905X75448.

[8] R. R. Boyer. "Attributes, characteristics, and applications of titanium and its alloys". In: *JOM* 62.5 (May 2010), pp. 21–24. ISSN: 10474838. DOI: 10.1007/S11837-010-0071-1/METRICS. URL: https://link.springer.com/article/10.1007/s11837-010-0071-1.

[9] James D. Cotton et al. "State of the Art in Beta Titanium Alloys for Airframe Applications". In: *JOM* 67.6 (June 2015), pp. 1281–1303. ISSN: 15431851. DOI: 10.1007/S11837-015-1442-4/FIGURES/25. URL: https://link.springer.com/article/10.1007/s11837-015-1442-4.

[10] Paramjit Singh, Harish Pungotra, and Nirmal S. Kalsi. "On the characteristics of titanium alloys for the aircraft applications". In: *Materials Today: Proceedings* 4.8 (Jan. 2017), pp. 8971–8982. ISSN: 2214-7853. DOI: 10.1016/J.MATPR.2017.07.249.

[11] Renato Altobelli Antunes, Camilo Augusto Fernandes Salvador, and Mara Cristina Lopes De Oliveira. "Materials Selection of Optimized Titanium Alloys for Aircraft Applications". In: *Materials Research* 21.2 (2018), p. 20170979. DOI: 10.1590/1980-5373-MR-2017-0979. URL: http://dx.doi.org/10.1590/1980-5373-MR-2017-0979.

[12] Eckart Uhlmann et al. "Additive Manufacturing of Titanium Alloy for Aircraft Components". In: *Procedia CIRP* 35 (Jan. 2015), pp. 55–60. ISSN: 2212-8271. DOI: 10.1016/J.PROCIR.2015.08.061.

[13] Valentin N. Moiseyev. "Titanium alloys: Russian aircraft and aerospace applications". In: *Titanium Alloys: Russian Aircraft and Aerospace Applications* (Jan. 2005), pp. 1–207.

[14] Ajey Venkataraman et al. "Study of Structure and Deformation Pathways in Ti-7Al Using Atomistic Simulations, Experiments, and Characterization". In: *Metallurgical and Materials Transactions A: Physical Metallurgy and Materials Science* 48.5 (May 2017), pp. 2222–2236. ISSN: 10735623. DOI: 10.1007/S11661-017-4024-Y/FIGURES/17. URL: https://link.springer.com/article/10.1007/s11661-017-4024-y.

[15] James C. Williams and Rodney R. Boyer. "Opportunities and Issues in the Application of Titanium Alloys for Aerospace Components". In: *Metals 2020, Vol. 10, Page 705* 10.6 (May 2020), p. 705. ISSN: 2075-4701. DOI: 10.3390/MET10060705. URL: https://www.mdpi.com/2075-4701/10/6/705/htm%20https://www.mdpi.com/2075-4701/10/6/705.

[16] Jeoung Han Kim et al. "A self-consistent approach for modeling the flow behavior of the alpha and beta phases in Ti-6Al-4V". In: *Metallurgical and Materials Transactions A: Physical Metallurgy and Materials Science* 42.7 (July 2011), pp. 1805–1814. ISSN: 10735623. DOI: 10.1007/S11661-010-0567-X/FIGURES/9. URL: https://link.springer.com/article/10.1007/s11661-010-0567-x.

[17] Harry A. Lipsitt. "Titanium Aluminides - An Overview". In: *MRS Online Proceedings Library (OPL)* 39 (1984), p. 351. ISSN: 0272-9172. DOI: 10.1557/PROC-39-351.

[18] Deniz Ozturk, Shravan Kotha, and Somnath Ghosh. "An uncertainty quantification framework for multiscale parametrically homogenized constitutive models (PHCMs) of polycrystalline Ti alloys". In: *Journal of the Mechanics and Physics of Solids* 148 (Mar. 2021), p. 104294. ISSN: 0022-5096. DOI: 10.1016/J.JMPS.2021.104294.

[19] Pınar Acar. "Crystal Plasticity Model Calibration for Ti-7Al Alloy with a Multi-fidelity Computational Scheme". In: *Integrating Materials and Manufacturing Innovation* 7.4 (Dec. 2018), pp. 186–194. ISSN: 21939772. DOI: 10.1007/S40192-018-0120-

0/FIGURES/6. URL: https://link.springer.com/article/10.1007/s40192-018-0120-0.

[20] Pinar Acar. "Uncertainty Quantification for Ti-7Al Alloy Microstructure with an Inverse Analytical Model (AUQLin)". In: *Materials 2019, Vol. 12, Page 1773* 12.11 (May 2019), p. 1773. ISSN: 1996-1944. DOI: 10.3390/MA12111773. URL: https://www.mdpi.com/1996-1944/12/11/1773.

[21] Arnas Gerald Fitzner. "EFFECTS OF ALLOYING ELEMENTS ON TWINNING IN !LPHA-TITANIUM ALLOYS". In: ().

[22] Anna Radecka et al. "Ordering and the micromechanics of Ti–7Al". In: *Materials Science and Engineering: A* 650 (Jan. 2016), pp. 28–37. ISSN: 0921-5093. DOI: 10.1016/J.MSEA.2015.09.070.

[23] C. Hodonou et al. "Material-design-process selection methodology for aircraft structural components: application to additive vs subtractive manufacturing processes". In: *International Journal of Advanced Manufacturing Technology* 103.1-4 (July 2019), pp. 1509–1517. ISSN: 14333015. DOI: 10.1007/S00170-019-03613-5/METRICS. URL: https://link.springer.com/article/10.1007/s00170-019-03613-5.

[24] Yifan Lv. "Additive Manufacturing for the Aircraft Industry: A Review". In: (2019). DOI: 10.4172/2329-6542.1000214. URL: https://www.researchgate.net/publication/331482685.

[25] P A Kobryn et al. "Additive Manufacturing of Aerospace Alloys for Aircraft Structures". In: (). URL: http://www.rto.nato.int/abstracts.asp..

[26] Chris L. Pettit. "Uncertainty Quantification in Aeroelasticity: Recent Results and Research Challenges". In: *https://doi.org/10.2514/1.3961* 41.5 (May 2012), pp. 1217–

1229. ISSN: 15333868. DOI: 10.2514/1.3961. URL: https://arc.aiaa.org/doi/10.2514/1.3961.

[27] A. Kumar et al. "A Markov random field approach for microstructure synthesis". In: *Modelling and Simulation in Materials Science and Engineering* 24.3 (Mar. 2016), p. 035015. ISSN: 0965-0393. DOI: 10.1088/0965-0393/24/3/035015. URL: https://iopscience.iop.org/article/10.1088/0965-0393/24/3/035015/meta.

[28] Pinar Acar and Veera Sundararaghavan. "A Markov random field approach for modeling spatio-temporal evolution of microstructures". In: *Modelling and Simulation in Materials Science and Engineering* 24.7 (Sept. 2016), p. 075005. ISSN: 0965-0393. DOI: 10.1088/0965-0393/24/7/075005. URL: https://iopscience.iop.org/article/10.1088/0965-0393/24/7/075005/meta.

[29] Albert Bijaoui and Frédéric Rué. "A multiscale vision model adapted to the astronomical images". In: *Signal Processing* 46.3 (Oct. 1995), pp. 345–362. ISSN: 0165-1684. DOI: 10.1016/0165-1684(95)00093-4.

[30] Jay D. Martin and Timothy W. Simpson. "Use of Kriging Models to Approximate Deterministic Computer Models". In: *https://doi.org/10.2514/1.8650* 43.4 (May 2012), pp. 853–863. ISSN: 00011452. DOI: 10.2514/1.8650. URL: https://arc.aiaa.org/doi/10.2514/1.8650.

[31] M. F. Horstemeyer. "Multiscale modeling: A review". In: *Practical Aspects of Computational Chemistry: Methods, Concepts and Applications* (2010), pp. 87–135. DOI: 10.1007/978-90-481-2687-3{_}4/FIGURES/11{_}4. URL: https://link.springer.com/chapter/10.1007/978-90-481-2687-3_4.

[32] Rosa E. Bulo et al. "Multiscale modeling of chemistry in water: Are we there yet?" In: *Journal of Chemical Theory and Computation* 9.12 (Dec. 2013), pp. 5567–5577.

ISSN: 15499618. DOI: 10.1021/CT4005596/SUPPL{_}FILE/CT4005596{_}SI{_}001.PDF. URL: https://pubs.acs.org/doi/full/10.1021/ct4005596.

[33] Rob Phillips. "Multiscale modeling in the mechanics of materials". In: *Current Opinion in Solid State and Materials Science* 3.6 (Dec. 1998), pp. 526–532. ISSN: 1359-0286. DOI: 10.1016/S1359-0286(98)80020-X.

[34] J. A. Elliott. "Novel approaches to multiscale modelling in materials science". In: *International Materials Reviews* 56.4 (July 2011), pp. 207–225. ISSN: 09506608. DOI: 10.1179/1743280410Y.0000000002/SUPPL{_}FILE/YIMR{_}A{_}11664829{_}SM0003.AVI. URL: https://www.tandfonline.com/doi/abs/10.1179/1743280410Y.0000000002.

[35] Z. C. Cordero, B. E. Knight, and C. A. Schuh. "Six decades of the Hall–Petch effect – a survey of grain-size strengthening studies on pure metals". In: 61.8 (Nov. 2016), pp. 495–512. ISSN: 17432804. DOI: 10.1080/09506608.2016.1191808.

[36] *» Bearing research: going to the atomic scale*. URL: https://evolution.skf.com/en/bearing-research-going-to-the-atomic-scale/.

[37] *Unraveling atomic-scale edge structure of nanoscale graphene islands*. URL: https://phys.org/news/2014-07-unraveling-atomic-scale-edge-nanoscale-graphene.html.

[38] Anna M Trump and John E Allison. "The Influence of Aluminum Concentration on Static Recrystallization in Alpha Titanium Alloys". In: *Proceedings of the 13th World Conference on Titanium* (May 2016), pp. 695–696. DOI: 10.1002/9781119296126.CH115. URL: https://onlinelibrary.wiley.com/doi/10.1002/9781119296126.ch115.

[39] *Mechanics of Composite Materials – Institute for Building Materials | ETH Zurich*. URL: https://ifb.ethz.ch/education/msc-courses/Mechanicsofcompositematerials.html.

[40] *Considering Aircraft Engine Condition Monitoring*. URL: https://sassofia.com/blog/considering-aircraft-engine-condition-monitoring-modules-life-limited-parts-llps/.

[41] Viggo Tvergaard. "Material Failure by Void Growth to Coalescence". In: *Advances in Applied Mechanics* 27.C (Jan. 1989), pp. 83–151. ISSN: 0065-2156. DOI: 10.1016/S0065-2156(08)70195-9.

[42] C. Frederic Smith, Braden Lapp, and Michael G. Glavicic. "Uncertainty quantification of material mechanical properties using surrogate models". In: *17th AIAA/ISSMO Multidisciplinary Analysis and Optimization Conference* (2016). DOI: 10.2514/6.2016-3998. URL: https://arc.aiaa.org/doi/10.2514/6.2016-3998.

[43] Claudio Zambaldi et al. "Orientation informed nanoindentation of α-titanium: Indentation pileup in hexagonal metals deforming by prismatic slip". In: *Journal of Materials Research* 27.1 (Jan. 2012), pp. 356–367. ISSN: 08842914. DOI: 10.1557/JMR.2011.334/FIGURES/TAB5. URL: https://link.springer.com/article/10.1557/jmr.2011.334.

[44] Stuart I. Wright. "Fundamentals of Automated EBSD". In: *Electron Backscatter Diffraction in Materials Science* (2000), pp. 51–64. DOI: 10.1007/978-1-4757-3205-4{_}5. URL: https://link.springer.com/chapter/10.1007/978-1-4757-3205-4_5.

[45] Stuart I. Wright and Matthew M. Nowell. "EBSD Image Quality Mapping". In: *Microscopy and Microanalysis* 12.01 (Feb. 2006), pp. 72–84. ISSN: 1431-9276. DOI: 10.1017/S1431927606060090.

[46] Adam J. Schwartz et al. “Electron backscatter diffraction in materials science”. In: *Electron Backscatter Diffraction in Materials Science* (2009), pp. 1–403. DOI: 10.1007/978-0-387-88136-2/COVER.

[47] Brent L. Adams, Stuart I. Wright, and Karsten Kunze. “Orientation imaging: The emergence of a new microscopy”. In: *Metallurgical Transactions A 1993 24:4* 24.4 (Apr. 1993), pp. 819–831. ISSN: 1543-1940. DOI: 10.1007/BF02656503. URL: https://link.springer.com/article/10.1007/BF02656503.

[48] D. J. Dingley and V. Randle. “Microtexture determination by electron back-scatter diffraction”. In: *Journal of Materials Science 1992 27:17* 27.17 (Sept. 1992), pp. 4545–4566. ISSN: 1573-4803. DOI: 10.1007/BF01165988. URL: https://link.springer.com/article/10.1007/BF01165988.

[49] F. J. Humphreys. “Characterisation of fine-scale microstructures by electron backscatter diffraction (EBSD)”. In: *Scripta Materialia* 51.8 (Oct. 2004), pp. 771–776. ISSN: 1359-6462. DOI: 10.1016/J.SCRIPTAMAT.2004.05.016.

[50] N. Tamura et al. “High spatial resolution grain orientation and strain mapping in thin films using polychromatic submicron x-ray diffraction”. In: *Applied Physics Letters* 80.20 (May 2002), p. 3724. ISSN: 0003-6951. DOI: 10.1063/1.1477621. URL: https://aip.scitation.org/doi/abs/10.1063/1.1477621.

[51] Wolfgang Ludwig et al. “X-ray diffraction contrast tomography: A novel technique for three-dimensional grain mapping of polycrystals. I. Direct beam case”. In: *Journal of Applied Crystallography* 41.2 (Mar. 2008), pp. 302–309. ISSN: 00218898. DOI: 10.1107/S0021889808001684/HX5063SUP2.AVI. URL: http://scripts.iucr.org/cgi-bin/paper?hx5063.

[52] W. Ludwig et al. “Three-dimensional grain mapping by x-ray diffraction contrast tomography and the use of Friedel pairs in diffraction data analysis”. In: *Review of*

Scientific Instruments 80.3 (Mar. 2009), p. 033905. ISSN: 0034-6748. DOI: 10.1063/1.3100200. URL: https://aip.scitation.org/doi/abs/10.1063/1.3100200.

[53] Greg Johnson et al. "X-ray diffraction contrast tomography: a novel technique for three-dimensional grain mapping of polycrystals. II. The combined case". In: *urn:issn:0021-8898* 41.2 (Mar. 2008), pp. 310–318. ISSN: 0021-8898. DOI: 10.1107/S0021889808001726. URL: http://scripts.iucr.org/cgi-bin/paper?hx5064.

[54] S. A. McDonald et al. "Non-destructive mapping of grain orientations in 3D by laboratory X-ray microscopy". In: *Scientific Reports* 5.1 (Dec. 2015), p. 14665. ISSN: 2045-2322. DOI: 10.1038/srep14665.

[55] Ramin Bostanabad et al. "Computational microstructure characterization and reconstruction: Review of the state-of-the-art techniques". In: *Progress in Materials Science* 95 (June 2018), pp. 1–41. ISSN: 0079-6425. DOI: 10.1016/J.PMATSCI.2018.01.005.

[56] A. Senthilnathan, P. Acar, and M. De Graef. "Markov Random Field based microstructure reconstruction using the principal image moments". In: *Materials Characterization* 178 (2021). ISSN: 10445803. DOI: 10.1016/j.matchar.2021.111281.

[57] Arulmurugan Senthilnathan and Pınar Acar. "Shape moment invariants as a new methodology for uncertainty quantification in microstructures". In: *AIAA Scitech 2021 Forum* (2021), pp. 1–13. DOI: 10.2514/6.2021-1697. URL: https://arc.aiaa.org/doi/10.2514/6.2021-1697.

[58] Arulmurugan Senthilnathan et al. "Uncertainty quantification of metallic microstructures using principal image moments". In: *Computational Materials Science* 215 (Dec. 2022), p. 111775. ISSN: 0927-0256. DOI: 10.1016/J.COMMATSCI.2022.111775.

[59] A. Senthilnathan and P. Acar. "Multi-Scale Modeling for Texture and Grain Topology of Polycrystalline Microstructures under Uncertainty". In: *AIAA Science and Tech-*

nology Forum and Exposition, AIAA SciTech Forum 2022. 2022. ISBN: 9781624106316. DOI: 10.2514/6.2022-2106.

[60] Arulmurugan Senthilnathan et al. "Computational Characterization and Model Verification for 3D Microstructure Reconstruction of Additively Manufactured Materials". In: (Jan. 2023). DOI: 10.2514/6.2023-1087. URL: https://arc.aiaa.org/doi/10.2514/6.2023-1087.

[61] Alex Goldman. "Applications and Functions of Ferromagnetic Materials". In: *Handbook of Modern Ferromagnetic Materials* (1999), pp. 1–15. DOI: 10.1007/978-1-4615-4917-8{_}1. URL: https://link.springer.com/chapter/10.1007/978-1-4615-4917-8_1.

[62] Adrian P. Mouritz. *Introduction to Aerospace Materials*. Elsevier Inc., May 2012, pp. 1–621. ISBN: 9781855739468. DOI: 10.2514/4.869198. URL: http://www.sciencedirect.com:5070/book/9781855739468/introduction-to-aerospace-materials.

[63] E Ising. "Beitrag zur theorie des ferro-und paramagnetismus". In: (1924). URL: http://www.icmp.lviv.ua/ising/books/isingshort.pdf.

[64] Stephen G. Brush. "History of the Lenz-Ising Model". In: *Reviews of Modern Physics* 39.4 (Oct. 1967), p. 883. ISSN: 00346861. DOI: 10.1103/RevModPhys.39.883. URL: https://journals.aps.org/rmp/abstract/10.1103/RevModPhys.39.883.

[65] M. K. Ramazanov and A. K. Murtazaev. "Phase transitions and critical characteristics in the layered antiferromagnetic Ising model with next-nearest-neighbor intralayer interactions". In: *JETP Letters* 101.10 (May 2015), pp. 714–718. ISSN: 10906487. DOI: 10.1134/S0021364015100100/METRICS. URL: https://link.springer.com/article/10.1134/S0021364015100100.

[66] M. K. Ramazanov et al. “Phase transitions and thermodynamic properties of antiferromagnetic Ising model with next-nearest-neighbor interactions on the Kagomé lattice”. In: *https://doi.org/10.1080/01411594.2018.1428975* 91.6 (June 2018), pp. 610–618. ISSN: 10290338. DOI: 10.1080/01411594.2018.1428975. URL: https://www.tandfonline.com/doi/abs/10.1080/01411594.2018.1428975.

[67] A. F. Sonsin et al. “Computational Analysis of 3D Ising Model Using Metropolis Algorithms”. In: *Journal of Physics: Conference Series* 630.1 (July 2015), p. 012057. ISSN: 1742-6596. DOI: 10.1088/1742-6596/630/1/012057. URL: https://iopscience.iop.org/article/10.1088/1742-6596/630/1/012057/meta.

[68] K. Binder and K. Schröder. “Phase transitions of a nearest-neighbor Ising-model spin glass”. In: *Physical Review B* 14.5 (Sept. 1976), p. 2142. ISSN: 01631829. DOI: 10.1103/PhysRevB.14.2142. URL: https://journals.aps.org/prb/abstract/10.1103/PhysRevB.14.2142.

[69] Rodrigo Bissacot and Leandro Cioletti. “Phase transition in ferromagnetic ising models with non-uniform external magnetic fields”. In: *Journal of Statistical Physics* 139.5 (June 2010), pp. 769–778. ISSN: 00224715. DOI: 10.1007/S10955-010-9961-4/METRICS. URL: https://link.springer.com/article/10.1007/s10955-010-9961-4.

[70] F. R. Nardi, E. Olivieri, and M. Zahradník. “On the Ising model with strongly anisotropic external field”. In: *Journal of Statistical Physics* 97.1-2 (1999), pp. 87–144. ISSN: 00224715. DOI: 10.1023/A:1004662917583/METRICS. URL: https://link.springer.com/article/10.1023/A:1004662917583.

[71] Jian Ding, Jian Song, and Rongfeng Sun. “A new correlation inequality for Ising models with external fields”. In: *Probability Theory and Related Fields* (Apr. 2022),

pp. 1–16. ISSN: 14322064. DOI: 10.1007/S00440-022-01132-1/METRICS. URL: https://link.springer.com/article/10.1007/s00440-022-01132-1.

[72] S. R. Salinas and W. F. Wreszinski. "On the mean-field Ising model in a random external field". In: *Journal of Statistical Physics* 41.1-2 (Oct. 1985), pp. 299–313. ISSN: 00224715. DOI: 10.1007/BF01020615/METRICS. URL: https://link.springer.com/article/10.1007/BF01020615.

[73] Yuan Da Liao et al. "Phase diagram of the quantum Ising model on a triangular lattice under external field". In: *Physical Review B* 103.10 (Mar. 2021), p. 104416. ISSN: 24699969. DOI: 10.1103/PHYSREVB.103.104416/FIGURES/8/MEDIUM. URL: https://journals.aps.org/prb/abstract/10.1103/PhysRevB.103.104416.

[74] Robert G barowski. "Monte Carlo simulations of the Ising model on a square lattice with random Gaussian interactions". In: *https://www.ejournals.eu/Czasopismo-Techniczne/* 2014.Nauki Podstawowe Zeszyt 3 NP (17) 2014 (Feb. 2015), pp. 51–57. ISSN: 2353-737X. DOI: 10.4467/2353737XCT.14.312.3400. URL: https://www.ejournals.eu/Czasopismo-Techniczne/2014/Nauki-Podstawowe-Zeszyt-3-NP-(17)-2014/art/4176/.

[75] B. J. Hiley and G. S. Joyce. "The Ising model with long-range interactions". In: *Proceedings of the Physical Society* 85.3 (Mar. 1965), p. 493. ISSN: 0370-1328. DOI: 10.1088/0370-1328/85/3/310. URL: https://iopscience.iop.org/article/10.1088/0370-1328/85/3/310/meta.

[76] A J F Siegert and David J Vezzetti. "On the Ising Model with Long-Range Interaction". In: *II. Critical-Region Analysis Journal of Mathematical Physics* 9 (1968), p. 2193. DOI: 10.1063/1.1664558. URL: https://doi.org/10.1063/1.1664558.

[77] Ming Kuei Hu. "Visual Pattern Recognition by Moment Invariants". In: *IRE Transactions on Information Theory* 8.2 (1962), pp. 179–187. ISSN: 21682712. DOI: 10.1109/TIT.1962.1057692.

[78] D J Dingley and V Randle. *Review Microtexture determination by electron back-scatter diffraction*. Tech. rep. 1992, pp. 4545–4566.

[79] S. I. Wright. "Orientation Texture". In: *Encyclopedia of Condensed Matter Physics* (Jan. 2005), pp. 221–233. DOI: 10.1016/B0-12-369401-9/00696-3.

[80] C. L.Y. Yeong and S. Torquato. "Reconstructing random media". In: *Physical Review E* 57.1 (Jan. 1998), p. 495. ISSN: 1063651X. DOI: 10.1103/PhysRevE.57.495. URL: https://journals.aps.org/pre/abstract/10.1103/PhysRevE.57.495.

[81] Ramin Bostanabad. "Reconstruction of 3D Microstructures from 2D Images via Transfer Learning". In: *Computer-Aided Design* 128 (Nov. 2020), p. 102906. ISSN: 0010-4485. DOI: 10.1016/J.CAD.2020.102906.

[82] Xiaolin Li et al. "A Transfer Learning Approach for Microstructure Reconstruction and Structure-property Predictions". In: *Scientific Reports 2018 8:1* 8.1 (Sept. 2018), pp. 1–13. ISSN: 2045-2322. DOI: 10.1038/s41598-018-31571-7. URL: https://www.nature.com/articles/s41598-018-31571-7.

[83] C. L.Y. Yeong and S. Torquato. "Reconstructing random media. II. Three-dimensional media from two-dimensional cuts". In: *Physical Review E* 58.1 (July 1998), p. 224. ISSN: 1063651X. DOI: 10.1103/PhysRevE.58.224. URL: https://journals.aps.org/pre/abstract/10.1103/PhysRevE.58.224.

[84] David M. Saylor et al. "Statistically representative three-dimensional microstructures based on orthogonal observation sections". In: *Metallurgical and Materials Transactions A 2004 35:7* 35.7 (2004), pp. 1969–1979. ISSN: 1543-1940. DOI: 10.1007/S11661-

004-0146-0. URL: https://link.springer.com/article/10.1007/s11661-004-0146-0.

[85] Hongyi Xu et al. "Descriptor-based methodology for statistical characterization and 3D reconstruction of microstructural materials". In: *Computational Materials Science* 85 (Apr. 2014), pp. 206–216. ISSN: 0927-0256. DOI: 10.1016/J.COMMATSCI.2013.12.046. URL: https://www.scholars.northwestern.edu/en/publications/descriptor-based-methodology-for-statistical-characterization-and.

[86] A. Brahme et al. "3D reconstruction of microstructure in a commercial purity aluminum". In: *Scripta Materialia* 55.1 (July 2006), pp. 75–80. ISSN: 1359-6462. DOI: 10.1016/J.SCRIPTAMAT.2006.02.017.

[87] Veeraraghavan Sundararaghavan and Nicholas Zabaras. "Classification and reconstruction of three-dimensional microstructures using support vector machines". In: *Computational Materials Science* 32.2 (Feb. 2005), pp. 223–239. ISSN: 0927-0256. DOI: 10.1016/J.COMMATSCI.2004.07.004.

[88] Anindya Bhaduri et al. "An efficient optimization based microstructure reconstruction approach with multiple loss functions". In: *Computational Materials Science* 199 (Nov. 2021), p. 110709. ISSN: 0927-0256. DOI: 10.1016/J.COMMATSCI.2021.110709.

[89] Ramin Bostanabad et al. "Stochastic microstructure characterization and reconstruction via supervised learning". In: *Acta Materialia* 103 (Jan. 2016), pp. 89–102. ISSN: 1359-6454. DOI: 10.1016/J.ACTAMAT.2015.09.044.

[90] Jinlong Fu et al. "Stochastic reconstruction of 3D microstructures from 2D cross-sectional images using machine learning-based characterization". In: *Computer Methods in Applied Mechanics and Engineering* 390 (Feb. 2022), p. 114532. ISSN: 0045-7825. DOI: 10.1016/J.CMA.2021.114532.

[91] Mark D. Rintoul and Salvatore Torquato. "Reconstruction of the Structure of Dispersions". In: *Journal of Colloid and Interface Science* 186.2 (Feb. 1997), pp. 467–476. ISSN: 0021-9797. DOI: 10.1006/JCIS.1996.4675.

[92] N. Sheehan and S. Torquato. "Generating microstructures with specified correlation functions". In: *Journal of Applied Physics* 89.1 (Dec. 2000), p. 53. ISSN: 0021-8979. DOI: 10.1063/1.1327609. URL: https://aip.scitation.org/doi/abs/10.1063/1.1327609.

[93] Yu Liu et al. "Computational microstructure characterization and reconstruction for stochastic multiscale material design". In: *Computer-Aided Design* 45.1 (Jan. 2013), pp. 65–76. ISSN: 0010-4485. DOI: 10.1016/J.CAD.2012.03.007.

[94] Ali Hasanabadi et al. "3D microstructural reconstruction of heterogeneous materials from 2D cross sections: A modified phase-recovery algorithm". In: *Computational Materials Science* 111 (Jan. 2016), pp. 107–115. ISSN: 0927-0256. DOI: 10.1016/J.COMMATSCI.2015.09.015.

[95] David T. Fullwood, Stephen R. Niezgoda, and Surya R. Kalidindi. "Microstructure reconstructions from 2-point statistics using phase-recovery algorithms". In: *Acta Materialia* 56.5 (Mar. 2008), pp. 942–948. ISSN: 1359-6454. DOI: 10.1016/J.ACTAMAT.2007.10.044.

[96] Sriram Ganesan, Iman Javaheri, and Veera Sundararaghavan. "Constrained Voronoi models for interpreting surface microstructural measurements". In: *Mechanics of Materials* 159 (Aug. 2021), p. 103892. ISSN: 0167-6636. DOI: 10.1016/J.MECHMAT.2021.103892.

[97] Anh Tran and Hoang Tran. "Data-driven high-fidelity 2D microstructure reconstruction via non-local patch-based image inpainting". In: *Acta Materialia* 178 (Oct. 2019), pp. 207–218. ISSN: 1359-6454. DOI: 10.1016/J.ACTAMAT.2019.08.007.

[98] T. J. Turner et al. "The influence of microstructure on surface strain distributions in a nickel micro-tension specimen". In: *Modelling and Simulation in Materials Science and Engineering* 21.1 (Nov. 2012), p. 015002. ISSN: 0965-0393. DOI: 10.1088/0965-0393/21/1/015002. URL: https://iopscience.iop.org/article/10.1088/0965-0393/21/1/015002/meta.

[99] Andrea Nicolas et al. "Reconstruction methods and analysis of subsurface uncertainty for anisotropic microstructures". In: *Materials Science and Engineering A* 760 (July 2019), pp. 76–87. ISSN: 09215093. DOI: 10.1016/J.MSEA.2019.05.089.

[100] Iman Javaheri and Veera Sundararaghavan. "Polycrystalline Microstructure Reconstruction Using Markov Random Fields and Histogram Matching". In: *Computer-Aided Design* 120 (Mar. 2020), p. 102806. ISSN: 0010-4485. DOI: 10.1016/J.CAD.2019.102806.

[101] Iman Javaheri, Mohsen Taheri Andani, and Veera Sundararaghavan. "Large-Scale Synthesis of Metal Additively-Manufactured Microstructures Using Markov Random Fields". In: *Computational Materials Science* 206 (Apr. 2022), p. 111228. ISSN: 0927-0256. DOI: 10.1016/J.COMMATSCI.2022.111228.

[102] Veera Sundararaghavan. "Reconstruction of three-dimensional anisotropic microstructures from two-dimensional micrographs imaged on orthogonal planes". In: *Integrating Materials and Manufacturing Innovation* 3.1 (Dec. 2014), pp. 240–250. ISSN: 21939772. DOI: 10.1186/S40192-014-0019-3/TABLES/1. URL: https://link.springer.com/article/10.1186/s40192-014-0019-3.

[103] Siwen Gao et al. "A Markov random field approach for microstructure synthesis". In: *Modelling and Simulation in Materials Science and Engineering* 24.3 (Mar. 2016), p. 035015. ISSN: 0965-0393. DOI: 10.1088/0965-0393/24/3/035015. URL: https://iopscience.iop.org/article/10.1088/0965-0393/24/3/035015/meta.

[104] Daphne Koller and Nir. Friedman. "Probabilistic graphical models : principles and techniques". In: (), p. 1626.

[105] P. G. Callahan, M. Groeber, and M. De Graef. "Towards a quantitative comparison between experimental and synthetic grain structures". In: *Acta Materialia* 111 (June 2016), pp. 242–252. ISSN: 1359-6454. DOI: 10.1016/J.ACTAMAT.2016.03.078.

[106] B. J. Inkson, M. Mulvihill, and G. Möbus. "3D determination of grain shape in a FeAl-based nanocomposite by 3D FIB tomography". In: *Scripta Materialia* 45.7 (Oct. 2001), pp. 753–758. ISSN: 1359-6462. DOI: 10.1016/S1359-6462(01)01090-9.

[107] Melissa R. Cox and Muniram Budhu. "A practical approach to grain shape quantification". In: *Engineering Geology* 96.1-2 (Jan. 2008), pp. 1–16. ISSN: 0013-7952. DOI: 10.1016/J.ENGGEO.2007.05.005.

[108] Bruno Bernard-Michel et al. "Classification of Crystal Shape Using Fourier Descriptors and Mathematical Morphology". In: *Particle & Particle Systems Characterization* 14.4 (Aug. 1997), pp. 193–200. ISSN: 1521-4117. DOI: 10.1002/PPSC.199700041. URL: https://onlinelibrary.wiley.com/doi/10.1002/ppsc.199700041.

[109] James H. Steele. "The Minkowski Functionals: The Global Parameters of Microstructure". In: *Microscopy and Microanalysis* 10.S02 (2004), pp. 712–713. ISSN: 1435-8115. DOI: 10.1017/S143192760488351X.

[110] Jens Schmalzing and Krzysztof M. Górski. "Minkowski functionals used in the morphological analysis of cosmic microwave background anisotropy maps". In: *Monthly Notices of the Royal Astronomical Society* 297.2 (June 1998), pp. 355–365. ISSN: 0035-8711. DOI: 10.1046/J.1365-8711.1998.01467.X. URL: https://academic.oup.com/mnras/article/297/2/355/988332.

[111] J Steele. "Characterizing 3D Microstructure using the Minkowski Functionals". In: *Microscopy and Microanalysis* 13.S02 (Aug. 2007), pp. 1658–1659. ISSN: 1435-8115. DOI: 10.1017/S1431927607075691.

[112] Y. Bhandari et al. "3D polycrystalline microstructure reconstruction from FIB generated serial sections for FE analysis". In: *Computational Materials Science* 41.2 (Dec. 2007), pp. 222–235. ISSN: 0927-0256. DOI: 10.1016/J.COMMATSCI.2007.04.007.

[113] Abhik Choudhury et al. "Quantification and classification of microstructures in ternary eutectic alloys using 2-point spatial correlations and principal component analyses". In: *Acta Materialia* 110 (May 2016), pp. 131–141. ISSN: 1359-6454. DOI: 10.1016/J.ACTAMAT.2016.03.010.

[114] Ahmet Cecen, Tony Fast, and Surya R. Kalidindi. "Versatile algorithms for the computation of 2-point spatial correlations in quantifying material structure". In: *Integrating Materials and Manufacturing Innovation* 5.1 (Dec. 2016), pp. 1–15. ISSN: 21939772. DOI: 10.1186/S40192-015-0044-X/TABLES/1. URL: https://link.springer.com/article/10.1186/s40192-015-0044-x.

[115] A. Tewari et al. "Quantitative characterization of spatial clustering in three-dimensional microstructures using two-point correlation functions". In: *Acta Materialia* 52.2 (Jan. 2004), pp. 307–319. ISSN: 1359-6454. DOI: 10.1016/J.ACTAMAT.2003.09.016.

[116] S Torquato and HW Haslach. "Random Heterogeneous Materials: Microstructure and Macroscopic Properties". In: *Applied Mechanics Reviews* 55.4 (July 2002), B62–B63. ISSN: 0003-6900. DOI: 10.1115/1.1483342. URL: https://asmedigitalcollection.asme.org/appliedmechanicsreviews/article/55/4/B62/458303/Random-Heterogeneous-Materials-Microstructure-and.

[117] J. MacSleyne et al. "Three-dimensional analysis of secondary γ precipitates in René-88 DT and UMF-20 superalloys". In: *Acta Materialia* 57.20 (Dec. 2009), pp. 6251–6267. ISSN: 1359-6454. DOI: 10.1016/J.ACTAMAT.2009.08.053.

[118] *Representation and Reconstruction of Three-dimensional Microstructures in Ni-based Superalloys*. URL: https://apps.dtic.mil/sti/citations/ADA547559.

[119] Lily Nguyen et al. "Quantification of rafting of γ precipitates in Ni-based superalloys". In: *Acta Materialia* 103 (Jan. 2016), pp. 322–333. ISSN: 1359-6454. DOI: 10.1016/J.ACTAMAT.2015.09.060.

[120] Muharrem Mercimek, Kayhan Gulez, and Tarik Veli Mumcu. "Real object recognition using moment invariants". In: *Sadhana 2005 30:6* 30.6 (2005), pp. 765–775. ISSN: 0973-7677. DOI: 10.1007/BF02716709. URL: https://link.springer.com/article/10.1007/BF02716709.

[121] T. Phiasai, S. Arunrungrusmi, and K. Chamnongthai. "Face recognition system with PCA and moment invariant method". In: *ISCAS 2001 - 2001 IEEE International Symposium on Circuits and Systems, Conference Proceedings* 2 (2001), pp. 165–168. DOI: 10.1109/ISCAS.2001.921033.

[122] Anant Bhardwaj, Manpreet Kaur, and Anupam Kumar. "Recognition of plants by Leaf Image using Moment Invariant and Texture Analysis". In: *International Journal of Innovation and Applied Studies* 3.1 (May 2013), pp. 237–248. ISSN: 2028-9324. URL: http://www.ijias.issr-journals.org/abstract.php?article=IJIAS-13-087-01.

[123] Anupam Kumar, Anant Bhardwaj, and Manpreet Kaur. "Recognition of plants by Leaf Image using Moment Invariant and Texture Analysis". In: *International Journal of Innovation and Applied Studies* 3.1 (2013), pp. 237–248. URL: http://www.issr-journals.org/ijias/.

[124] Yudong Zhang et al. "Pathological brain detection in MRI scanning via Hu moment invariants and machine learning". In: *http://dx.doi.org/10.1080/0952813X.2015.1132274* 29.2 (Mar. 2016), pp. 299–312. ISSN: 13623079. DOI: 10.1080/0952813X.2015.1132274. URL: https://www.tandfonline.com/doi/abs/10.1080/0952813X.2015.1132274.

[125] Yu Dong Zhang et al. "Alcoholism detection by medical robots based on Hu moment invariants and predator–prey adaptive-inertia chaotic particle swarm optimization". In: *Computers & Electrical Engineering* 63 (Oct. 2017), pp. 126–138. ISSN: 0045-7906. DOI: 10.1016/J.COMPELECENG.2017.04.009.

[126] Zhihu Huang and Jinsong Leng. "Analysis of Hu's moment invariants on image scaling and rotation". In: *ICCET 2010 - 2010 International Conference on Computer Engineering and Technology, Proceedings* 7 (2010). DOI: 10.1109/ICCET.2010.5485542.

[127] Joviša Žunić, Kaoru Hirota, and Paul L. Rosin. "A Hu moment invariant as a shape circularity measure". In: *Pattern Recognition* 43.1 (Jan. 2010), pp. 47–57. ISSN: 0031-3203. DOI: 10.1016/J.PATCOG.2009.06.017.

[128] Dragiša Žunić and Joviša Žunić. "Shape ellipticity based on the first Hu moment invariant". In: *Information Processing Letters* 113.19-21 (Sept. 2013), pp. 807–810. ISSN: 0020-0190. DOI: 10.1016/J.IPL.2013.07.020.

[129] Dragiša Žunić and Joviša Žunić. "Shape ellipticity from Hu moment invariants". In: *Applied Mathematics and Computation* 226 (Jan. 2014), pp. 406–414. ISSN: 0096-3003. DOI: 10.1016/J.AMC.2013.10.062.

[130] Joviša Žunić et al. "On a 3D analogue of the first Hu moment invariant and a family of shape ellipsoidness measures". In: *Machine Vision and Applications* 27.1 (Jan. 2016), pp. 129–144. ISSN: 14321769. DOI: 10.1007/S00138-015-0730-X/TABLES/4. URL: https://link.springer.com/article/10.1007/s00138-015-0730-x.

[131] Dongming Zhao and Jie Chen. "Affine curve moment invariants for shape recognition". In: *Pattern Recognition* 30.6 (June 1997), pp. 895–901. ISSN: 0031-3203. DOI: 10.1016/S0031-3203(96)00126-4.

[132] Paul L. Rosin. "Measuring shape: ellipticity, rectangularity, and triangularity". In: *Machine Vision and Applications 2003 14:3* 14.3 (2003), pp. 172–184. ISSN: 1432-1769. DOI: 10.1007/S00138-002-0118-6. URL: https://link.springer.com/article/10.1007/s00138-002-0118-6.

[133] Patrick Callahan. "THESIS SUBMITTED IN PARTIAL FULFILLMENT OF THE REQUIREMENTS FOR THE DEGREE OF Doctor Of PhilOSOPhV TITLE Quantitative Characterization and Comparison of Precipitate and Grain Shape in Ni-base Superallovs Using Moment Invariants PRESENTED BY ACCEPTED BY THE DEPARTMENT OF". In: ().

[134] Jeremiah P MacSleyne. "Moment invariants for 2-D and 3-D characterization of the morphology of gamme-prime precipitates in nickel-base superalloys". PhD thesis. Carnegie Mellon University, 2008.

[135] J. P. MacSleyne, J. P. Simmons, and M. De Graef. "On the use of 2-D moment invariants for the automated classification of particle shapes". In: *Acta Materialia* 56.3 (Feb. 2008), pp. 427–437. ISSN: 1359-6454. DOI: 10.1016/J.ACTAMAT.2007.09.039.

[136] Marc Degraef. "Shape Descriptors for the Quantification of Microstructures DISTRIBUTION A: Distribution approved for public release". In: (). URL: https://livelink.ebs.afrl.af.mil/livelink/llisapi.dll.

[137] Jin Soo Noh and Kang Hyeon Rhee. "Palmprint identification algorithm using hu invariant moments and otsu binarization". In: *Proceedings - Fourth Annual ACIS International Conference on Computer and Information Science, ICIS 2005* 2005 (2005), pp. 94–99. DOI: 10.1109/ICIS.2005.97.

[138] Pınar Acar. "Recent progress of uncertainty quantification in small-scale materials science". In: *Progress in Materials Science* 117 (Apr. 2021), p. 100723. ISSN: 0079-6425. DOI: 10.1016/J.PMATSCI.2020.100723.

[139] P. S. Koutsourelakis, K. Kuntiyawichai, and G. I. Schuëller. "Effect of material uncertainties on fatigue life calculations of aircraft fuselages: A cohesive element model". In: *Engineering Fracture Mechanics* 73.9 (June 2006), pp. 1202–1219. ISSN: 0013-7944. DOI: 10.1016/J.ENGFRACMECH.2006.01.003.

[140] Shun Peng Zhu et al. "Bayesian framework for probabilistic low cycle fatigue life prediction and uncertainty modeling of aircraft turbine disk alloys". In: *Probabilistic Engineering Mechanics* 34 (Oct. 2013), pp. 114–122. ISSN: 0266-8920. DOI: 10.1016/J.PROBENGMECH.2013.08.004.

[141] Shun Peng Zhu et al. "Probabilistic Physics of Failure-based framework for fatigue life prediction of aircraft gas turbine discs under uncertainty". In: *Reliability Engineering & System Safety* 146 (Feb. 2016), pp. 1–12. ISSN: 0951-8320. DOI: 10.1016/J.RESS.2015.10.002.

[142] Shravan Kotha, Deniz Ozturk, and Somnath Ghosh. "Uncertainty-quantified parametrically homogenized constitutive models (UQ-PHCMs) for dual-phase α/β titanium alloys". In: *npj Computational Materials 2020 6:1* 6.1 (Aug. 2020), pp. 1–20. ISSN: 2057-3960. DOI: 10.1038/s41524-020-00379-3. URL: https://www.nature.com/articles/s41524-020-00379-3.

[143] Shravan Kotha et al. "Uncertainty Quantified Parametrically Homogenized Constitutive Models for Microstructure-Integrated Structural Simulations". In: *Integrating Materials and Manufacturing Innovation* 9.4 (Dec. 2020), pp. 322–338. ISSN: 21939772. DOI: 10.1007/S40192-020-00187-Z/METRICS. URL: https://link.springer.com/article/10.1007/s40192-020-00187-z.

[144] Francesco De Bona et al. “Understanding Uncertainty in Microstructure Evolution and Constitutive Properties in Additive Process Modeling”. In: *Metals 2022, Vol. 12, Page 324* 12.2 (Feb. 2022), p. 324. ISSN: 2075-4701. DOI: 10.3390/MET12020324. URL: https://www.mdpi.com/2075-4701/12/2/324/htm%20https://www.mdpi.com/2075-4701/12/2/324.

[145] Bruno Sudret, Stefano Marelli, and Joe Wiart. “Surrogate models for uncertainty quantification: An overview”. In: *2017 11th European Conference on Antennas and Propagation, EUCAP 2017* (May 2017), pp. 793–797. DOI: 10.23919/EUCAP.2017.7928679.

[146] Chong Wang et al. “Recent Advances in Surrogate Modeling Methods for Uncertainty Quantification and Propagation”. In: *Symmetry 2022, Vol. 14, Page 1219* 14.6 (June 2022), p. 1219. ISSN: 2073-8994. DOI: 10.3390/SYM14061219. URL: https://www.mdpi.com/2073-8994/14/6/1219/htm%20https://www.mdpi.com/2073-8994/14/6/1219.

[147] Badri Hiriyur, Haim Waisman, and George Deodatis. “Uncertainty quantification in homogenization of heterogeneous microstructures modeled by XFEM”. In: *International Journal for Numerical Methods in Engineering* 88.3 (Oct. 2011), pp. 257–278. ISSN: 1097-0207. DOI: 10.1002/NME.3174. URL: https://onlinelibrary.wiley.com/doi/10.1002/nme.3174.

[148] Pejman Honarmandi and Raymundo Arróyave. “Uncertainty Quantification and Propagation in Computational Materials Science and Simulation-Assisted Materials Design”. In: *Integrating Materials and Manufacturing Innovation 2020 9:1* 9.1 (Jan. 2020), pp. 103–143. ISSN: 2193-9772. DOI: 10.1007/S40192-020-00168-2. URL: https://link.springer.com/article/10.1007/s40192-020-00168-2.

[149] Rohit K. Tripathy and Ilias Bilionis. "Deep UQ: Learning deep neural network surrogate models for high dimensional uncertainty quantification". In: *Journal of Computational Physics* 375 (Dec. 2018), pp. 565–588. ISSN: 0021-9991. DOI: 10.1016/J.JCP.2018.08.036.

[150] Mohammadreza Yaghoobi et al. "PRISMS-Plasticity: An open-source crystal plasticity finite element software". In: *Computational Materials Science* 169 (Nov. 2019), p. 109078. ISSN: 0927-0256. DOI: 10.1016/J.COMMATSCI.2019.109078.

[151] Mohammadreza Yaghoobi et al. "PRISMS-Fatigue computational framework for fatigue analysis in polycrystalline metals and alloys". In: *npj Computational Materials 2021 7:1* 7.1 (Mar. 2021), pp. 1–12. ISSN: 2057-3960. DOI: 10.1038/s41524-021-00506-8. URL: https://www.nature.com/articles/s41524-021-00506-8.

[152] Arulmurugan Senthilnathan and Pınar Acar. "Shape moment invariants as a new methodology for uncertainty quantification in microstructures". In: *AIAA Scitech 2021 Forum* (2021), pp. 1–13. DOI: 10.2514/6.2021-1697. URL: https://arc.aiaa.org/doi/10.2514/6.2021-1697.

[153] Bradley H. Jared et al. "Additive manufacturing: Toward holistic design". In: *Scripta Materialia* 135 (July 2017), pp. 141–147. ISSN: 1359-6462. DOI: 10.1016/J.SCRIPTAMAT.2017.02.029.

[154] Felipe A.C. Viana et al. "Metamodeling in multidisciplinary design optimization: How far have we really come?" In: *AIAA Journal* 52.4 (Mar. 2014), pp. 670–690. ISSN: 00011452. DOI: 10.2514/1.J052375/ASSET/IMAGES/LARGE/FIGURE5.JPEG. URL: https://arc.aiaa.org/doi/10.2514/1.J052375.

[155] Daniel Lizotte et al. "Automatic Gait Optimization with Gaussian Process Regression". In: ().

[156] Carl Edward Rasmussen. "Gaussian Processes in machine learning". In: *Lecture Notes in Computer Science (including subseries Lecture Notes in Artificial Intelligence and Lecture Notes in Bioinformatics)* 3176 (2004), pp. 63–71. ISSN: 16113349. DOI: 10.1007/978-3-540-28650-9{_}4/COVER. URL: https://link.springer.com/chapter/10.1007/978-3-540-28650-9_4.

[157] Ilias Bilionis and Nicholas Zabaras. "Multi-output local Gaussian process regression: Applications to uncertainty quantification". In: *Journal of Computational Physics* 231.17 (July 2012), pp. 5718–5746. ISSN: 0021-9991. DOI: 10.1016/J.JCP.2012.04.047.

[158] Noel Cressie. "The origins of kriging". In: *Mathematical Geology 1990 22:3* 22.3 (Apr. 1990), pp. 239–252. ISSN: 1573-8868. DOI: 10.1007/BF00889887. URL: https://link.springer.com/article/10.1007/BF00889887.

[159] Zhuo Wang et al. "Uncertainty Quantification in Metallic Additive Manufacturing Through Physics-Informed Data-Driven Modeling". In: *JOM* 71.8 (Aug. 2019), pp. 2625–2634. ISSN: 15431851. DOI: 10.1007/S11837-019-03555-Z/FIGURES/7. URL: https://link.springer.com/article/10.1007/s11837-019-03555-z.

[160] Liang Xia, Balaji Raghavan, and Piotr Breitkopf. "Towards surrogate modeling of material microstructures through the processing variables". In: *Applied Mathematics and Computation* 294 (Feb. 2017), pp. 157–168. ISSN: 0096-3003. DOI: 10.1016/J.AMC.2016.08.056.

[161] Maciej Serda et al. "DACE - A Matlab Kriging Toolbox". In: *Uniwersytet śląski* 7.1 (2002). Ed. by G. Balint et al., pp. 343–354. ISSN: 1868-7075. DOI: 10.2/JQUERY.MIN.JS. URL: https://orbit.dtu.dk/en/publications/dace-a-matlab-kriging-toolbox.

[162] Jerome Sacks et al. “Design and Analysis of Computer Experiments”. In: 4.4 (Nov. 1989), pp. 409–423. ISSN: 0883-4237. DOI: 10.1214/SS/1177012413. URL: https://projecteuclid.org/journals/statistical-science/volume-4/issue-4/Design-and-Analysis-of-Computer-Experiments/10.1214/ss/1177012413.short.

[163] W. Heisenberg. “Zur Theorie des Ferromagnetismus”. In: *Zeitschrift für Physik* 49.9-10 (Sept. 1928), pp. 619–636. ISSN: 14346001. DOI: 10.1007/BF01328601/METRICS. URL: https://link.springer.com/article/10.1007/BF01328601.

[164] F. Y. Wu. “The Potts model”. In: *Reviews of Modern Physics* 54.1 (Jan. 1982), p. 235. ISSN: 00346861. DOI: 10.1103/RevModPhys.54.235. URL: https://journals.aps.org/rmp/abstract/10.1103/RevModPhys.54.235.

[165] R. J. Baxter and F. Y. Wu. “Exact Solution of an Ising Model with Three-Spin Interactions on a Triangular Lattice”. In: *Physical Review Letters* 31.21 (Nov. 1973), p. 1294. ISSN: 00319007. DOI: 10.1103/PhysRevLett.31.1294. URL: https://journals.aps.org/prl/abstract/10.1103/PhysRevLett.31.1294.

[166] “The Heisenberg model 1.1 Definition of the model”. In: (). URL: https://folk.ntnu.no/johnof/magnetism-2012.pdf%20Accessed:%202023-04-03.

[167] “The Ising model”. In: (). URL: https://www.math.arizona.edu/~tgk/541/chap1.pdf.

[168] George T. Rado. “Magnetoelectric studies of critical behavior in the Ising-like antiferromagnet DyPO4”. In: *Solid State Communications* 8.17 (Sept. 1970), pp. 1349–1352. ISSN: 0038-1098. DOI: 10.1016/0038-1098(70)90040-2.

[169] J. C. Wright et al. “DyPO4: A Three-Dimensional Ising Antiferromagnet”. In: *Physical Review B* 3.3 (Feb. 1971), p. 843. ISSN: 01631829. DOI: 10.1103/PhysRevB.3.843. URL: https://journals.aps.org/prb/abstract/10.1103/PhysRevB.3.843.

[170] Q. Jiang, X. F. Cui, and M. Zhao. “Size effects on Curie temperature of ferroelectric particles”. In: *Applied Physics A: Materials Science and Processing* 78.5 (Dec. 2004), pp. 703–704. ISSN: 09478396. DOI: 10.1007/S00339-002-1959-6/METRICS. URL: https://link.springer.com/article/10.1007/s00339-002-1959-6.

[171] M. Hasan, A. Senthilnathan, and P. Acar. “Uncertainty-Dominated Phase Transitions of Two-Dimensional Magnetic Materials”. In: *AIAA Journal* 60.5 (2022). ISSN: 1533385X. DOI: 10.2514/1.J061465.

[172] Jonathan V. Selinger. “Introduction to the Theory of Soft Matter”. In: Soft and Biological Matter (2016). DOI: 10.1007/978-3-319-21054-4. URL: http://link.springer.com/10.1007/978-3-319-21054-4.

[173] T Kennedy. *Math 541: Introduction to Mathematical Physics Lecture Notes*. 2008.

[174] Richard P. Feynman et al. “The Feynman Lectures on Physics; Vol. I”. In: *American Journal of Physics* 33.9 (July 2005), p. 750. ISSN: 0002-9505. DOI: 10.1119/1.1972241. URL: https://aapt.scitation.org/doi/abs/10.1119/1.1972241.

[175] Pinar Senthilnathan Arulmurugan; Acar and Bart Raeymaekers. “Reconstructing synthetic surface topography maps from an experimental measurement using a Markov random field graphical network”. Blacksburg, 2023.

[176] Surapol Raadnui. “Wear particle analysis—utilization of quantitative computer image analysis: A review”. In: *Tribology International* 38.10 (Oct. 2005), pp. 871–878. ISSN: 0301-679X. DOI: 10.1016/J.TRIBOINT.2005.03.013.

[177] Xing Liu et al. “A machine learning approach to fracture mechanics problems”. In: *Acta Materialia* 190 (May 2020), pp. 105–112. ISSN: 1359-6454. DOI: 10.1016/J.ACTAMAT.2020.03.016.

[178] L. Anand and M. Kothari. “A computational procedure for rate-independent crystal plasticity”. In: *Journal of the Mechanics and Physics of Solids* 44.4 (Apr. 1996), pp. 525–558. ISSN: 0022-5096. DOI: 10.1016/0022-5096(96)00001-4.

[179] Pınar Acar, Ali Ramazani, and Veera Sundararaghavan. “Crystal Plasticity Modeling and Experimental Validation with an Orientation Distribution Function for Ti-7Al Alloy”. In: *Metals 2017, Vol. 7, Page 459* 7.11 (Oct. 2017), p. 459. ISSN: 2075-4701. DOI: 10.3390/MET7110459. URL: https://www.mdpi.com/2075-4701/7/11/459/htm%20https://www.mdpi.com/2075-4701/7/11/459.

[180] Pinar Acar. “Machine Learning Reinforced Crystal Plasticity Modeling Under Experimental Uncertainty”. In: *https://doi.org/10.2514/1.J059233* 58.8 (July 2020), pp. 3569–3576. ISSN: 00011452. DOI: 10.2514/1.J059233. URL: https://arc.aiaa.org/doi/10.2514/1.J059233.

Appendices

Appendix A

Crystal Plasticity Simulations

The open-source Crystal Plasticity Finite Element (CPFE) software, PRISMS-Plasticity [150, 151], developed by the University of Michigan, is utilized for carrying out CPFE simulations to determine mechanical properties. The PRISMS-Plasticity is a 3D CPFE software that involves the rate-independent crystal plasticity model coupled with a twin activation mechanism. Therefore, it can model both slip and twin system behaviors for Ti-7Al. Because of the ability to model the twin deformation, the PRISMS-Plasticity model is expected to achieve a high-fidelity representation of the local deformation behavior. The constitutive model of each grain in the PRISMS-CPFE software is modeled through a rate-independent single crystal plasticity theory developed by [178] where the hardening moduli (h^{β} for the slip system β) is expressed as:

$$h^{\alpha\beta} = h_o^{\beta} q \left[1 - \frac{s^{\beta}}{s_s^{\beta}}\right]^{a^{\beta}} \tag{A.1}$$

where h_o and s_s represent the hardening parameter and slip resistance at the hardening saturation, respectively, a is a material constant, and q represents the latent hardening ratio [150].

The Ti-7Al alloy has an HCP crystallographic structure with the basal $< a >$, prismatic $< a >$, pyramidal $< a >$, and pyramidal $< c + a >$ slip systems in addition to the six twinning systems. However, the twinning activity during the tension test is found to be

Table A.1: Elastic parameters of Ti-7Al in GPa [179]

C_{11}	C_{12}	C_{13}	C_{33}	C_{44}
175	88.7	62.3	220	62.2

negligible for Ti-7Al alloy [179]. The independent elastic parameters of Ti-7Al used for the simulations are listed in Table A.1 [179]. The dependent elastic parameters are formulated as follows: $C_{22} = C_{11}$, $C_{23} = C_{13}$, $C_{55} = C_{44}$, and $C_{66} = (C_{11} - C_{12})/2$. The microstructure image of $N \times N$ resolution is modeled as voxels of the same dimensions resulting in N^2 voxels. A 10×10 coarse meshing strategy is used on the model to achieve computational efficiency. Each pixel of the actual image is represented by a single voxel in the CPFE model. The slip system parameters used in the crystal plasticity simulation are obtained from a previous study [180]. The initial texture is assumed to represent variations around a randomly-oriented microstructure. Uniaxial tension simulations are performed for the microstructural images and mechanical properties are determined from the resulting stress-strain curves [57, 59, 58].